ATOMICALLY RESOLVED TRANSMISSION ELECTRON MICROSCOPY AND IN-SITU VOLTAGE-DRIVEN DYNAMIC RESPONSE OF DOMAIN WALLS IN LEAD-FREE FERROELECTRICS

Oana-Andreea Condurache

Doctoral Dissertation
Jožef Stefan International Postgraduate School
Ljubljana, Slovenia

Supervisor: Prof. Dr. Andreja Benčan Golob, Jožef Stefan Institute and Jožef Stefan International Postgraduate School, Ljubljana, Slovenia
Co-Supervisor: Prof. Dr. Goran Dražić, National Institute of Chemistry and Jožef Stefan International Postgraduate School, Ljubljana, Slovenia

Evaluation Board:
Prof. Dr. Sašo Šturm, Chair, Jožef Stefan Institute and Jožef Stefan International Postgraduate School, Ljubljana, Slovenia
Dr. Francisco Ruiz Zepeda, Member, National Institute of Chemistry, Ljubljana, Slovenia
Prof. Dr. Vasiliki Tileli, Member, École Polytechnique Fédérale de Lausanne, Lausanne, Switzerland

MEDNARODNA PODIPLOMSKA ŠOLA JOŽEFA STEFANA
JOŽEF STEFAN INTERNATIONAL POSTGRADUATE SCHOOL

Oana-Andreea Condurache

ATOMICALLY RESOLVED TRANSMISSION ELECTRON MICROSCOPY AND IN-SITU VOLTAGE-DRIVEN DYNAMIC RESPONSE OF DOMAIN WALLS IN LEAD-FREE FERROELECTRICS

Doctoral Dissertation

PRESEVNA ELEKTRONSKA MIKROSKOPIJA DOMENSKIH STEN NA ATOMSKI RAVNI IN NJIHOV IN SITU DINAMIČNI ODZIV NA ELEKTRIČNO POLJE V FEROELEKTRIKIH BREZ SVINCA

Doktorska disertacija

Supervisor: Prof. Dr. Andreja Benčan Golob
Co-Supervisor: Prof. Dr. Goran Dražić

Ljubljana, Slovenia, June 2023

Acknowledgments

I am deeply grateful to everyone who has shaped and contributed to the realization of this dissertation.

First and foremost, I express my deepest gratitude to my supervisors Prof. Andreja Benčan and Prof. Goran Dražić for their continuous guidance, kindness and shared knowledge. Thank you for your openness which empowered me to be braver in various aspects of my studies.

I would like to thank Prof. Tadej Rojac for insightful discussions, assistance with data interpretation and for his consistently inspiring creativity.

Many thanks to Brigita for her endless patience and for saving me when I felt lost in the laboratory.

To all my international friends that I have met during my PhD studies. They have taught me so many valuable lessons, made me discover Slovenian mountains and made me wonder, at times, why borders exist. I extend my thanks to all the K5 colleagues for guidance, support, and friendship. Special thanks to Matej and Samir for always being there to answer my questions. I am grateful to Mirela for being a fellow Romanian and reminding me of my roots throughout my PhD journey. A heartfelt thanks goes to my office-mate Victor for all the laughter and thought-provoking discussions about the world. To Francesco who has been my best friend all these years and has always been by my side.

Abstract

Ferroelectric domain walls (DWs) are nano-to-atomic-scale interfaces that separate domains of different polar order. What makes DWs so interesting is their dynamic nature in an electric field, which offers an exciting potential for nanoscale and atomic-scale applications, but, also, more generally, the dynamics of DWs is linked to a fundamental understanding of ferroelectricity. The aim of this PhD thesis was to study DWs in lead-free ferroelectric bulk systems under static and dynamic conditions on the local scale by (scanning)-transmission electron microscopy-(S)TEM.

In the first part of the thesis a comparative study between step-like uncharged and charged DWs in polycrystalline $BiFeO_3$ is performed in terms of strain and structure. Our results show that uncharged DWs exhibit a higher and more concentrated strain than their charged counterparts. The lower strain of charged DWs is associated with a wider transition (i.e. change in directions and magnitude) of polarization vector across the DWs. All the step-like DWs reported here, regardless of their charge state, exhibit a comparable number of Bi vacancies and present a non-Ising behavior.

The second part presents a dynamic study of the atomic-level response of zigzag DWs in $BiFeO_3$ single crystals in a subcoercive field regime. The atomic-level movement of a single DW was observed. One of the foremost results is that, on the atomic scale, the movement of the wall under an electric field is decoupled from the strain field marking the initial position of the wall. We could explain this by the segregation of defects with a relatively low mobility, such as clusters of oxygen vacancies. Furthermore, the triangular tip of the zigzag DW is pinned, but a short-range change in its properties occurs: asymmetry is induced in the wall plane leading to strain, bound charge and a possible redistribution of the Bi-vacancies.

The last part of the thesis presents the results for the kinetics of domains in $(K,Na)NbO_3$ single crystals. The dynamics of the mobile, needle-like DWs is influenced by other immobile walls, which act as random bound defects. Domain growth and coalescence may cease at a certain voltage with a subsequent increase in the number of DWs due to splitting of the needles and the formation of nanodomains. Pinning events and domain-domain interactions between two orthogonal, needlelike domains are directly probed. Our results suggest that this interaction is mediated by strain.

Povzetek

V feroelektričnih materialih so domene, področja z enotno polarizacijo, ločene z domenskimi stenami (DS). Stene so različnih velikosti, nastajajo na nanometrski ali atomski ravni in se pod električnim poljem premikajo. Lokalne lastnosti DS na nanometrskem in atomskem nivoju se lahko neposredno izkorišča v različnih aplikacijah, prav tako dinamika DS pomembno vpliva tudi na celokupni makroskopski odziv feroelektrikov.

Namen doktorske disertacije je z uporabo metod (vrstične) presevne elektronske mikroskopije preučiti lokalne statične in dinamične lastnosti domenskih sten v feroelektričnih volumenskih materialih, ki ne vsebujejo svinca.

V prvem delu disertacije smo izvedli strukturno primerjalno študijo stopničastih nenabitih in nabitih DS v polikristaliničnem $BiFeO_3$ na atomskem nivoju. Pokazali smo, da nenabite stene izkazujejo večje lokalne napetosti kot nabite stene. Manjše lokalne napetosti nabitih DS so povezane s postopno spremembo smeri in velikosti polarizacije čez steno. Vse preučevane stopničaste stene so izkazovale rotacijo polarizacije na steni – »ne-Ising« obnašanje – in vsebovale primerljivo količino vrzeli na mestih bizmuta.

V drugem delu doktorske disertacije smo na atomskem nivoju študirali dinamiko »cik-cak« domenskih sten v monokristalu $BiFeO_3$ v režimu subkoercitivnega električnega polja. Eden od najpomembnejših rezultatov je, da se na atomski ravni stena pod električnim poljem loči od napetostnega polja, ki označuje začetni položaj stene. Napetostno polje smo pojasnili s segregacijo defektov z relativno nizko gibljivostjo, kot so na primer skupki vrzeli na mestih kisika. Vrh cik-cak domen ostaja pod električnim poljem pričvrščen, pojavijo se lokalne spremembe, inducira se asimetrija v napetosti stene, v naboju stene in pride do prerazporeditve vrzeli na mestih bizmuta.

Zadnji del disertacije predstavlja študijo o mobilnosti domen v monokristalu $(K,Na)NbO_3$. Na dinamiko mobilnih igličastih DS vplivajo druge, negibljive stene. Ko pri določeni napetosti pride do povečanja števila DS zaradi cepitve igličastih domen in nastanka manjših nanodomen, se rast in združevanje domen prekine. V študiji smo neposredno opazovali dogodke pripenjanja in interakcije, preko lokalnih napetosti, dveh igličastih, pravokotnih domen.

Contents

List of Figures

List of Tables

Abbreviations

ABF	...	(Annular) Bright Field
ABO_3	...	chemical formula of the perovskite unit cell
BF	...	Bright Field
BFO		$BiFeO_3$
BFP	...	Back Focal Plane
CDW	...	Charged Domain Walls
CTEM	...	Conventional Transmission Electron Microscopy
DF	...	Dark Field
DW	...	Domain Wall
EDXS	...	Energy-Dispersive X-ray Spectroscopy
EELS	...	Electron Energy Loss Spectroscopy
FIB	...	Focused Ion Beam
HAADF	...	High Angle Annular Dark Field
HH	...	head-to-head
HRTEM	...	High Resolution Transmission Electron Microscopy
HT	...	head-to-tail
KAI	...	Kolmogorov-Avrami-Ishibashi model
LAADF	...	Low Angle Annular Dark Field
MEMS	...	Microelectromechanical Systems
OL	...	Objective Lens
pc	...	pseudo-cubic
SAED	...	Selected Area Electron Diffraction
STEM	...	Scanning Transmission Electron Microscopy
TEM	...	Transmission Electron Microscopy
TT	...	tail-to-tail
UDW	...	Uncharged Domain Walls

Symbols

$F_{gradient\ energy}$	... the gradient energy of a domain wall
$F_{ordering\ energy}$	... the ordering energy of a domain wall
P_S	... spontaneous polarization
P_{max}	... saturation polarization
P_{rem}	... remanent polarization
T_C	... Curie temperature
d_{hkl}	... lattice constant for *hkl* planes
g_{hkl}	... Bragg reflection
λ_{path}	... mean free path
ρ_{DW}	... the bound charge at DW location
E_C	... coercive field
E_d	... depolarizing field
$F_{domains}$	... the energy of domains
F_{DWs}	... the energy of domain walls
hkl	... Miller Indices
I	... total transmitted integral intensity
I_0	... zero-loss peak integral intensity
t	... specimen thickness
w	... domain size
Z	... Atomic number
E	... electric field
F	... free energy
$\boldsymbol{P}$	... polarization
$\boldsymbol{T}$	... temperature
U	... volume energy of the domains
d	... crystallite size (grain size or the thickness of a thin film)
k	... gradient coefficient (called also exchange constant)
$\boldsymbol{n}$	... the unit normal vector
$\boldsymbol{\nabla}$	... divergence
δ	... domain wall thickness
λ	... wavelength of a radiation
ρ	... volume charge density
σ	... energy volume density of the DWs
χ	... electric susceptibility

Chapter 1

Introduction

In the introduction, a theoretical background is given on the topics relevant to the thesis. The chapter begins with a motivation of the present work. The following section introduces the fundamentals of ferroelectric materials. The chapter continues with details on (scanning) transmission electron microscopy-(S)TEM image formation and modes and a brief review on in situ TEM techniques. The chapter concludes with a list of objectives and hypothesis which are at the basis of the present thesis.

1.1 Motivation

Ferroelectric/piezoelectric materials are important components in many devices, such as sensors, transducers, actuators and energy-harvesting devices. Nowadays, lead-based ferroelectric/piezoelectric materials dominate the market. However, due to legislation and restrictions on lead in commercial products [1], great efforts have been made to develop more environmentally friendly alternatives. There are two main groups of lead-free ferroelectrics currently under development: those that compete directly with lead-based materials in terms of piezoelectric activity (e.g., $(K_{0.5}Na_{0.5})NbO_3$)[2] and those that have poorer properties but a high Curie temperature and are potential candidates for high-temperature applications (e.g., $BiFeO_3$)[3].

Ferroelectric domain walls (DWs) are nano-to-atomic-level interfaces that separate domains with different polarization vector orientations. DWs-based nanoelectronics aims to exploit the mobility of DWs and incorporate them into electronic devices designed for miniaturization, lower power consumption, and fast access times [4]. In addition, the interaction of DWs and domains with the external electric field makes an important extrinsic contribution to the macroscopic functional properties of the ferroelectric [5].

Therefore, a thorough understanding of the properties of DWs (morphology, structure, strain distribution, possible defects segregation) and the interplay between the properties and the functional response (i.e., the electrical response) is of paramount importance, not only for the development of future atomic-scale electronics, but also for a fundamental understanding of ferroelectricity.

Since DWs are atomic-scale features, their complexity has only been revealed in the last decade, largely thanks to the development of atomic-resolution (S)TEM techniques in combination with analytical tools. DWs are no longer seen as simple straight interfaces, but have been shown to have particular morphologies (e.g., step-like [6]), complex structure (e.g., unusual strain modulation [7]) or a different chemistry from the domain matrix (e.g., DWs that present the segregation of defects [8]).

The properties of the walls directly determine their elastic and electrostatic energy; therefore, they are expected to have a direct influence on their dynamics. A further step in characterizing DWs is to observe their response to an external electric field in situ. Since it is a local characterization technique (from a few µm to the atomic scale), the in-situ voltage bias (S)TEM sometimes challenges the understanding of ferroelectricity from a macroscopic point of view. For instance, it has been shown that the ferroelectric switching is an inhomogeneous process at the local scale, since a statistical approach cannot be applied, and a single lattice defect can have a huge impact on the switching dynamics [9].

Curiously, the number of in-situ voltage-bias studies with atomic resolution, investigating the interaction between DWs and electric field, is small. Gao et al. [10] discovered an atomic-scale mechanism of dipole glass formation at the interface between a ferroelastic domain and a switched domain that impedes the switching process. This illustrates how complex atomic-level phenomena can be, and what a tremendous impact they have on the overall response of the system, which is particularly important in miniature devices where the kinetics of individual domains dominate the functionality. However, the paucity of high-resolution studies on DWs could be due to tedious specimen preparation; the specimen should be thin enough to achieve atomic resolution using the (S)TEM technique (ideally below 100 nm) while maintaining the integrity of the electrical device.

The focus of this thesis is on the local characterization of DWs in lead-free ferroelectrics under static and dynamic conditions by means of (S)TEM and in-situ (S)TEM.

1.2 Ferroelectrics

Ferroic materials are characterized by a long-range order parameter, which can have two or more polarities and can be switched between them by applying an external (electric, mechanic, or magnetic) field. In terms of their order parameter, the primary ferroics are ferroelectric, ferroelastic and ferromagnetic materials. If a material exhibits more than one primary ferroic property, it is called multiferroic.

The switching property of the order parameter is possible at temperatures lower than a critical temperature ($T \leq Tc$) called the Curie temperature. At this temperature, a phase transition takes place and a break in the symmetry occurs.

Ferroelectric materials are characterized by spontaneous polarization ($\boldsymbol{P_s}$) as an order parameter (i.e., a permanent electrical dipole at the unit-cell level). $\boldsymbol{P_s}$ can be switched between two equilibrium states by applying an electrical field [11].

Ferroelectrics belong to the class of piezoelectric materials and are also ferroelastics. The order parameter in feroelastics is spontaneous strain and it can be switched by applying a mechanical stress. The spontaneous strain in ferroelectrics is coupled to the spontaneous polarization via electrostrictive coefficients.

A permanent dipole moment at the unit-cell level implies a separation of the mass center of the positive and negative charges. The majority of ferroelectrics with relevant technological applications are perovskites with the chemical formula: ABO_3 [11] [12]. A common way of representing the perovskite unit cell is as a corner-centered A cations cell containing BO_6 octahedra (Figure 1.1 a)).

The spontaneous polarization in ferroelectric perovskites, such as, $K_{0.5}Na_{0.5}NbO_3$, $BiFeO_3$, $BaTiO_3$ and $PbTiO_3$, can be described by shifts of the B-site cations and O ions relative to the A-site cations. In Figure 1.1 b) a simplified distortion is represented only by the B-site displacement with respect to the A lattice. However, the polarization can have other directions fixed by the crystal symmetry (in Table 2.1 the polarization direction in

the main perovskite symmetries is listed). The total dipole moment of the unit cell will depend on the atomic displacements, as well as on the oxygen-octahedral tilts [13] [14].

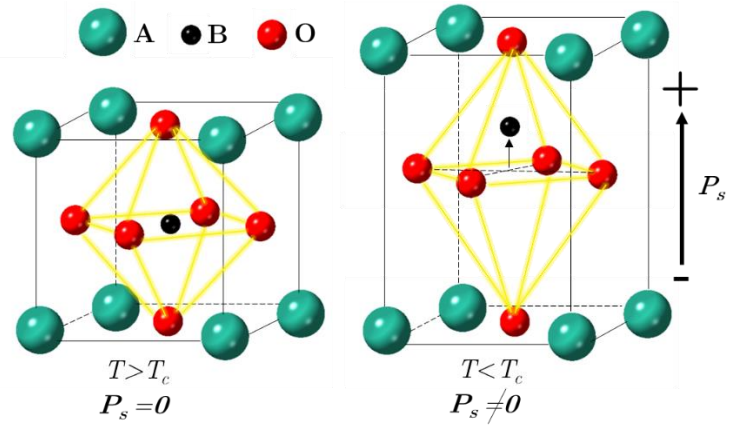

Figure 1.1: Perovskite Structure¶ at a) $T > T_C$ for which the structure is cubic (centrosymmetric) and no spontaneous polarization occurs and at b) $T < T_C$ for which the structure is non-centrosymmetric and a spontaneous polarization (Ps) appears as a consequence of the separation of the center of positive and negative charges. In this simplified case only the B-site displacement with respect to the A lattice is shown.

1.2.2 Domain structure and domain walls

An important characteristic of a ferroelectric material is the organization in regions with different orientations of the polarization vector, regions called ferroelectric domains. The region of transition between one domain and another is called the domain wall (DW). Since the polarization orientation differs from one domain to another, the domains must differ in the orientation of the crystallographic axes. [11] [15]

1.2.2.1 Formation of domains

All real crystals are finite and present surfaces. In a polarized dielectric, bound charges arise on the surface of the material in accord with equation 1.1, where ρ is the volume charge density and $\boldsymbol{P}$ is the polarization:

$$\rho = -\nabla \bullet \boldsymbol{P} \tag{1.1}$$

The surface-bound charges will lead to the appearance of an electrical field opposite to the spontaneous polarization, called the depolarizing field ($\boldsymbol{E_d}$). The formation of periodic ferroelectric domains helps to minimize the free energy of the entire crystalline structure: electrostatic energy created by the depolarizing field (as shown in Figure 1.2) but, in a more general context, also the elastic energy associated with mechanical constraints. Nevertheless, domain formation leads to the creation of DWs that are, in general, energetically costly.

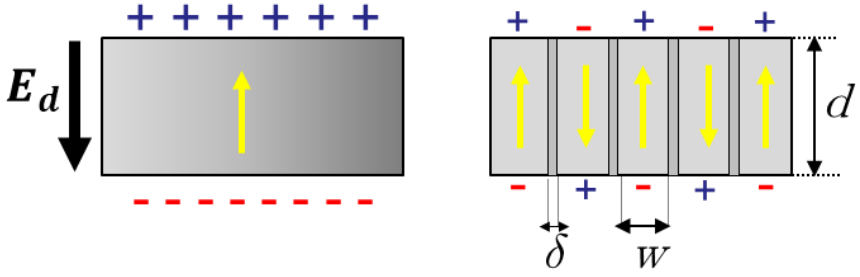

a) b)

Figure 1.2: Cross-section of a ferroelectric. a) A single-domain state in which a depolarizing field arrises ($\boldsymbol{E_d}$) and b) a multi-domain state as a result of free-energy minimization. The bound charges are ilustrated with + and –. The direction of the polarization is marked by a yellow arrow. The crystal size, domain size and DW thicknees are noted as d, w and δ, respectivly.

The size and shape of domains, together with the internal structure of the DWs, will be determined by the minimization of the total free energy (F). The size of the domains has been discussed for ferromagnetic materials by C. Kittle [16] and extrapolated for ferroelectric materials [17]. The domain size (w) is decided by the competition between the two main contributors to the domain free energy: the energy of the domain itself (Fdomains) and the energy associated with the DWs (FDWs) (equation 1.2). While the energy of the domains is proportional to the domain size, the energy of the DWs is inversely proportional to it. In equation 1.2: $\boldsymbol{w}$ is the domain width, $\boldsymbol{\sigma}$ is the energy volume density of the DWs, $\boldsymbol{U}$ is the volume energy of the domains and $\boldsymbol{d}$ is the crystallite size (grain size or the thickness of a thin film). [13] [18]

$$F = F_{domains} + F_{DWs} = Uw + \sigma\frac{d}{w} \tag{1.2}$$

The equilibrium condition (F=minimum $\Rightarrow \frac{dF}{dw} = 0$) leads to Kittel's law, showing that the domain dimension depends on the square root of the crystallite size:

$$w = \sqrt{\tfrac{\sigma}{U}d} \tag{1.3}$$

1.2.2.2 Domain-wall thickness and energy

The energy environment of the DW will affect its thickness and its morphology. There are at least two competitive components that contribute to the DW energy: one from the gradient of the order parameter and one from its ordering. The DW energy is shown in equation 1.4 (as an integration over the DW thickness), where k is the gradient coefficient (also called exchange constant), δ is the DW thickness, $\boldsymbol{P}$ is the polarization and a and b are in the following relation: $P_{max} = \sqrt{\frac{-a}{b}}$, P_{max} being the saturation polarization in a monodomain state [19].

$$F_{DW} = F_{gradient\ energy} + F_{ordering\ energy} = \int_{-\delta/2}^{\delta/2}[\tfrac{k}{2}(\nabla \bullet \boldsymbol{P})^2 + \tfrac{a}{2}P^2 + \tfrac{b}{4}P^4]dx \tag{1.4}$$

On the one hand, in order to reduce the energy caused by the polarization gradient across the wall, the DW thickness should be large (the polarization gradient across the wall will be smaller if the changes in the polarization between adjacent domains are over a larger distance). On the other hand, by increasing the DW thickness, the misalignment between the polarization vectors across the wall increases, and so does the ordering energy of the DWs; hence, minimizing the ordering energy will favor thin DWs.

Ultimately, the equilibrium thickness of the wall is given by the minimum energy condition, given in equation 1.5 (where χ is the susceptibility of the material):

$$\delta = 4\sqrt{k\chi} \tag{1.5}$$

The typical thickness of the ferroelectric DWs is often experimentally determined from one to a few unit cells [20]. In some cases, abnormally thick DWs of tens to a hundred nanometres are reported [21][22]. Wide DWs are assigned to particular strain (e.g., coupling with dislocations) [20] or electrostatic (e.g., accumulation of point-charge defects) [23][24][25] environments.

It is commonly accepted that pure ferroelectric walls (180º walls in which the sign of the polarization is changed across the wall) are atomically sharp, while ferroelectric-ferroelastic DWs (non-180º DWs) are a few unit cells wider [13][22]. However, recent calculations challenge this, showing that for $PbTiO_3$ their thickness may be comparable [26].

The accurate prediction and investigation of the thickness and structure of a DW is not trivial and requires atomic resolution techniques. Thickness and morphology are important components that determine the mobility of the DWs, as discussed in one of the next chapters.

1.2.2.3 Types of domain walls

1.2.2.3.1 Charged and neutral

This classification of DWs is illustrated in Figure 1.3. DWs can have a neutral configuration, side-by-side or head-to-tail (HT) (Figure 1.3 a) and b)) or a charged configuration, tail-to-tail (TT) (Figure 1.3 c) and d)) or head-to-head (HH) (Figure 1.3 e) and f)), in which there are uncompensated bound charges. If a DW is in a HH or TT configuration, the DW is labelled as strongly charged. However, if the plane of the wall slightly deviates from the neutral direction but an overall HT configuration is still maintained, the DW is labelled as weakly charged. Increasing the inclination of the DW in respect to the neutral plane will increase the amount of bound charge. [27] In Figure 1.3 g) and h) a zig-zag (needlelike) domain morphology is shown to serve as an example for weakly charged DWs. Zigzag domain boundaries are a commonly reported morphology [28] [29] and their formation has been demonstrated to be, in some situations, a more stable energetic configuration than the flat-wall morphology [15][30].

Charges are created by any change in the component of the polarization perpendicular to the DW: $\rho_{DW} = \Delta \boldsymbol{P} \bullet \boldsymbol{n}$, where ρ_{DW} is the bound charge at the DW location, $\Delta \boldsymbol{P}$ is the difference between the polarization vectors of adjacent domains and $\boldsymbol{n}$ is the unit normal vector relative to the DW plane.

Because the polarization vector is pointing from the negative charged center towards the positive charged center, the TT configuration will be negatively charged (positive ions

depleted area) and will attract donor ions and holes, while the HH configuration will be positively charged (electron depleted area) and will attract negatively charged defects.

Intrinsically charged DWs may be screened by free charges (electrons, holes, mobile ions). In fact, strongly charged DWs require screening, otherwise, the ferroelectricity will be disrupted by the depolarizing field. [27]

The energy of the charged DWs in perovskites is one order of magnitude higher than their uncharged counterparts [13]. As regards their thickness, calculations [31] and experimental [32] [33] reports suggest charged DWs are thicker than neutral DWs.

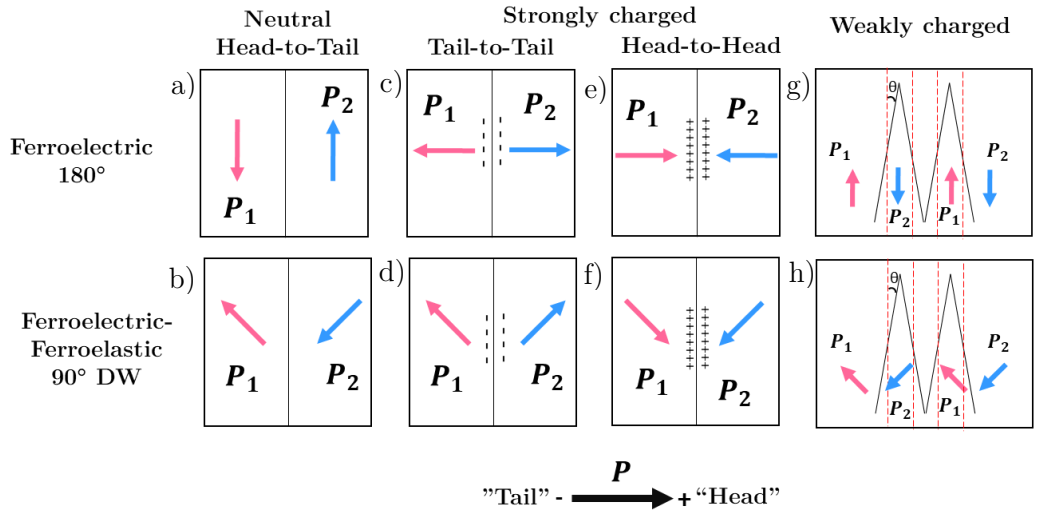

Figure 1.3: Schematics of Neutral/Charged 180° and 90° DWs. a), b) Neutral Head-to-Tail DWs. c), d) Strongly charged Tail-to-Tail DWs. e), f) Strongly-charged Head-to-Head DWs. g), h) Weakly-charged DWs where the actual wall plane (black line) is tilted by an angle θ with respect to the theoretical neutral plane (red dotted line).

1.2.2.3.2 Angle-labelled domain walls

DWs can be labeled according to the angle formed between the polarization vectors on either side of the wall.

As referred to before, a general classification is 180° and non-180° DWs. In general, 180º DWs are solely ferroelectric (the domains present opposite polarization vector), while non-180º DWs are simultaneously ferroelectric and ferroelastic (the domains have different polarization orientation and different strain tensor) [11].

The angle formed between the polarization vectors on either side of the wall depends on the symmetry of the parent material. The polarization directions in the main perovskite phases (tetragonal, rhombohedral and orthorhombic) are shown in Figure 1.4, and Table 1.1 summarizes the types of DWs that can be found in these symmetries and their permissible orientation. The orientation of the DW plane is decided by the elastic compatibility between the two domains and by the charge neutrality [34]. However, the elastic compatibility dominates over the electrical neutrality [19].

For the simpler perovskite distortion, which is the tetragonal, the polar direction is along $[\mathbf{100}]_{pc}$, which leads to six different possible polar orientations and two types of DWs: 90° and 180°. [35] [36] As the symmetry lowers, the number and complexity of the DWs increases. The rhombohedral symmetry has a spontaneous polarization along one of the

four diagonals in the perovskite structure (along $[\mathbf{111}]_{pc}$ direction) and two different orientations for each diagonal; therefore, there are eight different polar domains. This leads to three different types of DWs: 71º, 109º and 180º. [37] In the case of orthorhombic distortion, the spontaneous polarization arises along one of the face diagonals (along $[\mathbf{110}]_{pc}$ directions) and so twelve different polar domains are possible. Four different types of DWs arise: 60º, 120º, 90º and 180º [38] [39].

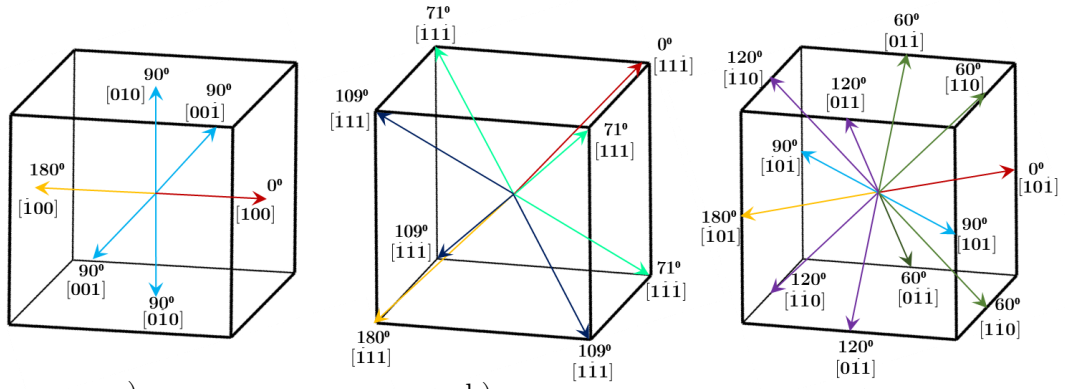

Figure 1.4: Polarization directions in different symmetries. a) Tetragonal, b) Rhombohedral and c) Orthorhombic perovskite phase. The angles between direction "0", chosen arbitrarily as a reference, and the other equivalent directions are shown. The pseudo-cubic crystallographic directions are indicated.

Table 1. Polar direction and types of DWs in the main ferroelectric perovskites. Planes and directions are described using the pseudo-cubic notation.

Symmetry at T_R	Direction of $\boldsymbol{P_s}$	Types of DWs	Planes	Examples of material
Tetragonal	[100] [010] [001] [$\bar{1}$00] [0$\bar{1}$0] [00$\bar{1}$]	180º	planes parallel with $\boldsymbol{P_s}$	$BaTiO_3$ [35]
		90º	{**110**}	
Rhombohedral	[111] [$\bar{1}$11] [1$\bar{1}$1] [11$\bar{1}$] [$\bar{1}\bar{1}$1] [$\bar{1}$1$\bar{1}$] [1$\bar{1}\bar{1}$] [$\bar{1}\bar{1}\bar{1}$]	180º	planes parallel with $\boldsymbol{P_s}$	$BiFeO_3$ [37], $Pb(Zr_{1-x}Ti_x)$, x=0.06-0.45[29]
		109º	{**100**} uncharged {**110**} charged	
		71º	{**110**} uncharged {**100**} charged	
Orthorhombic	[110] [101] [011] [$\bar{1}$01] [$\bar{1}$10] [1$\bar{1}$0] [01$\bar{1}$] [10$\bar{1}$] [0$\bar{1}\bar{1}$] [$\bar{1}$0$\bar{1}$] [$\bar{1}\bar{1}$0] [0$\bar{1}\bar{1}$]	180º	planes parallel with $\boldsymbol{P_s}$	$(K_{0.50}Na_{0.50})NbO_3$ [40]
		120º	{**110**} for uncharged DW (for the charged 120º DW the directions depend on the electrostrictive and piezoelectric coefficients)	
		90º	{**100**}	
		60º	{**110**} for charged DW (for the uncharged 60º DW the directions depend on the electrostrictive and piezoelectric coefficients)	

1.2.2.3.3 Structure of the DW

DWs may sometimes deviate from their straight, flat trajectory and present some degree of roughing. Experimentally, atomic-level steps (from a few unit cells [32] [33] [41] up to 10 unit cells [33]) have been reported to form at the DWs. In the absence of disorder, the system energy is minimized by a flat configuration and so, meandering of the DW trajectory is associated with the presence of pinning sites, such as point defects [15] [42]. Interestingly, roughening of the wall is not always associated with pinning. On the contrary, in some cases steps are linked to increased DW mobility [43].

A different polarization structure in the transition from one domain to another will determine the different types of DWs (Figure 1.5). If the polarization rotates across the wall, the DW is termed chiral. If the rotation is in the wall plane, the DW is called **Néel**

type; if the rotation is out of the wall plane, the DW is called **Bloch type**. The dipole moment is not quantized, so the polarization can, in ferroelectric materials, be potentially reversed by changing its magnitude along the wall: a decrease in magnitude until it is null, change direction and increase in magnitude again. This type of DWs is called the **Ising type**.

Apparently, chirality is not energetically favorable because polarization rotation will introduce large crystalline anisotropy and the accumulation of bound charges. Hence, ferroelectric DWs are expected to be of the Ising type. However, theoretical studies have predicted that DWs could be in ferroelectric perovskites at least partially chiral [44] [45]. As well, experimentally, the presence of Bloch and Néel DWs in ferroelectric perovskites was shown [46] [47] [48]. Nonetheless, little is known about the non-Ising structures of DWs and their origin is not yet clarified. It is believed that the chirality in multiferroics is determined by the competition between the depolarizing and the flexoelectric field [49].

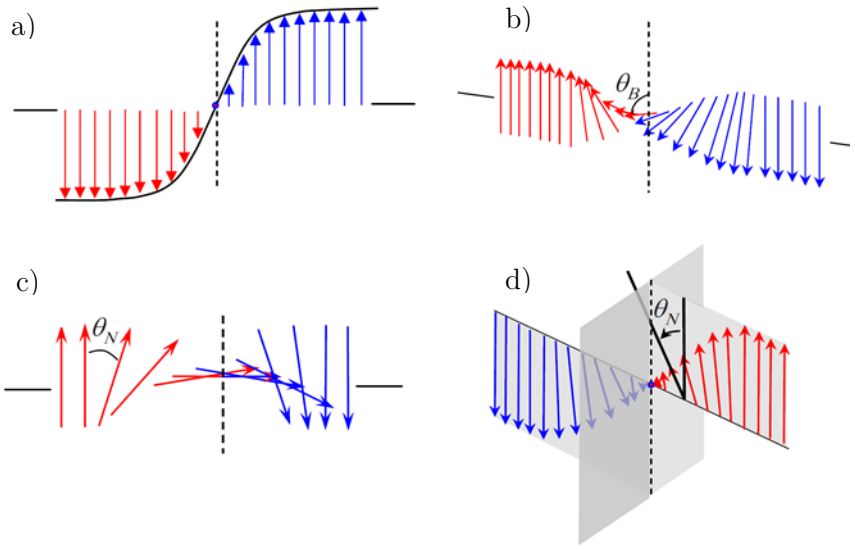

Figure 1.5: Types of DWs. a) Ising type DW, b) Bloch type DW, (c) Néel type DW, (d) Ising-Néel type DW. θ represents the angle between the polarization and the DW plane. Reprinted with permission from [44]. Copyright (2023) by the American Physical Society.

1.2.3 Polarization switching and interaction of a ferroelectric with an electric field

A signature of ferroelectric materials is a hysteretic dependence of polarization on an external electric field (*P-E* loop), illustrated in Figure 1.6. The non-linearity is a consequence of domains and of DWs' movement upon the application of an electric field. In the virgin, non-poled phase, the material has randomly oriented, polar domains and the net polarization is null (Point *a* in Figure 1.6). By applying an electric field ($\boldsymbol{E}$), domains with polarization in the direction of the field grow, while the ones with the opposite polarization direction shrink. For a strong enough $\boldsymbol{E}$, the majority of dipole moments are oriented in the direction of the field and a monodomain state can be achieved (situation *b* in Figure 1.6) corresponding to the saturation polarization $\boldsymbol{P}_{max}$. When decreasing the electric field to 0, some domains will back-switch, but the net polarization is not zero: it has a remanence value $\boldsymbol{P}_{rem}$ (situation *c* in Figure 1.6). Only when a sufficiently high electric field is applied in the opposite direction does the polarization become null again (situation

d in Figure 1.6). This corresponds to a critical field, called the coercive field $\boldsymbol{E_c}$. By increasing the magnitude of the opposite field, a new saturation state can be obtained where the polarization is $\boldsymbol{-P_{max}}$ (situation *e* in Figure 1.6). [50] [51]

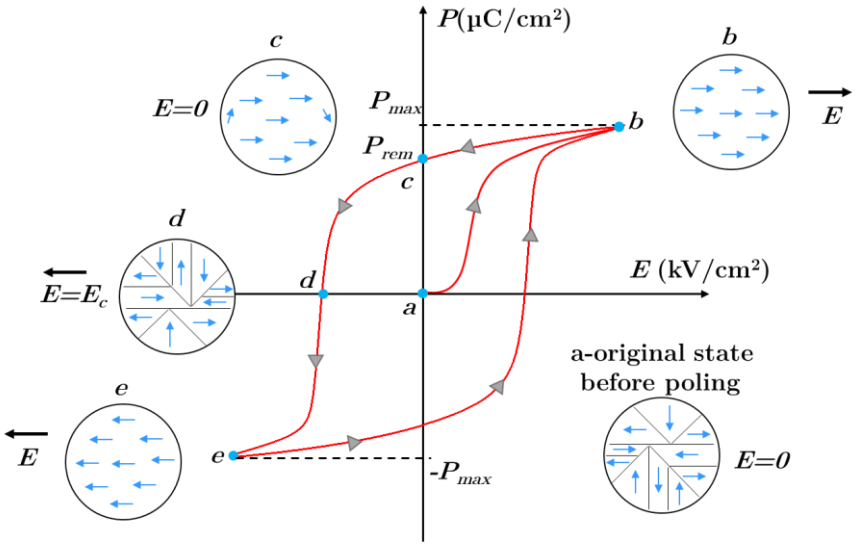

Figure 1.6: Schematic of the hysteresis P-E loop of a ferroelectric. The direction of the electric field is indicated by a black arrow and with blue arrows the polarization direction is marked. Significant points on the loop are marked: *a* – initial non-poled state, *b* – single domain state at saturation ($\boldsymbol{P_{max}}$), *c* – remanence state ($\boldsymbol{P_{rem}}$), *d* – polarization becomes 0 at a critical field applied in opposite direction - coercive field ($\boldsymbol{E_c}$), *e* - single domain state at saturation for the field applied in the opposite direction ($\boldsymbol{-P_{max}}$)

The coercive field ($\boldsymbol{E_c}$) is defined as the minimum electric field above which the polarization can change sign [52]. However, the coercive field is a macroscopically defined quantity, at local scales, each region of the material can have different switching thresholds depending on the local energetic environment. Switching at local scales (e.g., at the scale of the DW) is inherently inhomogeneous [9] [28].

The movement of DWs dominates the polarization switching process. A widely used model to describe the kinetics of polarization switching is the Kolmogorov-Avrami-Ishibashi model (KAI) [53] [54]. This model assumes that the nucleation of new ferroelectric domains is a statistical process, initiated at random locations in the crystal. The nucleation is further followed by unrestricted domain growth. The KAI model describes well a macroscopic system under the influence of high electric fields ($\boldsymbol{E > E_c}$). Nonetheless, KAI does not describe well small systems (e.g., nanocapacitors) or the switching process in a sub-coercive fields regime ($\boldsymbol{E < E_c}$). [55]

In addition, the dynamics of DWs is linked to the interaction with defects and other DWs. DWs attract and are attracted by defects. The defects that interact the most with the DWs are so-called point-charge defects, such as oxygen vacancies, cation vacancies, electrons or holes [56]. The presence of defects at DWs influences their motion, typically by pinning them. The pinning mechanism was defined by Taganstev et al. as “immobilizing of domain walls caused by their interaction with defects” [57]. The pinning will reduce the DW mobility, but the wall can move through these domains if enough energy is provided to overcome the height of the energy barrier, and this process is called de-pinning [13].

1.3 (Scanning) Transmission Electron Microscopy-(S)TEM

TEM is now routine for the characterization of ferroelectric materials. It is one of the most versatile characterization techniques, providing simultaneously, imaging capabilities, information about the crystal structure and chemical composition by electron diffraction and analytical tools, respectively.

A state-of-the-art (S)TEM offers high spatial resolution (down to the atomic level) and the possibility to conduct an analysis while applying external stimuli in situ (e.g., applying an electrical field, change of temperature, application of mechanical stress) or inside gas/liquid environments. Since the functionality of ferroelectrics is decided by their electrical response, in-situ electric biasing (S)TEM offers a unique opportunity to gain insights into fundamental processes such as: switching dynamics, DW movements and their interaction with defects and other interfaces.

1.3.1 Operation of (S)TEM

A TEM operates by accelerating a beam of electrons (typical accelerating voltages are 80–300kV) and transmitting it through an ultra-thin specimen (ideally below 100 nm).

From the interaction between the electron beam and the specimen a batch of signals are generated (Summarized in Figure 1.7). Electrons that pass without interaction are the directly transmitted beam. Nonetheless, most electrons will be scattered (particle nature of electrons is considered) or diffracted (wave nature of electrons is considered), and scattering/diffraction is the key mechanism in image and electron diffraction by TEM. If no measurable energy loss occurs, the scattering is elastic; conversely, if a measurable energy loss occurs, the scattering is inelastic. Another distinction can be made between scattered electrons, referring to their wave nature: coherent (in phase) or incoherent (out-of-phase).

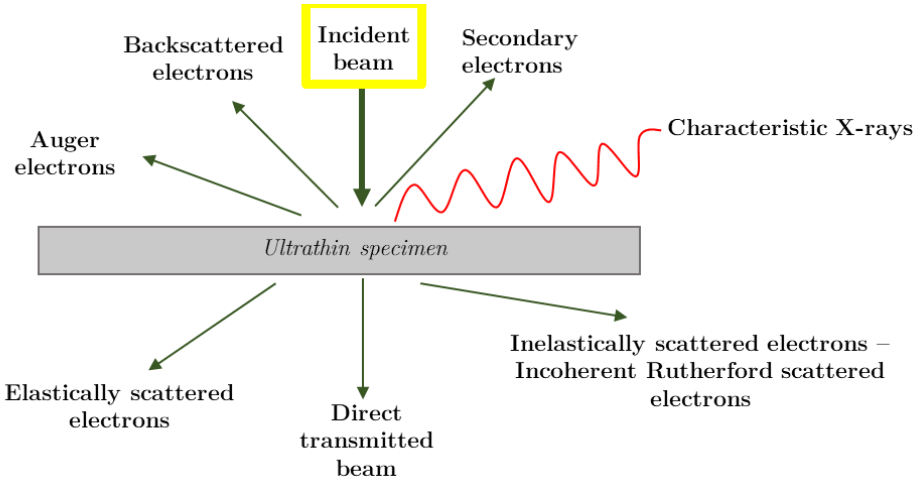

Figure 1.7: Signals generated by the interaction of a high-energy electron beam with an ultra-thin specimen.

Depending on how the illumination system is set up, there are two operating modes: conventional TEM (CTEM) and scanning TEM (STEM) (Figure 1.8). A parallel beam mode is primarily used for imaging in CTEM, while a convergent beam operation mode is used for STEM (but also for X-ray and electrons spectroscopy).

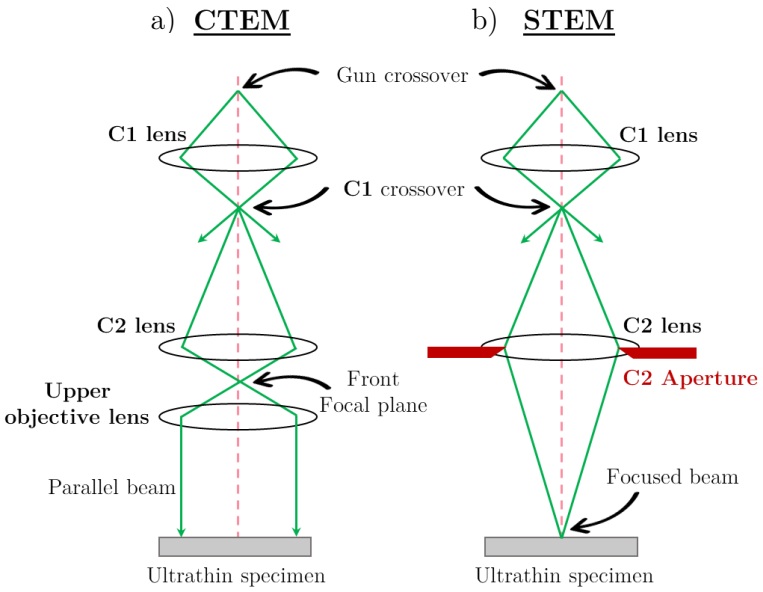

Figure 1.8: Illumination system in TEM.a) Parallel-beam operation in CTEM mode and b) convergent-beam operation in STEM mode. The electromagnetic lenses are represented by black ovals, the electron rays are depicted as green lines, the optical axis is represented by a dotted pink line and the aperture is marked in red. Graphics based on [58].

With CTEM the imaging system can be used either to form a magnified image of the real space (Figure 1.9 a)) or to form a selected-area electron diffraction (SAED) pattern (Figure 1.9 b)). By changing the excitation of the intermediate lens, either the image plane or, the back focal plane (BFP) of the objective lens (OL) is selected as an object for the projection lens. When the object for the projection system is the image plane of the OL, a magnified image of the specimen is displayed on the screen (Figure 1.9 a)). Conversely, when the object is the BFP of the OL, a SAED is formed on the screen (Figure 1.9 b)).

It should be noted that in Figure 1.8 and 1.9, simplified schematics are shown, although, in reality, a modern TEM has more lenses [58].

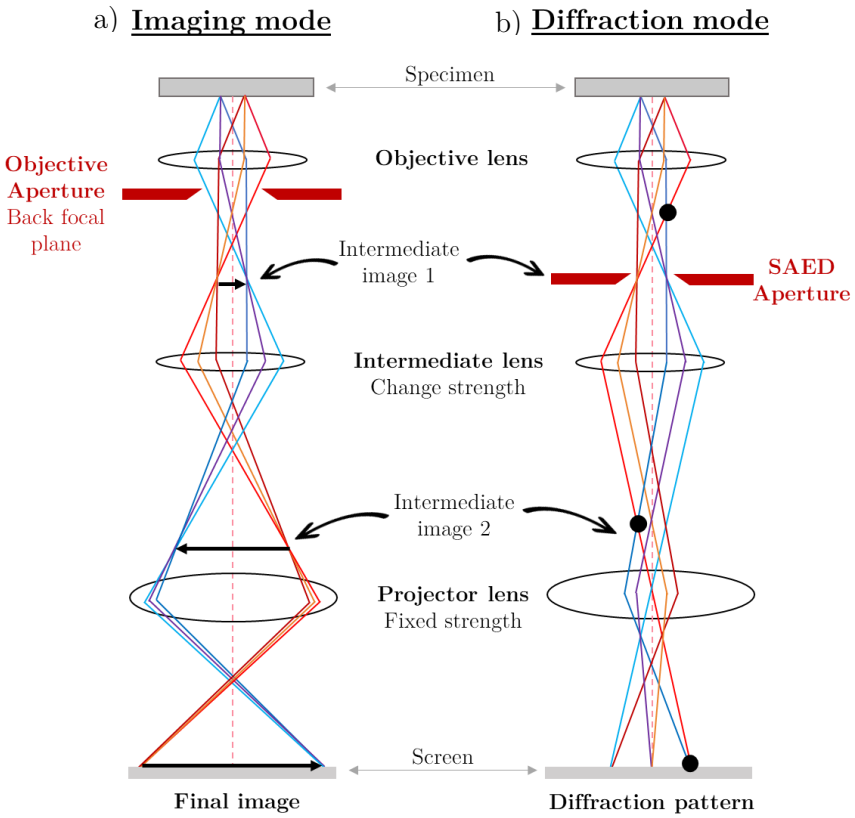

Figure 1.9: Main operating modes of a CTEM imaging system. a) Formation of a magnified image and b) Formation of a diffraction pattern. When changing the strength of the intermediate lens, either the image plane of the objective lens (magnified image a)) or the back focal plane of the objective lens is projected on the screen (diffraction pattern b)). To obtain an electron-diffraction pattern from a selected area of interest, an aperture is inserted in the image plane of the objective lens. Graphics based on [58].

In a STEM, a convergent electron probe is scanned in a raster across the specimen with the aid of scanning coils (Figure 1.10 a)). Multiple scattered signals are detected and plotted as a function of the probe position to form a magnified image [59]. In Figure 1.10 b) the primary STEM detectors that collect signals based on the scattering angle are shown:

i. (Annular) Bright field - (A)BF picks up the on-axis forward-scattered electrons (BF: $\theta_0 <$ 10 mrad and ABF: 10 mrad$< \theta_1 <$ 20 mrad).
ii. Low-Angle Annular Dark Field – LAADF is an annular detector which collects small-angle forward-scattered electrons (10 mrad $< \theta_2 <$ 50 mrad).
iii. High-Angle Annular Dark Field – HAADF collects electrons which are inelastically scattered at high angles ($\theta_3 >$ 50 mrad) due to Rutherford scattering.

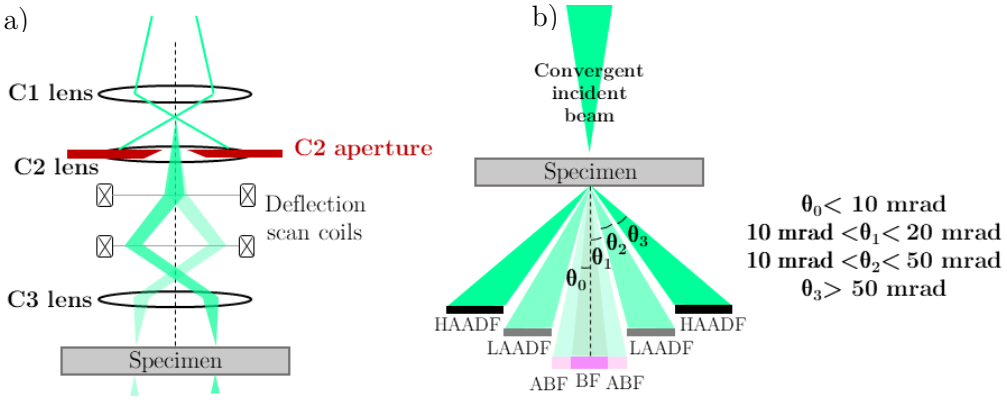

Figure 1.10: STEM system and detectors. a) Scanning system where deflection coils are used to raster the electron beam across the specimen. b) Detector in STEM: (A)BF – (annular) bright field, LAADF – low-angle annular dark field and HAADF – high-angle annular dark field. The typical angular values for each detector are listed (θ). Graphics based on [58].

1.3.2 (S)TEM contrast for ferroelectrics

TEM imaging mode can operate under different contrast mechanisms. Contrast is defined as the difference in intensity between two adjacent area. As the electron wave passes through a specimen, both its amplitude and phase can be altered and both amplitude contrast and phase contrast can contribute to the image, even if usually one of them dominates. [58]

Amplitude contrast comprises the mass-thickness contrast (the denser/thicker the specimens, the less electrons they transmit) and diffraction contrast. As diffraction contrast originates in a coherent elastic-scattering mechanism on certain crystallographic planes, it is particularly important in the realm of ferroelectrics. The domains, which represent regions with slightly different crystallographic orientations, as well as DWs, or crystallographic defects can be revealed. Friedel`s law assures an inversion-symmetric diffraction pattern for thin specimens; however, Friedel`s law can be broken due to strong dynamical scattering in polar materials; this allows contrast between domains of different polarization (the intensity of a Bragg reflection $\boldsymbol{g_{hkl}}$ is different from that of a reflection with space inversion $\boldsymbol{g_{\bar{h}\bar{k}\bar{l}}}$) [60]. In BF mode the dark contrast regions are produced from areas that are aligned for Bragg diffraction. With the use of an objective aperture which can select a certain diffracted beam (*hkl*), a dark-field (DF) image can be formed. Domains containing polarization in the particular *hkl* direction selected by the aperture will be brighter, while domains with polarization away from the selected direction will appear darker.

A phase-contrast mechanism is at the heart of high-resolution TEM (HRTEM) where lattice fringes can be imaged. The recorded image has the periodicity of the sample's crystallographic structure; however, it is not a direct representation of it because the exit wave is influenced further by the microscope conditions (defocus settings, aberrations).

Aberration-corrected STEM is widely used nowadays for ferroelectrics as it allows the imaging of individual atomic columns and a direct interpretation of atomic position. The displacements of the atoms can be mapped (e.g., A vs B or O vs B in a perovskite ferroelectric) and link to the direction of the polarization and determine, for instance, the

local polar order or the type and structure of a DW. The HAADF detector is recording mainly incoherent Rutherford scattering and gives a strong atomic-number contrast ($\sim Z^2$). HAADF does not allow the imaging of light elements (such as O). All atoms, including light elements, can be revealed by ABF where the outer section of the BF signal is collected, which, compared to BF, is incoherent and is not dominated by phase contrast. This gives a straightforward interpretation of the atomic position [61]. It should be noted that HAADF is more robust than ABF, which is more sensitive to specimen thickness and small mistilts [62]. The main advantage of STEM is that HAADF and ABF can be acquired simultaneously. LAADF is a detector collecting electrons scattered just outside the BF region. Both elastically and inelastically scattered electrons, which are partially coherent, contribute to the detected signal, which makes LAADF ideal for imaging features that diffract strongly, such as crystallographic defects or DWs [63].

1.3.3 SAED

Crystallographic information can be gathered by using electron diffraction. In diffraction mode an area of interest is selected with the aid of an aperture.

Electron diffraction is a result of Bragg scattering on the lattice planes, separated by lattice constant, d_{hkl}. Bragg's law describes the path difference between two waves that interfere constructively:

$$2d_{hkl} \sin\theta = n\lambda \tag{1.6}$$

, where θ is the scattering angle, λ is the wavelength of the radiation and n is an integer (order of reflection). The electron-diffraction pattern is the result of the collective electron scattering from successive lattice planes.

Ferroelectric/ferroelastic domains can determine the splitting of certain reflexions along characteristic crystallographic directions due to a slight mismatch between domains. SAED acquired across a DW and the analysis of reflection splitting can give information about the polar configuration and the type of DW. An example of determining the DW type by using SAED is shown in Figure 1.11. In this case, 109° and 71° DWs in polycrystalline $BiFeO_3$ have been revealed by comparing the splitting of the diffraction spots in the experimental SAED to the simulated diffraction pattern. [64]

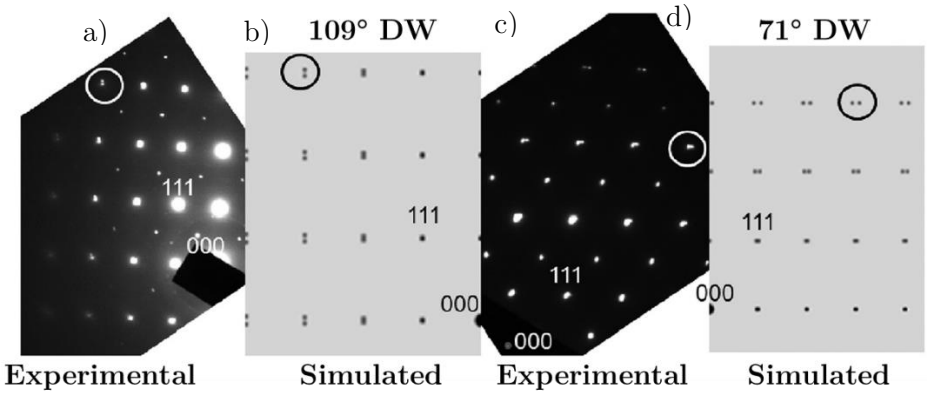

Figure 1.11: Experimental and simulated SAED from domains in $[110]_{pc}$ zone axis where splitting of the marked (333) reflections was observed in approximately the $[110]_{pc}$ direction for 109° DW (a) and b)) and in $[100]_{pc}$ for 71° DW (c) and d)). Reprinted from [64] with permission from AIP Publishing.

1.3.4 Analytical tools

The local investigation of the chemical composition in ferroelectrics by analytical tools proved to be valuable as it establishes the relationship between local chemistry and the domain structure. For instance, slight compositional variations have been shown to have an effect on the domain morphology in (K,Na)NbO_3 [65]. Concerning the DWs, the nature of point-charge defects, which tend to accumulate at the wall [66], can influence their mobility and/or their physical properties (e.g., electrical conductivity [62]). Routinely used analytical techniques in TEM are energy-dispersive X-ray spectroscopy (EDXS) and electron-energy-loss spectroscopy (EELS). EDXS analyses the X-rays generated by the inelastic interaction between the primary electron beam and the material. EELS, on the other hand, measures the energy loss during the inelastic processes of the primary beam in the specimen [67]. EELS is more suitable for detecting light elements than EDXS and overall, it has a better energy resolution. Moreover, from EELS spectra the oxidation state of the elements can be determined, and this might be particularly useful in determining and understanding the types of defects that segregate at DWs. However, EELS data is more difficult to interpret and the acquisition time is longer [68], and for that reason, EDXS and EELS are usually complementary techniques.

In addition, EELS offers the possibility to measure the specimen thickness by log-ratio relative method [69]. Equation 1.7 shows that the ratio of specimen thickness (t) to the characteristic mean free path (λ_{path}) for inelastic scattering is linked to the ratio between the total transmitted integral intensity (I) and the zero-loss peak integral intensity (I_0). An estimation of the sample thickness can aid the data interpretation and provide input for simulations (HAADF and ABF image simulation, SAED simulation, electric field distribution in the TEM specimen by finite element method simulations etc.).

$$\frac{t}{\lambda_{path}} = \ln \frac{I}{I_0} \tag{1.7}$$

1.3.5 In-situ voltage-biasing TEM

Voltage-biasing TEM experiments for ferroelectric materials bring the investigation closer to the real conditions of device operation, as an electric field is applied to the specimen while the TEM investigation is performed.

In-situ TEM offers the opportunity to locally and directly investigate fundamental domain switching phenomena (e.g., movement of DWs, change in DW properties, pinning between domains etc.).

There are diverse methods by which the electric field is applied across the TEM specimen (summarized in Figure 1.12). [70]

Early on, in-situ biasing studies on ferroelectrics were conducted on traditionally prepared **mechanically polished specimens** with central perforation produce by Ar^+ milling (Figure 1.12 a)). [71]-[75] The electric field can be either parallel or perpendicular to the electron beam, depending on the electrodes' configuration. [73] The electrodes are further connected to the in-situ holder through wires. In any case, the electrodes are relatively far from the thin area of interest and the perforation, which often has irregular geometry, causes an inhomogeneous electric field. The main advantage of this method is that the specimens have very good quality and can be very thin.

For **probe-contact in-situ holders** an electric field is applied to the specimen between a probe and a counter electrode (Figure 1.12 b)). The probe is pressed directly on the surface of the ferroelectric specimen [9] [76] [77] or on a previously deposited electrode on the specimen surface [78]. The benefit of this technique is that the electric field can be

relatively well controlled in the area of interest. However, a concern is that pressing a probe on the specimen surface causes stress and can have an effect on the switching process since polarization and strain are coupled in a ferroelectric. This geometry is more feasible for thin films than for bulk ferroelectrics (bulk ceramics or single crystals), which have large areas. [51]

State-of-the-art advances in in-situ biasing equipment are the **electrical biasing holders with integrated circuitry** for contacting microelectromechanical (MEMS) Si-based chips with patterned electrodes (Figure 1.12 c)). The chips can be designed for both heating/biasing experiments and, in that case, the patterned electrodes will be deposited on a silicon nitride membrane. While this allows very sophisticated experiments investigating simultaneously temperature- and electric-field-dependence-phenomena, the specimen preparation is challenging: electron-transparent lamellae should be transferred to the MEMS-based devices, the mechanical stability of the device should be maintained and the breakage of the silicon nitride membrane should be avoided. [79] Biasing-dedicated chips can offer a membrane-free FIB-optimized design where a pass-through notch down the middle of the chip allows for easy specimen deposition and thinning (Figure 1.12 c)). The lack of membrane gives the highest possible resolution to the microscope.

It is worth mentioning that electric field can be applied not only using a specialized in-situ biasing holder, as in the methods discussed above, but, also, through **electron-beam illumination**. A few reports have demonstrated control over the nucleation and response of domains by electron-beam illumination [80] [81]. While there is some ambiguity over the mechanism of beam-induced polarization changes [81] [82], an induced divergent radial field by positive sample charging through secondary-electron emission was thoroughly demonstrated (Figure 1.12 d)). [81] This method is advantageous because it does not require dedicated holders or special specimen preparation. Heating of the specimen due to illumination can further complicate the interpretation of results since the domain structure is sensitive to temperature changes. Moreover, the configuration of the electric field is rather complicated and depends on the illumination conditions.

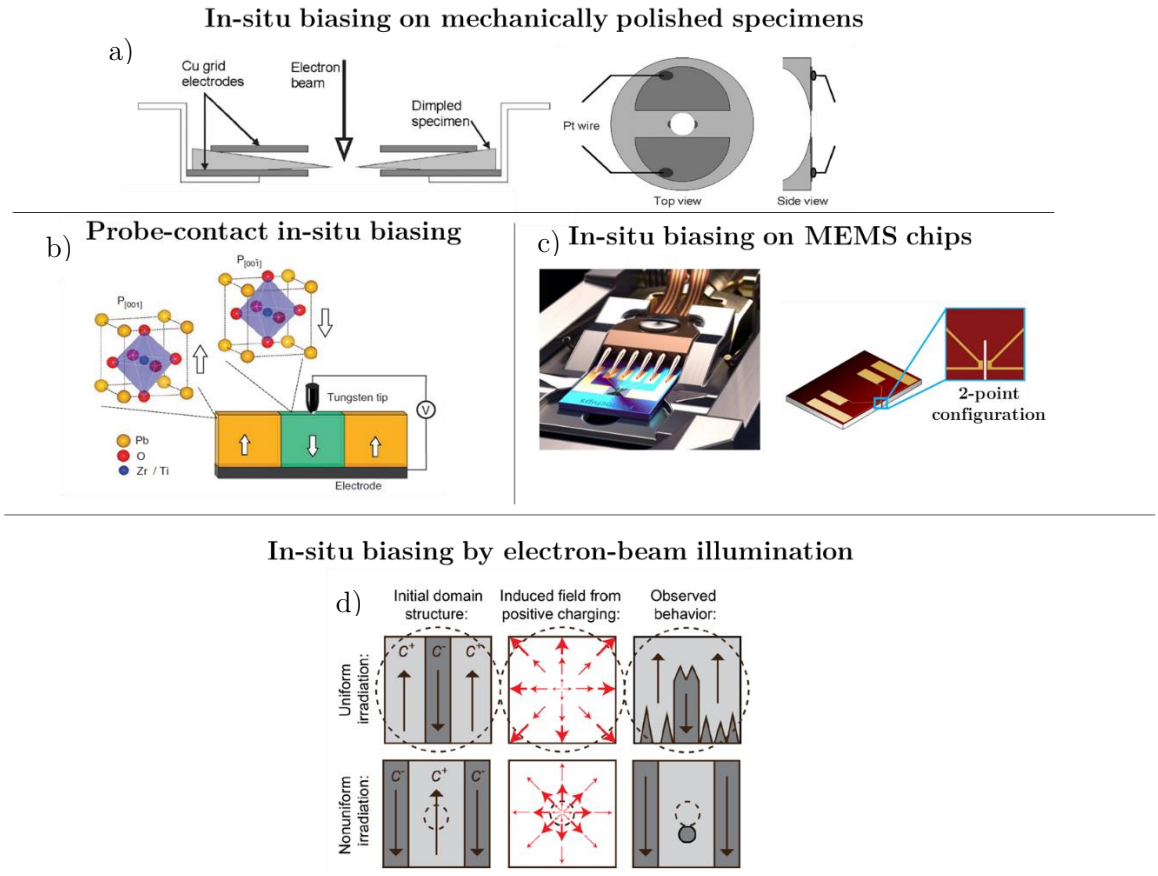

Figure 1.12: In-situ biasing systems. a) Different configurations of in-situ biasing on mechanically polished specimens. Reproduced with permission from Springer Nature [73]. b) Schematic of a probe-contact in-situ biasing performed on a ferroelectric thin film. Reproduced with permission from Springer Nature [9] c) In-situ biasing holder together with FIB-optimized biasing chip [83]. d) Schematic showing electric fields due to positive sample charging, alongside observed domain behavior in an in-situ biasing experiment by electron-beam illumination. Reprinted with permission from [81]. Copyright (2023) by the American Physical Society.

1.4 Objectives and Hypotheses of the Dissertation

The aim of the dissertation was to investigate the atomic-scale structure and voltage-driven dynamic response of domain walls in bulk lead-free ferroelectrics by transmission electron microscopy.

The first part of the dissertation investigates the morphology, structure and chemistry of uncharged and charged step-like DWs in polycrystalline $BiFeO_3$ with atomic resolution.

The dissertation is further devoted to in-situ biasing STEM experiments following the interaction of the material with the electric field.

- The second part of the dissertation aims at investigating with atomic resolution the DWs' interaction with a sub-coercive electric field in a rhombohedral $BiFeO_3$ single crystal.
- Lastly, the aim was to monitor the domain structure's evolution under an electric field of monoclinic $(K_{0.5}Na_{0.5})NbO_3$ single crystal in the presence of other interfaces (i.e, crystallographic defects, other immobile DWs, edge of the sample)

The objectives of this doctoral dissertation are the following:

1) Determine and compare the atomic-level strain distribution and structural properties of charged vs neutral step-like DWs in polycrystalline $BiFeO_3$
2) Establish a focused-ion-beam specimen preparation procedure for in-situ biasing STEM, targeting atomic resolution.
3) Investigate how the mobility of the DWs in a $BiFeO_3$ single crystal depends on their type and morphology.
4) Study at the atomic level the interaction between DWs and a subcoercive-field in a $BiFeO_3$ single crystal
5) Understand how the domain pattern evolves when an electric field is applied in situ for the case of a $(K_{0.5}Na_{0.5})NbO_3$ single crystal and how the switching is mediated by the presence of nanoscale interfaces.

This doctoral dissertation is based on the following hypotheses:

1) Nominally charged and nominally neutral DWs exhibit different strain and structural properties.
2) The response of DWs to an external electric field depends on several factors including their type, morphology, the presence of point-charge defects or different bound charge distribution.
3) Even at low fields (i.e., electric fields below the critical coercive field) various phenomena can occur at the DW level such as a change of its morphology or changes induced in the unit-cell distortion.
4) Interfaces (i.e., crystallographic defects) mediate the ferroelectric switching process.

Chapter 2

Atomically Resolved Structure of Step-Like Uncharged and Charged Domain Walls in Polycrystalline $BiFeO_3$

The morphology and structure of DWs are closely related to their functional dynamic response. [41]

In this study we analyze charge/uncharged step-like $\{100\}_{pc}$-type DWs by atomic resolution high-angle annular dark field (HAADF) in polycrystalline $BiFeO_3$.

First, we show that $\{100\}_{pc}$-type DWs can form fine atomic-level steps (1–3 unit cells), but also sharp quasi-rectangular steps with charged/uncharged segments (at least 10 unit cells per segment).

Second, we compare nominally uncharged (UDW) and nominally charged (CDW) tail-to-tail $\{100\}_{pc}$-type DWs. Our experimental results show that UDWs exhibit a higher strain in terms of unit-cell -distortion of the Bi sublattice than the tail-to-tail CDWs. Simulations of HAADF images establish that higher strain on nominally uncharged $\{100\}_{pc}$-type DWs is primarily intrinsic due to crystallographic mismatch rather than chemical strain as the amount of Bi vacancies probed by a Bi intensity evaluation is comparable on both types of DWs. Therefore, although the formation of CDWs is energetically unfavorable from an electrostatic point of view, these DWs are more elastically compatible than their neutral counterparts. These results will add to the general knowledge of CDWs, which are energetically costly and whose formation is not well understood.

In terms of structure, derived from an Fe-displacement map relative to the Bi sublattice, CDWs are found to be statistically wider (10 vs. 5 unit cells), which can be associated with a broader strain distribution. In contrast, the strain is concentrated in the center of the wall for the UDWs. Both UDWs and CDWs have a non-Ising profile, where the Fe-displacement vector changes both magnitude and orientation at the wall.

Significant differences for charged and uncharged DWs could suggest a different role in the switching behavior.

This chapter addresses thesis objective 1.

Published in: O. Condurache, G. Dražić, N. Sakamoto, T. Rojac, and A. Benčan, "Atomically resolved structure of step-like uncharged and charged domain walls in

polycrystalline $BiFeO_3$," *Journal of Applied Physics*, vol. 129, no. 5, pp. 054102, 2021, https://doi.org/10.1063/5.0034699

My contribution: I analyzed the HAADF-STEM images and determined the atomic-displacement, strain and intensity maps. I interpreted the results, elaborated the concept of the manuscript and wrote the paper, together with the co-authors.

Journal of Applied Physics ARTICLE scitation.org/journal/jap

Atomically resolved structure of step-like uncharged and charged domain walls in polycrystalline $BiFeO_3$

Cite as: J. Appl. Phys. **129**, 054102 (2021); doi: 10.1063/5.0034699
Submitted: 22 October 2020 · Accepted: 8 January 2021 ·
Published Online: 2 February 2021

Oana Condurache,[1,2,a)] Goran Dražić,[1,2,3] Naonori Sakamoto,[4] Tadej Rojac,[1,2] and Andreja Benčan[1,2]

AFFILIATIONS

[1]Electronic Ceramics Department, Jozef Stefan Institute, 1000 Ljubljana, Slovenia
[2]Jozef Stefan International Postgraduate School, 1000 Ljubljana, Slovenia
[3]Department of Materials Chemistry, National Institute of Chemistry, 1000 Ljubljana, Slovenia
[4]Research Institute of Electronics, Shizuoka University, 3-5-1 Naka-ku, Hamamatsu, Japan

Note: This paper is part of the Special Topic on Domains and Domain Walls in Ferroic Materials.
[a)]**Author to whom correspondence should be addressed:** oana.condurache@ijs.si

ABSTRACT

The dynamics of domain walls (DWs) during polarization switching has a great influence on the electromechanical response of ferroelectrics. To understand the influence of DWs on the functional performance of the material, their local structure and properties must be revealed. There are many investigations of the DWs in ferroelectric thin films, while investigations of the DWs in polycrystalline ferroelectrics are fewer. Here, we report on a comparative study of uncharged and charged ("tail-to-tail") DWs in $BiFeO_3$ ceramics from the point of view of the atomically resolved strain and structure using scanning-transmission electron microscopy. Both types of DWs have a step-like morphology and have a non-Ising behavior. The strain, expressed as the unit-cell distortion, is higher and more concentrated in the case of uncharged walls, which we associate with a narrower transition region of the Fe-displacement vectors. Conversely, in the case of "tail-to-tail" charged DWs, the unit-cell distortion is smaller and more dispersed because of the wider transition region of the Fe-displacement vectors. All the types of step-like DWs reported here, regardless of their charge state, exhibit a comparable amount of Bi-vacancies segregation. Further details about the structural differences are discussed from the point of view of the Fe-displacement evolution through the wall for uncharged/"tail-to-tail" charged DWs. The results are useful as they provide an insight into the local structure and chemistry of charged and uncharged DWs in polycrystalline $BiFeO_3$.

I. INTRODUCTION

Domain walls (DWs) in ferroelectrics are nanoscale topological features that mark the transition between regions with homogeneous orientations of the polarization. DWs can have different properties than the domains themselves;[1,2] furthermore, they are dynamic interfaces as they can be moved, erased, and thus manipulated by means of external electric or mechanical fields. There are two strong motivations to study the complexity of the physics and chemistry of DWs in ferroelectrics at the atomic scale. First, the unique electrical properties that the walls can possess, in combination with their dynamic nature under an applied electric field, provide to the DWs with the potential to become "the device."[3] New applications have been proposed for so-called "non-volatile, ferroelectric, domain-wall memories," where the memory binary state, rather than relying on the conventional polarization state during domain switching, is determined by writing and erasing a particular conductive DW in $BiFeO_3$ (BFO).[4] Second, the interphases in ferroelectrics together with the intrinsic lattice distortion can significantly affect the macroscopic electromechanical response of the material.[5–8] For example, in $(K,Na)NbO_3$-based ceramics, it has been shown that up to 80% of the electric-field-induced macroscopic strain, which is important in, e.g., piezoelectric actuators, can originate from a non-180° DW-switching contribution.[9]

Journal of Applied Physics ARTICLE scitation.org/journal/jap

The dynamics of DWs is directly influenced by their structure and morphology. Several studies have shown that DWs are not simple, straight interfaces, but that their morphology and structure can be rather complex.[9–14] For example, Lubk *et al.* showed that DWs in BFO thin films can be rough and produce lattice-wise steps at the atomic level.[11] In contrast, no such reports exist for polycrystalline BFO. Reports of morphological features are of particular importance as theoretical studies have shown that steps at the DWs increase their mobility and should thus strongly affect the DW dynamics.[11,15]

Studies of DWs are further complicated by the presence of walls that carry an internal bound charge due to there being a nonzero component of polarization that is perpendicular to the domain-wall plane. These walls are usually referred to as charged walls. Depending on the direction of the polarization vector on either side of the wall, DWs are formally referred to as uncharged DWs (UDWs) if they have a "tail-to-head" or "head-to-tail" configuration, or charged DWs (CDWs) if they have a negative "tail-to-tail" or a positive "head-to-head" configuration. A "tail-to-tail" or "head-to-head" DW is often considered "strongly" charged as opposed to a "weakly" charged DW (which is a "tail-to-head" or a "head-to-tail" but the electro-neutrality is broken locally in the DW region).[16] In this paper, by CDWs we will refer only to "tail-to-tail"- or "head-to-head"-type DWs. Despite their obvious energetic cost of formation, "strongly" charged DWs have been experimentally observed in different systems.[16] It is not yet clear how the intrinsic charge state of the DW determines its structure and morphology because comparative studies between CDWs and UDWs that are present in the same ferroelectric system remain scarce. As an illustration, for an epitaxial $PbZr_{0.2}Ti_{0.8}O_3$ thin film, it was shown that the charged DWs can be thicker than the uncharged ones.[17] A comparative study at the atomic level of the structure of charged and uncharged DWs in BFO thin films was performed by Wang *et al.*,[18] which showed a one-dimensional lattice-strain modulation for charged DWs, that is otherwise not present for the uncharged DWs. In the case of BFO, charged DWs are often ignored in calculations,[19–21] but they are more often reported in experimental studies of BFO thin films.[22,23] To the best of our knowledge, the presence of "tail-to-tail"- or "head-to-head"-type CDWs in polycrystalline BFO has not yet been reported.

It cannot be argued that studies of BFO thin films provide an important insight into various phenomena related to DWs. However, it must be emphasized that in thin-film structures, either polycrystalline or single crystalline (epitaxial), the electric, and elastic constraints (e.g., the presence of epitaxial strain or the unique size-effect phenomena) are different from those in the bulk. Furthermore, it was shown in a number of studies how the domain pattern in epitaxial thin films can be strongly controlled and depends on growth parameters such as growth rate,[24] oxygen partial pressure during growth,[25] thickness,[26] or the choice of the substrate.[27] Consequently, it is reasonable to assume that the properties of the DWs in thin films differ from those in a conventionally sintered polycrystalline system. Although one could expect that the local properties in a polycrystalline material with randomly oriented grains would average and give a small overall contribution, it has been shown that the local properties of DWs in $BiFeO_3$ ceramic, such as the elevated electrical conductivity, interfere with their mobility, resulting in a considerable effect on the macroscopic properties.[28]

In this study, we investigate the morphology and structure of uncharged and "tail-to-tail"-charged step-like ferroelastic DWs in polycrystalline BFO using the high-angle annular-dark-field scanning-transmission electron microscopy (HAADF-STEM) technique with atomic resolution. The aim was to understand the local structural differences between the uncharged and charged DWs. We found that both types of DWs can form step-like kinks. In contrast to CDWs, the uncharged walls have a higher and more concentrated strain, coupled with a narrower transition region and an abrupt change in the displacement vector across the wall. We were thus able to show directly that CDWs and UDWs have different structural properties. The results help us in understanding the so far unrevealed local structural and chemical aspects of the rather unusual CDWs and more conventional UDWs in polycrystalline BFO.

II. EXPERIMENTAL PROCEDURE

$BiFeO_3$ ceramics were synthesized using a mechanochemically activation preparation technique. Mechanochemically activated powders were compacted and sintered for 6 h at 760 °C using a heating and cooling rate of 5 °C/min. Details of the synthesis procedure are given elsewhere.[28] Atomic-scale investigations of the DWs were performed using a Cs-corrected scanning-transmission electron microscope (STEM) from Jeol Ltd., a Jeol ARM 200CF, operating at 200 kV. The collection semi-angle of the high-angle annular-dark-field (HAADF) detector was 68–180 mrad. The coordinates of the intensity maxima of the atomic columns were determined from HAADF images using a 2D Gaussian fit. The normalized Bi-column intensities were determined using a previously reported method,[29,30] in which the detector's background intensity is subtracted from the intensity of each pixel in the raw HAADF image. The intensities of the atomic columns were extracted by the integration of the pixel values within one sigma, approximating a Gaussian-type intensity distribution. For further details about this analysis, see Refs. 30 and 31. The samples for the STEM analysis were prepared using a conventional method: the sample was ground down to 100 μm, dimpled to 12 μm and, finally, thinned to electron transparency using a Gatan PIPS ion-milling system. The thickness of the analyzed areas was between 30 and 50 nm.

III. RESULTS AND DISCUSSION

A. Morphology of step-like $\{100\}_{pc}$-type DWs at the atomic scale

We commence by showing three different regions in the sample, each containing a $\{100\}_{pc}$-type DW (pc refers to pseudocubic). We describe a DW as being $\{100\}_{pc}$ type if it lies in the $\{100\}_{pc}$ family of planes. The atomic-level structure of the DW was extracted from HAADF-STEM images [Figs. 1(a)–1(c)], acquired in the $[100]_{pc}$ zone axis by measuring the direction and magnitude of the projected Fe displacements from the center of the Bi sublattice for each projected unit cell.

Journal of Applied Physics ARTICLE scitation.org/journal/jap

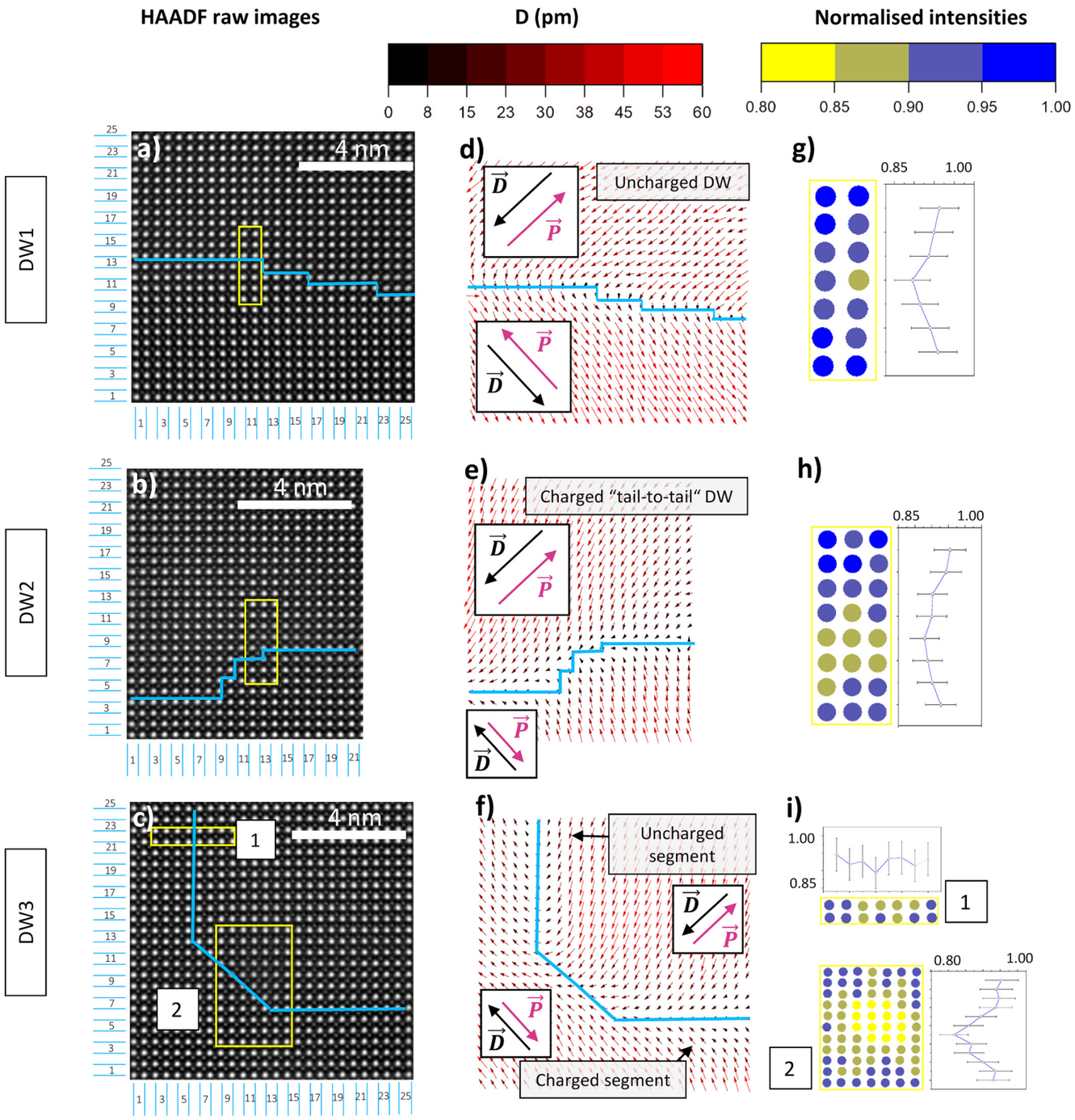

FIG. 1. (a)–(c) HAADF images in $[100]_{pc}$ zone axis of *DW1*, *DW2,* and *DW3* area, respectively. Blue line marks the middle of the domain-wall region. (d)–(f) Fe off-center displacement mapping (with respect to the Bi sublattice center) for *DW1*, *DW2,* and *DW3* area, respectively. The charged/uncharged regions of the DWs are marked. In the inset, the direction and orientation of the projected Fe off-centric displacements ($\vec{D}$) and the corresponding direction of the projected polarization ($\vec{P}$) on either side of the wall are shown. (g)–(i) Bi-intensity maps across the domain-wall regions marked with a yellow rectangle in (a)–(c), together with the corresponding intensity-line profile. Bars represent 5% relative uncertainty.

Journal of Applied Physics ARTICLE scitation.org/journal/jap

We present three kinds of $\{100\}_{pc}$-type DWs: (1) an UDW having step-like features [*DW1* in Fig. 1(d)]; (2) a CDW that has similar steps to *DW1* [*DW2* in Fig. 1(e)] and (3) a wall that has a quasi-rectangular step, having charged/uncharged segments [*DW3* in Fig. 1(f)].

We found that *DW1* and *DW2* have a staircase-like morphology. *DW1* has fine steps of 1–2 unit cells, while *DW2* has a larger step-height range of 1–3 unit cells. Roughness in the form of step-like kinks was previously reported for La-doped $BiFeO_3$ thin films,[11] and their presence was linked to the enhanced mobility of DWs when switching under an electric field.[11,15] On the other hand, *DW3* has a different morphology consisting of a sharp, quasi-rectangular step, forming relatively large (at least 10 unit cells) charged/uncharged segments. A similar step-like morphology was seen to occur when the DW is pinned on edge dislocations;[32] however, as seen from the HAADF image, *DW3* appears to be free of any other visible crystallographic defects, except the wall itself [Fig. 1(c)].

We went on and evaluated the charge state of the analyzed DWs considering the Fe-displacement vector maps [Figs. 1(d)–1(f)] and taking into account that the projected Fe-displacement vector has an opposite orientation to that of the projected polarization vector.[33] We found that *DW1* is overall a $\{100\}_{pc}$-type UDW [Fig. 1(d)], *DW2* is a "tail-to-tail" CDW [Fig. 1(e)] and *DW3* represents uncharged and "tail-to-tail"-charged segments [Fig. 1(f)]. Note that *DW1* has an overall "head-to-tail" configuration even if locally (at the step) the "head-to-tail" configuration is disrupted; likewise, in *DW2,* the "tail-to-tail" configuration is locally disrupted.

We must point out that the CDWs (i.e., *DW2* or the charged segment of *DW3*) are observed without a particular treatment, i.e., after a conventional sintering process, and, thus, were formed spontaneously despite the high electrostatic energy requirements.[34] While reported in BFO thin films[18,22] and in BFO single crystal,[12] CDWs formed spontaneously have not yet been observed directly in polycrystalline BFO.

In rhombohedral symmetry of BFO (space group $R3c$[18]), the spontaneous polarization can lie along one of the four diagonals in the pseudocubic perovskite unit cell (along the $[111]_{pc}$ direction) which leads to three different types of DWs: 71°, 109°, and 180°. These DW types are distinguished depending on the number of the reversed sign of the polarization components (x,y,z) of a given domain with respect to the polarization components of the adjacent domain. In the case of 71°, 109°, and 180° DW, either one, two or all the three signs of the polarization components are reversed, respectively.[18] Based on the assumptions that we present in supplementary material 1, we were able to conclude that *DW1* is a 109° UDW, *DW2* can be either a 109° CDW of $\{100\}_{pc}$ type or a 71° CDW of $\{100\}_{pc}$ type, and *DW3* presents charged/uncharged segment of a 109° DW on $\{100\}_{pc}$. A detailed explanation of the DW-type identification together with a three-dimensional representation of the possible polarization configuration on either side of *DW1*, *DW2*, and *DW3* is shown in supplementary material 1.

Previous studies[30,31] revealed the segregation of Bi vacancies at UDWs in BFO ceramics, owing to the electrostatic and elastic forces driving the defect diffusion at the walls. Motivated by these studies, in the next step, we probed the presence of Bi vacancies by mapping locally the intensities of the Bi atomic columns [Figs. 1(g)–1(i)]. As seen in Fig. 1(g), the variation in intensity of the Bi columns across the *DW1* (uncharged 109° DW) is around 5%–10%, indicating the presence of Bi vacancies. Considering that DWs are strained crystallographic defects, the intensity of the atomic columns in the STEM can undergo fluctuations due to the presence of the associated strain fields. These fluctuations are usually below 5%:[35,36] therefore, we can link the 5%–10% drop in the intensity at *DW1* to the presence of Bi vacancies segregating at this DW. Using the same intensity-evaluation methodology, a much prominent intensity drop (~20% relative) for the Bi columns in straight 109° UDWs (i.e., without the step features as shown here for *DW1*) have been previously reported for BFO ceramics.

A similar drop in the Bi atomic column intensity (5%–10%) was found for *DW2* [Fig. 1(h)]. Since the orientation of the projected polarization vector is opposed to that of the projected Fe displacement,[33] *DW2* is a "tail-to-tail" wall [Fig. 1(e)] and consequently, it should be negatively charged. Since Bi vacancies are also expected to be negatively charged (i.e., V_{Bi}''' in the Vink Kroger notation), their presence at the negatively charged "tail-to-tail" *DW2* is unexpected. While this situation would need further investigation, the compensation of the "tail-to-tail" DW is probably driven by a complex interplay between the strain relaxation, which is provided by Bi vacancies,[31] and screening by positively charged defects, e.g., Fe^{4+}[30,31] or O vacancies.[22]

In the case of *DW3*, we confirm for the uncharged segment an intensity drop of 5%–10% for the Bi atomic columns [Fig. 1(i), upper map] and for the charged segment we found close to the tip of the step that the intensity of the Bi atomic columns drops by ~20% relative to the average intensity measured inside the domain itself [Fig. 1(i), bottom map], suggesting a concentrated segregation of Bi-vacancy defects at the corner of the rectangular step.

B. Comparison between charged and uncharged $\{100\}_{pc}$-type DWs

We discuss next how the lattice strain and the local atomic off-center displacements at the $\{100\}_{pc}$-type DWs depend on the charged state of the wall. We remind the reader that we cannot identify the exact type of *DW2*: it can be either a 71° "tail-to-tail" CDW on $\{100\}_{pc}$, or a 109° "tail-to-tail" CDW on $\{100\}_{pc}$. However, according to Wang *et al.*,[18] it is the plane in which DW lie rather than their angle labelled type that dictates the structure of charged DWs. Wang *et al.*[18] showed that charged 71° DWs on $\{100\}_{pc}$ and charged 109° DWs on $\{100\}_{pc}$ present similar structural characteristics. In contrast, charged 109° DWs on $\{100\}_{pc}$ are considerably different than charged 109° DWs that lie on $\{110\}_{pc}$. Thus, we believe that not knowing whether *DW2* is a 71° DW or a 109° DW does not restrict a valuable comparison between the uncharged and charged $\{100\}_{pc}$-type DWs.

The comparison between the charged and uncharged ferroelastic DWs in $BiFeO_3$ is particularly relevant for understanding the differences between the functional behavior of this type of DWs (such as the switching mechanism and the interaction with point defects), since the analysis is performed in the same experiment, with the same specimen and for DWs that have a similar morphology (i.e., step-like morphology).

Journal of Applied Physics ARTICLE scitation.org/journal/jap

1. Lattice distortion

Figure 2 shows the distortion of the unit cell perpendicular to the wall plane for *DW1* [Fig. 2(b)], *DW2* [Fig. 2(c)], and *DW3* [Figs. 2(d) and 2(e)]. The lattice at the DW is distorted mainly in the direction perpendicular to the DW plane, as shown in a previous study.[31] In supplementary material 2, the lattice distortion parallel to *DW1* and *DW2* is also presented. We calculated the lattice strain in the form of the unit-cell distortion [as schematically presented in Fig. 2(a)] using the Bi sublattice from the same area of the HAADF images shown in Fig. 1.

In the case of uncharged $\{100\}_{pc}$-type walls [*DW1*, Fig. 2(b), and the uncharged segment of *DW3*, Fig. 2(d)], we found experimentally that the lattice distortion is located in the middle of the wall with a distortion angle of 3.0°–4.5°. On the other hand, in the case of charged $\{100\}_{pc}$-type walls [*DW2*, Fig. 2(c), and the charged segment of DW3, Fig. 2(e)], the strain in the wall area is much lower (a distortion angle smaller than 3°) and more diffuse. Previous atomic-structure analyses[20] showed that DWs in BFO are strained such that the Bi sublattice exhibits shearing, while the Fe sublattice is practically unaffected when crossing the DW. This intrinsic Bi shear strain can be largely affected by the presence of Bi vacancies accumulated at the walls.[31] Here, we show that the relative intensity decrease of the Bi atomic columns in the wall region is comparable for the charged and uncharged regions (~10%, as shown in Fig. 1). Thus, the data suggest that there is no significant difference in the Bi-vacancies concentration between the CDWs and UDWs, meaning that the difference in the Bi-lattice shear values for the charged and uncharged $\{100\}_{pc}$-type walls can be explained as a pure, intrinsic lattice mismatch. The lattice mismatch is higher in the case of uncharged $\{100\}_{pc}$-type walls than in the case of charged $\{100\}_{pc}$-type walls, as confirmed by the analysis shown in supplementary material 3, where the theoretical unit-cell distortion for uncharged-, charged-"tail-to-tail"- and charged-"head-to-head" $\{100\}_{pc}$-type walls was evaluated from a simulated HAADF-STEM image. The results in supplementary material 3 show that the intrinsic shear is much higher at the uncharged wall. Therefore, even though the formation of CDWs is energetically unfavorable from an electrostatic point of view, these DWs are elastically more compatible than the UDWs, resulting in a lower elastic cost during their formation.[20]

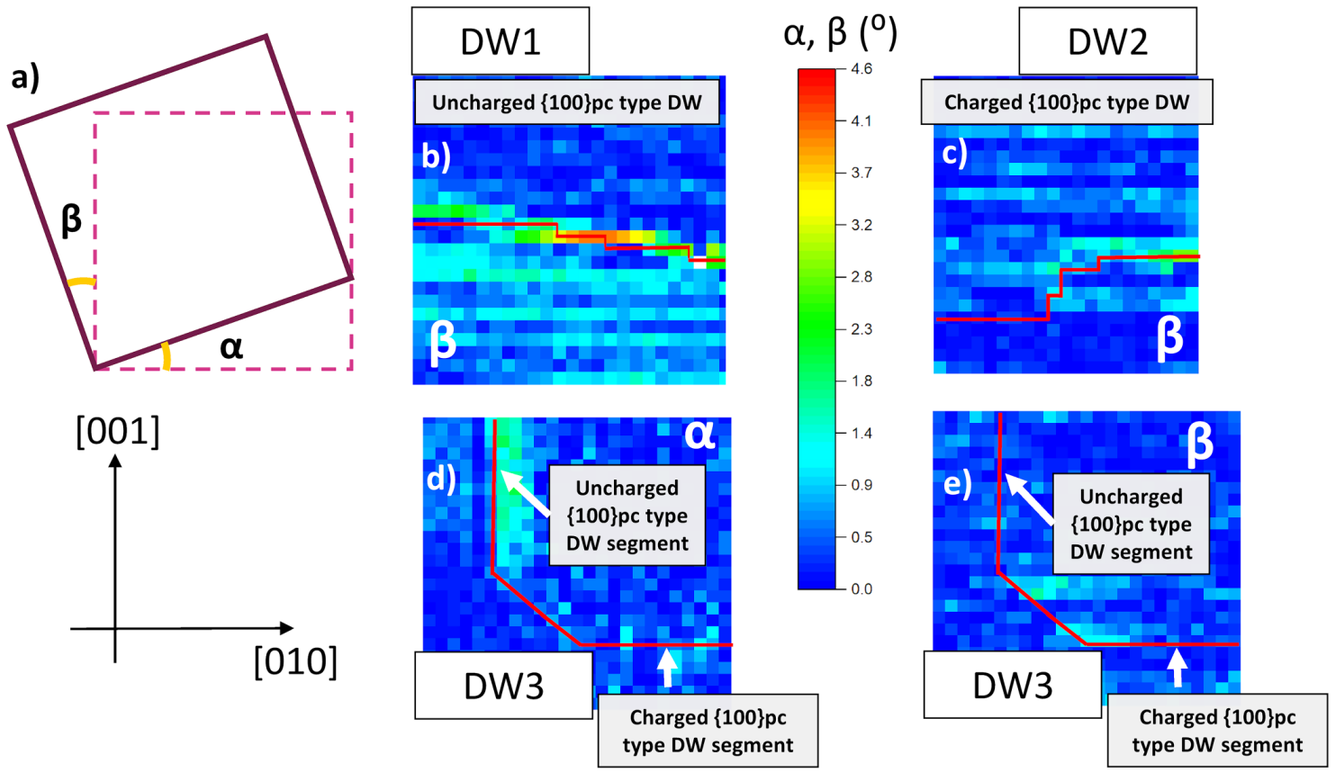

FIG. 2. Unit-cell distortion of the Bi sublattice. (a) Schematic representation of the unit-cell distortion angles. α and β are the distortion angles in the [010] and [001] directions, respectively. Hence, β is the distortion angle perpendicular to *DW1*, *DW2* and the charged segment of *DW3*, while α is the distortion angle perpendicular to the uncharged segment of *DW3* (b), (c) Unit-cell distortion of the Bi sublattice (β) normal to the wall plane for the *DW1* and *DW2* regions, respectively. (d) and (e) Unit-cell distortion of the Bi sublattice for the *DW3* region normal to the uncharged segment (α) and normal to the charged segment (β), respectively. Red line marks the middle of the domain-wall region.

Journal of Applied Physics ARTICLE scitation.org/journal/jap

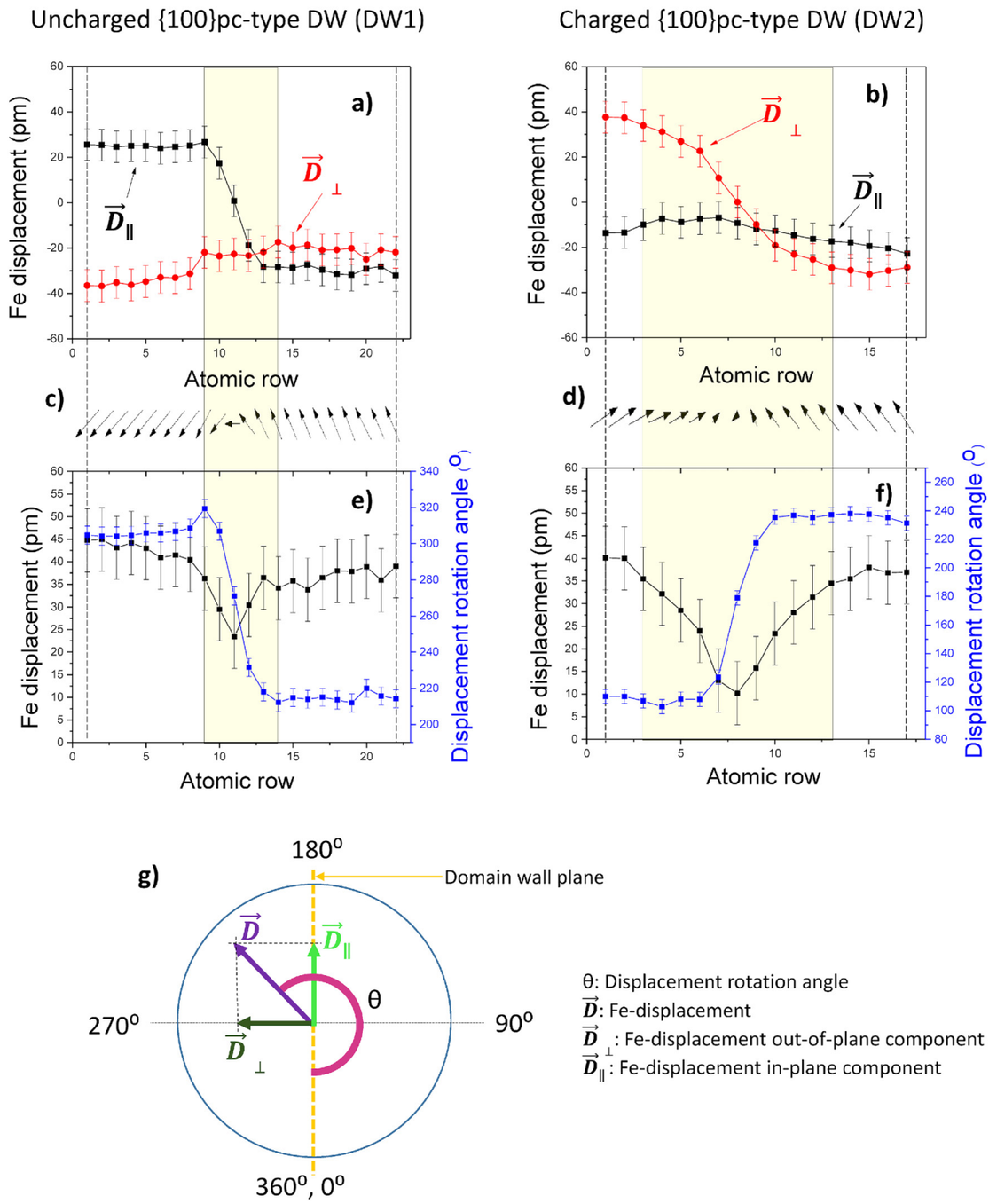

FIG. 3. (a) and (b) Out-of-plane (red curve) and in-plane component (black curve) of average Fe displacements with respect to the wall plane for *DW1* and *DW2*. The error bar represents a ±7 pm uncertainty. (c) and (d) Representation of average Fe-displacement vector in the *DW1* and *DW2* regions according to the magnitude and rotation angle shown in (e) and (f). (e) and (f) Average magnitude and rotation angle of Fe-displacement vector from one domain to another in the case of $\{100\}_{pc}$-type uncharged DW (*DW1*) and $\{100\}_{pc}$-type charged DW (*DW2*). The error bar represents a ±7 pm uncertainty for the Fe-displacement evaluation and ±5° for the rotation-angle evaluation[11] (g) Geometric schematic of Fe-displacement vector ($\vec{D}$) decomposed into out-of-plane component ($\vec{D}_{\perp}$) and in-plane component ($\vec{D}_{\parallel}$) with the corresponding displacement rotation angle (θ). The DW transition region (DW width) is marked with a yellow frame. The width was defined from the region where the in-plane and/or out-of-plane component of the displacement shows a significant change.

Journal of Applied Physics ARTICLE scitation.org/journal/jap

2. Atomic off-center displacements

We further investigated how the structure of the DW depends on its charge state. For the sake of a comparison, we analyzed the average projected Fe-displacement evolution across the DW from one domain to the other in *DW1* and *DW2* (Fig. 3).

We analyzed, in the first place, the decomposition of the Fe-displacement vectors into in-plane and out-of-plane components [Figs. 3(a) and 3(b)], followed by the total off-centric Fe-displacement magnitude and angle [Figs. 3(c)–3(f)]. The basic geometrical relationships used in the analysis are schematically explained in Fig. 3(g). Based on our experimental observation, the Fe-displacement vector across the DW evolves differently in UDWs and CDWs.

In Figs. 3(a) and 3(b), we present the decomposed Fe displacements parallel and perpendicular to the plane of the DW. The displacement component that is parallel to the wall has a significant change for the uncharged DW [Fig. 3(a), black data] and the displacement component perpendicular to the wall has a significant change for the charged DW [Fig. 3(b), red data]. The variations in the displacement components support the uncharged and charged configurations of *DW1* and *DW2*, respectively.

A further observation is that the transition region in which the Fe-displacement vector changes in magnitude and orientation is wider for the CDW than for the UDW [∼5 unit cells for *DW1*, Fig. 3(e), vs ∼10 unit cells for *DW2*, Fig. 3(f)]. Additionally, we made a statistical analysis considering the different locations across the charged/uncharged step-like DWs. We found that the DW width is greater in the case of the charged DWs (∼10 uc) than for the uncharged DWs (∼6 uc), which confirms our conclusions (see supplementary material 4). This is consistent with a previous report showing that CDWs in epitaxial $PbZr_{0.2}Ti_{0.8}O_3$ thin films are wider than the UDWs.[16] We can link a more abrupt Fe-displacement transition for the UDW [Fig. 3(e)] to a more concentrated strain in the middle of the wall [Fig. 2(b)]. Conversely, a smaller and more dispersed strain for the CDW [Fig. 2(c)] can be associated with a more diffuse transition of the displacement from one domain area to another [Fig. 3(f)].

Second, in both cases, the displacement vector reduces its magnitude and it also rotates through the DW, revealing a non-Ising behavior [see angle evolution in Figs. 3(e) and 3(f)]. Non-Ising behavior was previously theoretically predicted for 109° uncharged DWs in BFO[19] and experimentally shown for charged 109° DWs in BFO thin films.[22] Significant differences in their structure, suggest that CDWs and UCDs might have a different role in the switching mechanism; however, further studies are required.

IV. CONCLUSIONS

The focus of this study was on the morphology and structure of charged and uncharged $\{100\}_{pc}$-type DWs in polycrystalline BFO. We have shown that the morphology of both types of $\{100\}_{pc}$-type DWs can be complex and form step-like kinks. We found DWs that have different roughness, such as charged-"tail-to-tail" and uncharged DWs that have small steps with a width of ∼1–4 units cells, and a DW that has a sharp, rectangular step that forms charged/uncharged segments of at least ∼10 unit cells. Bi vacancies were found to segregate at the analyzed step-like DWs, regardless of their intrinsic charge nature; a higher degree of Bi-vacancies accumulation was found at the large sharp step. In addition, we structurally compared the charged "tail-to-tail" and the uncharged $\{100\}_{pc}$-type DWs. We show that the uncharged $\{100\}_{pc}$-type DWs have a larger associated lattice strain than the charged-"tail-to-tail" $\{100\}_{pc}$-type DWs, and we were able to explain the result as a pure intrinsic lattice mismatch. This result is an indication that the formation of charged DWs is energetically costly from an electrostatic point of view, compared to the formation of uncharged DWs, but at the same time, it is energetically favorable from the point of view of lattice compatibility. We associate a higher and more concentrated strain for the uncharged $\{100\}_{pc}$ type to a more abrupt and narrower transition of the Fe-displacement vector through the DW. In addition, both charged and uncharged DWs exhibit a non-Ising behavior, i.e., they exhibit the simultaneous rotation and reduction of the Fe-displacement vector across the DW. Since the $\{100\}_{pc}$-type DWs have been experimentally shown to be intrinsically different in strain distribution and structure, we assume that their role in the switching mechanism will be different, depending on their particular strain and charged state, as indicated by this study. We hope that these results will generate interest in future studies, theoretical or experimental, aimed at understanding the influence of the structural differences of DWs on their mobility in polycrystalline BFO.

SUPPLEMENTARY MATERIAL

See the supplementary material for schematics of possible polarization configurations on either side of *DW1*, *DW2*, and *DW3* (supplementary material 1); representation of unit-cell distortion of the Bi-sublattice parallel to the *DW1* and *DW2* planes (supplementary material 2); the simulated projected unit-cell distortion for uncharged, charged-"tail-to-tail" and charged-"head-to-head" $\{100\}_{pc}$-type DW (supplementary material 3); and statistics on different locations of the DW width for charged and uncharged step-like DWs (supplementary material 4).

ACKNOWLEDGMENTS

The work was carried out within the Research Program P2-0105, Project Nos. J2-2497 and PR-08978 (Slovenian Research Agency). Part of this work was carried out under the Cooperative Research Project Program of Research Institute of Electronics, Shizuoka University. Part of this research was also supported by the Collaborative Research Project of Laboratory for Materials and Structures, Institute of Innovative Research, Tokyo Institute of Technology. Ms. Maja Makarovič is acknowledged for the BFO sample preparation. Ms. Brigita Kmet is acknowledged for the TEM sample preparation.

DATA AVAILABILITY

The data that support the findings of this study are available within the article and its supplementary material.

REFERENCES

[1]G. Catalan, in *Mesoscopic Phenomena in Multifunctional Materials*, edited by A. Saxena and A. Planes (Springer-Verlag, Berlin Heidelberg, 2014), pp. 225–247.

Journal of Applied Physics ARTICLE scitation.org/journal/jap

[2]J. Seidel, L. W. Martin, Q. He, Q. Zhan, Y.-H. Chu, A. Rother, M. E. Hawkridge, P. Maksymovych, P. Yu, M. Gajek, N. Balke, S. V. Kalinin, S. Gemming, F. Wang, G. Catalan, J. F. Scott, N. A. Spaldin, J. Orenstein, and R. Ramesh, Nat. Mater. **8**, 229 (2009).
[3]G. Catalan, J. Seidel, R. Ramesh, and J. F. Scott, Rev. Mod. Phys. **84**, 119 (2012).
[4]P. Sharma, Q. Zhang, D. Sando, C. H. Lei, Y. Liu, J. Li, V. Nagarajan, and J. Seidel, Sci. Adv. **3**, e1700512 (2017).
[5]M. Davis, D. Damjanovic, and N. Setter, J. Appl. Phys. **100**, 084103 (2006).
[6]A. Pramanick, D. Damjanovic, J. E. Daniels, J. C. Nino, and J. L. Jones, J. Am. Ceram. Soc. **94**, 293 (2011).
[7]N. H. Khansur, H. Kawashima, S. Wada, J. M. Hudspeth, and J. Daniels, Acta Mater. **98**, 182 (2015).
[8]D. A. Ochoa, G. Esteves, T. Iamsasri, F. Rubio-Marcos, J. F. Fernández, J. E. García, and J. L. Jones, J. Eur. Ceram. Soc. **36**, 2489 (2016).
[9]J. Gonnissen, D. Batuk, G. F. Nataf, L. Jones, A. M. Abakumov, S. Van Aert, D. Schryvers, and E. K. H. Salje, Adv. Funct. Mater. **26**, 7599 (2016).
[10]G. De Luca, M. D. Rossell, J. Schaab, N. Viart, M. Fiebig, and M. Trassin, Adv. Mater. **29**, 1605145 (2017).
[11]A. Lubk, M. D. Rossell, J. Seidel, Q. He, S. Y. Yang, Y. H. Chu, R. Ramesh, M. J. Hÿtch, and E. Snoeck, Phys. Rev. Lett. **109**, 047601 (2012).
[12]C.-L. Jia, L. Jin, D. Wang, S.-B. Mi, M. Alexe, D. Hesse, H. Reichlova, X. Marti, L. Bellaiche, and K. W. Urban, Acta Mater. **82**, 356 (2015).
[13]Q. H. Zhang, L. J. Wang, X. K. Wei, R. C. Yu, L. Gu, A. Hirata, M. W. Chen, C. Q. Jin, Y. Yao, Y. G. Wang, and X. F. Duan, Phys. Rev. B **85**, 020102 (2012).
[14]G. F. Nataf, M. Guennou, J. M. Gregg, D. Meier, J. Hlinka, E. K. H. Salje, and J. Kreisel, Nat. Rev. Phys. **2**, 634 (2020).
[15]R. C. Miller and G. Weinreich, Phys. Rev. **117**, 1460 (1960).
[16]P. S. Bednyakov, B. I. Sturman, T. Sluka, A. K. Tagantsev, and P. V. Yudin, Npj Comput. Mater. **4**, 65 (2018).
[17]C.-L. Jia, S.-B. Mi, K. Urban, I. Vrejoiu, M. Alexe, and D. Hesse, Nat. Mater. **7**, 57 (2008).
[18]W.-Y. Wang, Y.-L. Tang, Y.-L. Zhu, Y.-B. Xu, Y. Liu, Y.-J. Wang, S. Jagadeesh, and X.-L. Ma, Adv. Mater. Interfaces **2**, 1500024 (2015).
[19]A. Lubk, S. Gemming, and N. A. Spaldin, Phys. Rev. B **80**, 104110 (2009).
[20]Y. Wang, C. Nelson, A. Melville, B. Winchester, S. Shang, Z.-K. Liu, D. G. Schlom, X. Pan, and L.-Q. Chen, Phys. Rev. Lett. **110**, 267601 (2013).
[21]O. Diéguez, P. Aguado-Puente, J. Junquera, and J. Íñiguez, Phys. Rev. B **87**, 024102 (2013).
[22]M. Campanini, E. Gradauskaite, M. Trassin, D. Yi, P. Yu, R. Ramesh, R. Erni, and M. D. Rossell, Nanoscale **12**, 9186 (2020).
[23]A. Y. Borisevich, O. S. Ovchinnikov, H. J. Chang, M. P. Oxley, P. Yu, J. Seidel, E. A. Eliseev, A. N. Morozovska, R. Ramesh, S. J. Pennycook, and S. V. Kalinin, ACS Nano **4**, 6071 (2010).
[24]W. Y. Wang, Y. L. Zhu, Y. L. Tang, Y. B. Xu, Y. Liu, S. Li, S. R. Zhang, Y. J. Wang, and X. L. Ma, Appl. Phys. Lett. **109**, 202904 (2016).
[25]W. R. Geng, X. H. Tian, Y. X. Jiang, Y. L. Zhu, Y. L. Tang, Y. J. Wang, M. J. Zou, Y. P. Feng, B. Wu, W. T. Hu, and X. L. Ma, Acta Mater. **186**, 68 (2020).
[26]S. Li, Y. L. Zhu, Y. L. Tang, Y. Liu, S. R. Zhang, Y. J. Wang, and X. L. Ma, Acta Mater. **131**, 123 (2017).
[27]J. Schwarzkopf, D. Braun, M. Schmidbauer, A. Duk, and R. Wördenweber, J. Appl. Phys. **115**, 204105 (2014).
[28]T. Rojac, H. Ursic, A. Bencan, B. Malic, and D. Damjanovic, Adv. Funct. Mater. **25**, 2099 (2015).
[29]J. M. LeBeau and S. Stemmer, Ultramicroscopy **108**, 1653 (2008).
[30]T. Rojac, A. Bencan, G. Drazic, N. Sakamoto, H. Ursic, B. Jancar, G. Tavcar, M. Makarovic, J. Walker, B. Malic, and D. Damjanovic, Nat. Mater. **16**, 322 (2017).
[31]A. Bencan, G. Drazic, H. Ursic, M. Makarovic, M. Komelj, and T. Rojac, Nat. Commun. **11**, 1762 (2020).
[32]A. Lubk, M. D. Rossell, J. Seidel, Y. H. Chu, R. Ramesh, M. J. Hÿtch, and E. Snoeck, Nano Lett. **13**, 1410 (2013).
[33]C. T. Nelson, B. Winchester, Y. Zhang, S.-J. Kim, A. Melville, C. Adamo, C. M. Folkman, S.-H. Baek, C.-B. Eom, D. G. Schlom, L.-Q. Chen, and X. Pan, Nano Lett. **11**, 828 (2011).
[34]A. K. Tagantsev, L. E. Cross, and J. Fousek, *Domains in Ferroic Crystals and Thin Films* (Springer Science + Business Media, New York, NY, 2010).
[35]S. Hillyard and J. Silcox, Ultramicroscopy **58**, 6 (1995).
[36]M. Tewes, F. F. Krause, K. Müller, P. Potapov, M. Schowalter, T. Mehrtens, and A. Rosenauer, J. Phys.: Conf. Ser. **471**, 012011 (2013).

Supplementary Material

Atomically resolved structure of step-like uncharged and charged domain walls in polycrystalline $BiFeO_3$

Oana Condurache[1,2], Goran Dražić[1,2,3], Naonori Sakamoto[4], Tadej Rojac[1,2], and Andreja Benčan[1,2]

[1]*Electronic Ceramics Department, Jozef Stefan Institute, 1000 Ljubljana, Slovenia*

[2]*Jozef Stefan International Postgraduate School, 1000 Ljubljana, Slovenia*

[3]*National Institute of Chemistry, Hajdrihova 19, 1000 Ljubljana, Slovenia*

[4]*Research Institute of Electronics, Shizuoka University, 3-5-1 Naka-ku, Hamamatsu, Japan*

Supplementary material 1 – Schematics of possible polarization configuration on either side of *DW1*, *DW2* and *DW3*

From the projected displacement maps obtained from the high-angle annular-dark-field scanning-transmission electron microscopy (HAADF-STEM) (presented in Fig. 1(d)-(f) in the main manuscript) we can propose a possible 3D configuration of the polarization vector on either side of *DW1*, *DW2* and *DW3*, and therefore, determine the possible type of *DW1*, *DW2* and *DW3* from the angle-label point of view.

In a rhombohedral $BiFeO_3$, the spontaneous polarization can be along one of the four diagonals in the perovskite structure (along the $[111]_{pc}$ direction) so three different types of domain walls (DWs) can form: 71°, 109° and 180°. A wall is of 71°- type if the polarization from one domain has only one reversed polar component compared with the adjacent domain; the wall is of 109° type if the polarization from one domain has two reversed polar components compared with the adjacent domain, and lastly if all 3 polar components are reversed, the wall is a 180°-type DW. In order to identify the type of the wall from the projected Fe-displacement maps, we take into consideration both the projected Fe-displacement configuration on either side of the wall and also the plane in which the DW is situated. In the case of the uncharged configurations (”head-to-tail" or ”tail-to-head”) we assume that the plane of the DW is the particular plane in which electrical neutrality and mechanical compatibility is retained (71° DW on $\{110\}_{pc}$, 109° DWs on $\{100\}_{pc}$ and 180° DWs on $\{110\}_{pc}$) [1] [2]. Further, we do not make any assumptions about the plane in which the charged DWs (”head-to-head" or ”tail-to-tail” configuration) are lying [1].

DW1 lies in the $\{100\}_{pc}$ and has an uncharged configuration (Fig. S1(a)), so we conclude it is a 109° uncharged DW (the possible 3D polarization configuration is shown schematically in Fig. S1(d)). Using the same reasoning, the uncharged segment of *DW3* is a 109° uncharged DW (Fig. S1(c)). Because the uncharged segment of *DW3* is of the 109° type, the polarization on one side of the wall has two reversed polar components compared to the other side of the wall (the possible 3D polarization configuration is shown schematically in Fig. S1(f)). The same configuration of the polarization vectors will be maintained on either side of the ”tail-to-tail” segment and consequently, the charged segment of *DW3* is a 109° charged DW on $\{100\}_{pc}$. In the case of *DW2,* which has a ”tail-to-tail” configuration (Fig. S1(b)), we cannot identify the type of the wall from projected displacement maps only. *DW2* can be either a 71° ”tail-to-tail” charged DW on $\{100\}_{pc}$, or a 109° ”tail-to-tail” charged DW on $\{100\}_{pc}$ (the possible 3D polarization configuration is shown schematically in Fig. S1(e)).

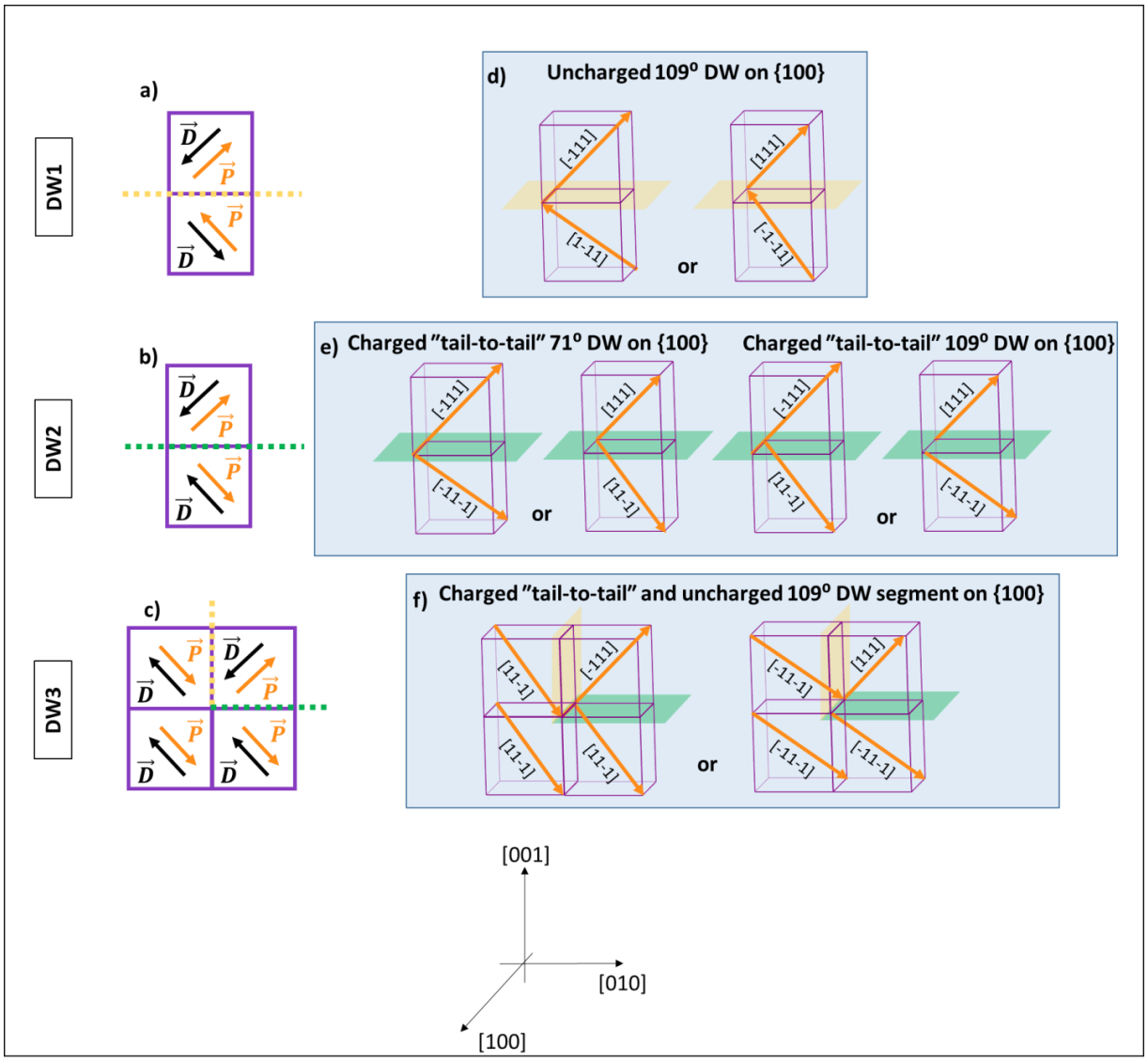

Figure S1. (a), (b), (c) Schematics of the projection of the Fe displacement ($\vec{D}$) and polarization ($\vec{P}$) vectors on either side of the wall for *DW1, DW2* and *DW3,* respectively. The schematics are a simplified representation of the projected displacement maps obtained from HAADF-STEM (shown in the main manuscript in Fig. 1 (d)-(f)). The projection is along one of the main crystalografic pseudocubic axis (e.g., [-100]). The uncharged DW planes are marked with a yellow dashed line, while the plane in which the charged DWs are lying are marked with a green dashed line.

d), e), f) Possible 3D configurations of the polarization vector on either side of the wall for *DW1, DW2* and *DW3,* respectively. The uncharged and charged DW planes are marked with yellow and green, respectively. The direction of the polarization vector is marked with the orange arrow.

All the notations follow the pseudocubic representation.

Supplementary material 2 – Unit-cell distortion of the Bi-sublattice parallel to the *DW1* and *DW2* plane

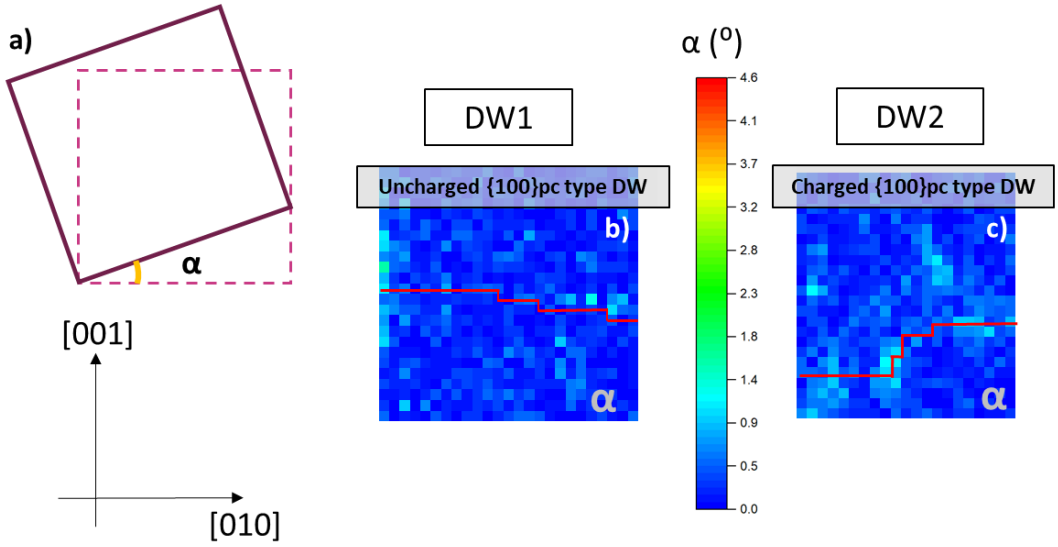

Figure S2. (a) Schematic representation of the unit-cell distortion angle parallel to [010] (α).

(b), (c) Unit-cell distortion of the Bi sublattice (α) parallel to the wall plane for the *DW1* and *DW2* regions, respectively. Red line marks the middle of the domain-wall region.

Supplementary material 3 – Simulated projected unit-cell distortion for uncharged, charged "tail-to-tail" and charged "head-to-head" $\{100\}_{pc}$ type DWs.

The projected unit-cell distortion was estimated from a simulated HAADF-STEM image containing segments of uncharged, charged-"tail-to-tail" and charged-"head-to-head" 109^o DWs (Fig. S3(a)). The image was simulated using the QSTEM code with a multi-slice method and frozen phonon approximation[3]. Thermal diffuse scattering was included in the simulations, so seven repetitions of the calculations per one image were used where the atomic positions were varied in the interval set by the estimated Debye-Waller factors for each calculation. We created an *R*3*c* $BiFeO_3$ structural model (ICSD 97591). A DW was created by a 180^o rotation of a part of the model (domain 2) around the [010] direction. The rhombohedral distortion was considered to be along $[\bar{1}11]$ in Domain 1 and $\bar{[}111]$ in Domain 2. The wall region was considered to be one unit-cell wide and the strain was evaluated by considering the Bi sublattice. Coordinates of the atomic columns were determined using a 2D Gaussian fit.

As seen from Fig. S3 (b) and (c), simulations show that the lattice distortion perpendicular to the DW plane is significantly higher for the uncharged DW (around 8°) than for the charged DW (for which the distortion is close to 0^o). Note in Fig. S3(d), (e) and (f) that a significant lattice shear is only observed at the uncharged DW (Fig. S3(d)).

The simulation data supports our experimental findings that the uncharged $\{100\}_{pc}$ DWs are intrinsically more strained than their charged counterparts (see Fig. 2 in the main manuscript and the associated discussion). There are, however, differences in the values obtained experimentally for the unit-cell distortion compared to those from the present simulation. Specifically, in the case of the uncharged DWs we measured a distortion angle between 3 and 4.5^o (see Fig. 2(b) and (d) in the main manuscript, compared to 8^o for the the simulation in Fig. S3(b)), while in the case of the charged DWs we measured an angle between 0 and 2^o (Fig. 2(c) and (e) in the main manuscript) compared to 0^o obtained from the simulation (Fig. S3(c)). One of the likely reasons for the quantitative discrepancy is that in the current simplified simulation the DW region was considered to be only one unit-cell wide, while experimentally the transition region from one domain to the other is typically a few units cells. Nevertheless, the simulation indicates that an intrinsic lattice mismatch exists when uncharged $\{100\}_{pc}$ DWs are created, while this intrinsic strain is smaller in the case of a charged $\{100\}_{pc}$ DW. This difference should affect the total energy requirements for the creation of the DWs, which is composed of electrostatic and elastic components [4].

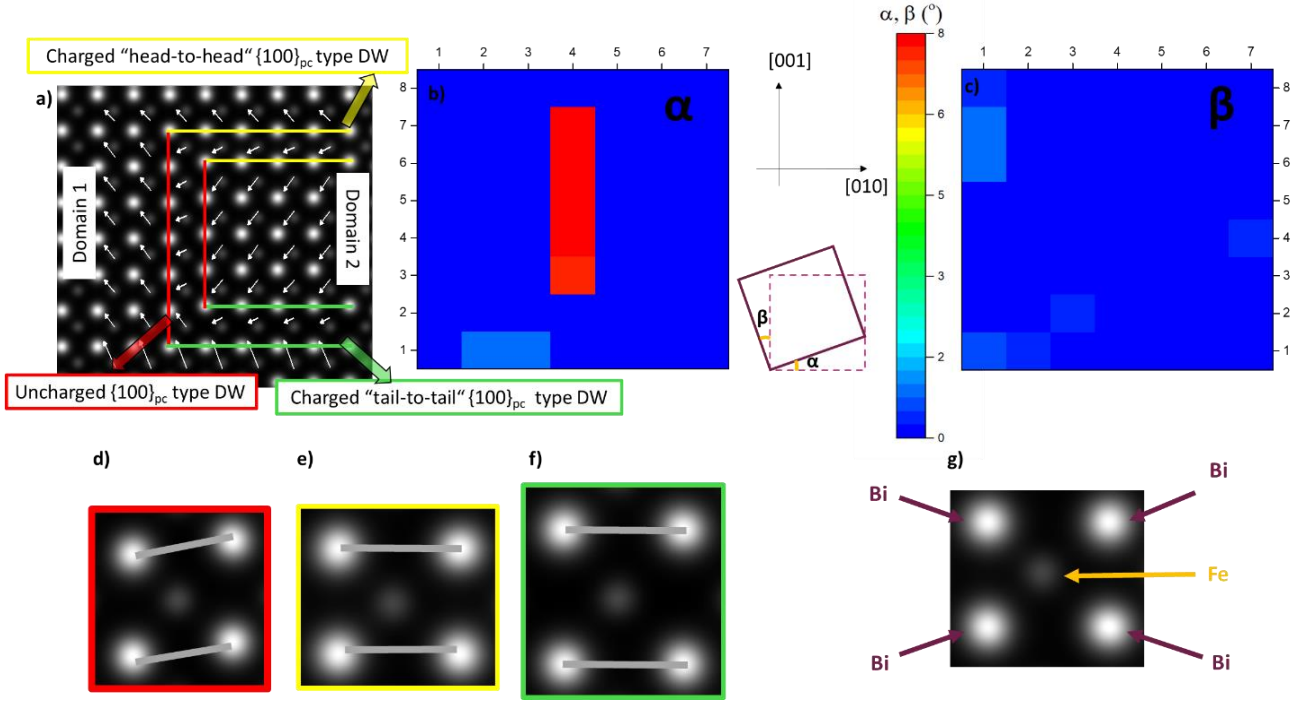

Figure S3. (a) Simulated HAADF-STEM image containing segments of uncharged (marked with red), charged-"tail-to-tail" (marked with green) and charged-"head-to-head" $\{100\}_{pc}$ DWs (marked with yellow). White arrows indicate Fe displacements from the center of the Bi sublattice (note that the Fe-displacement vector has an opposite orientation with respect to the polarization vector, hence the choice of the terminology "tail-to-tail" and "head-to-head" for the charged walls).

(b), (c) The unit-cell distortion angle mapped from the HAADF image in (a).

(d), (e), (f) Close-up of the individual projected unit-cell corresponding to the region of the uncharged (marked with red), charged-"tail-to-tail" (marked with green) and charged-"head-to-head" $\{100\}_{pc}$ DW (marked with yellow). The shear is more pronounced for the uncharged $\{100\}_{pc}$ DW and is marked with grey.

g) Schematic of a projected Bi-sublattice unit cell in the HAADF-STEM image.

Supplementary material 4 – Statistical analysis of the DW width performed across different locations of the charged and uncharged step-like DWs.

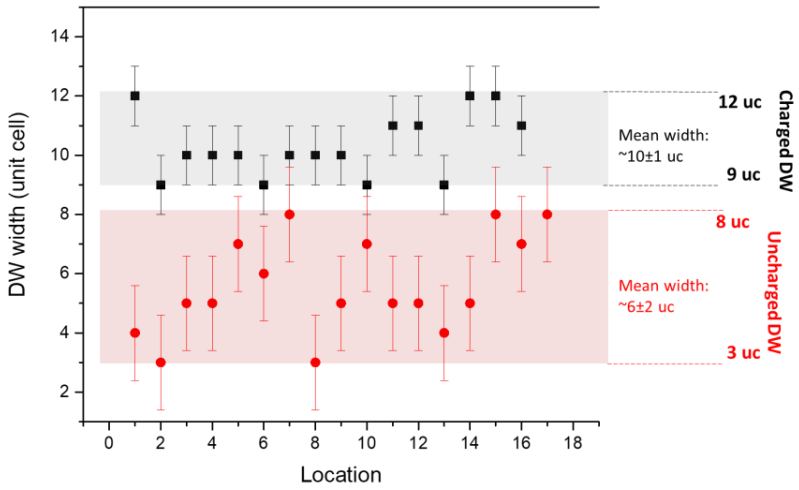

Figure S4. Scatter plot representing the DW width for several locations (numbered) of uncharged DWs (red dots) and charged DWs (black dots). The error bars mark the standard deviation, which is 2 uc for the uncharged DW width and 1 uc for the charged DW width. With the red and grey frames, we marked the interval between the minimum and maximum values obtained for uncharged and charged DW widths, respectively. The average DW width with standard deviation for the two cases is noted alongside respective plots. uc is an abbreviation for unit cell.

References

[1] W.-Y. Wang, Y.-L. Tang, Y.-L. Zhu, Y.-B. Xu, Y. Liu, Y.-J. Wang, S. Jagadeesh, and X.-L. Ma, Advanced Materials Interfaces **2**, 1500024 (2015).
[2] S.K. Streiffer, C.B. Parker, A.E. Romanov, M.J. Lefevre, L. Zhao, J.S. Speck, W. Pompe, C.M. Foster, and G.R. Bai, Journal of Applied Physics **83**, 2742 (1998).
[3] C. Koch, Determination of Core Structure Periodicity and Point Defect Density along Dislocations, PhD thesis, Arizona State University, 2002.
[4] A.K. Tagantsev, L.E. Cross, and J. Fousek, *Domains in Ferroic Crystals and Thin Films* (Springer New York, New York, NY, 2010).

Chapter 3

Atomic-Level Response of the Domain Walls in Bismuth Ferrite in a Subcoercive-Field Regime

The focus of the present study is to investigate the domain structure and its response to a subcoercive electric field in a $BiFeO_3$ (BFO) single crystal, down to the atomic level, using in-situ scanning transmission electron microscopy (STEM).

The domain structure of a BFO single crystal consists of zigzag DWs embedded in large lamellar domains. We applied an electric field in situ and monitor the response of the domain structure. The zigzag DWs show a higher mobility than the lamellar DWs, which are pinned on crystallographic defects. From Fe-displacement mapping (relative to the center of the Bi sublattice) the zigzag DWs have been assigned as 180° DWs, while the lamellar ones are assumed to be ferroelastic.

Further, the subcoercive field response of the zigzag mobile walls is analyzed. Since the expected phenomena in a low-field regime (i.e., subcoercive field) are short range, reaching the atomic resolution becomes imperative and the experiment is designed accordingly. The response of a single DW is observed at the atomic level. The mid-section of a zigzag wall moves (as determined based on atomic displacement); however, the strain field (seen in the annular bright field-STEM contrast) does not follow the movement of the wall. This can be explained by the segregation of defects with low mobility at the initial DW position, such as ordered clusters of oxygen vacancies. A different behavior is observed at the triangular apex of the zigzag wall, which is pinned, and it changes its morphology due to interaction with the electric field. The change in the DW plane comes together with bound-charge, strain and Bi-vacancies redistribution.

This chapter addresses thesis objectives 2, 3 and 4.

Published in: O. Condurache, G. Dražić, T. Rojac, H. Uršič, B. Dkhil, A. Bradeško, D. Damjanovic and A. Benčan "Atomic-Level Response of the Domain Walls in Bismuth Ferrite in a Subcoercive-Field Regime," *Nano Letters*, vol. 23, no. 2, pp. 750–756, 2023, https://pubs.acs.org/doi/10.1021/acs.nanolett.2c02857

My contribution: I performed and optimized the FIB specimen preparation. I contribute to the execution and optimization of the in-situ STEM biasing experiment. I analyzed the

data. I elaborated the concept of the manuscript and wrote the paper, together with the co-authors.

NANO LETTERS

pubs.acs.org/NanoLett Letter

Atomic-Level Response of the Domain Walls in Bismuth Ferrite in a Subcoercive-Field Regime

Oana Condurache,* Goran Dražić, Tadej Rojac, Hana Uršič, Brahim Dkhil, Andraž Bradeško, Dragan Damjanovic, and Andreja Benčan*

Cite This: *Nano Lett.* 2023, 23, 750–756 Read Online

ACCESS | Metrics & More | Article Recommendations | Supporting Information

ABSTRACT: The atomic-level response of zigzag ferroelectric domain walls (DWs) was investigated with in situ bias scanning transmission electron microscopy (STEM) in a subcoercive-field regime. Atomic-level movement of a single DW was observed. Unexpectedly, the change in the position of the DW, determined from the atomic displacement, did not follow the position of the strain field when the electric field was applied. This can be explained as low mobility defect segregation at the initial DW position, such as ordered clusters of oxygen vacancies. Further, the triangular apex of the zigzag wall is pinned, but it changes its shape and becomes asymmetric under electrical stimuli. This phenomenon is accompanied by strain and bound charge redistribution. We report on unique atomic-scale phenomena at the DW level and show that in situ STEM studies with atomic resolution are very relevant as they complement, and sometimes challenge, the knowledge gained from lower resolution studies.

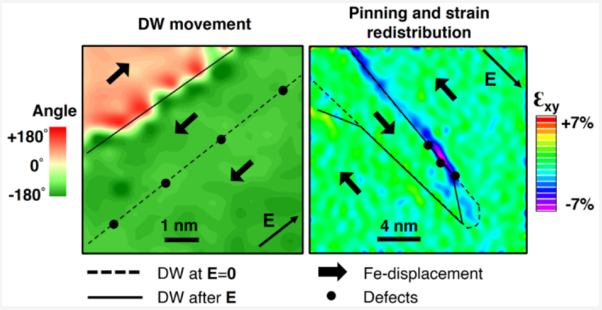

KEYWORDS: *Domain Walls, in situ STEM, Ferroelectric Switching, Bismuth Ferrite*

Ferroelectrics, which are characterized by a spontaneous and switchable electric polarization, are currently receiving a great deal of attention from both fundamental and technological points of view as they can be used for memory and logic devices, sensors and actuators, energy harvesters, and photoacoustic modulators, to name just a few examples. When an external electric field is applied to a ferroelectric material, the polarization within the domains tries to align with the direction of the field. As a result, changes occur in the domain structure, causing the domain walls (DWs), which are the boundaries between two adjacent domains with a homogeneous polarization, to move or change their properties. Nanoelectronics aims to exploit the dynamics of DWs, most frequently through their long-range movement during ferroelectric switching.[1]

A new perspective has recently been added to the area of DW nanoelectronics, i.e., the manipulation of the properties of stationary DWs under the influence of a subcoercive electric field.[2] For instance, in the case of $LiNbO_3$, in situ piezoelectric force microscopy has shown how the inclination plane of the DWs and their conductance can be tuned in a relatively weak field regime.[3,4] The interaction between the DWs and the subcoercive fields was rarely studied,[5−11] with more data having been collected for high-field ranges.

In situ techniques are essential for a direct observation of the response of DWs to electrical stimuli. In particular, in situ scanning transmission electron microscopy (STEM) provides a high spatial resolution and brings the experiment to the local scale of the DW (i.e., the atomic scale). There are very few in situ STEM studies with atomic resolution targeting ferroelectric DWs[12,13] compared to in situ STEM studies at the micrometer and nanometer level.[14−17] The lack of high-resolution in situ studies involving DWs is partly due to the tedious specimen-preparation process and need for special sample holders to apply an electric field. To achieve atomic resolution using the STEM technique, the specimen should be thin enough (ideally below 100 nm) while maintaining the integrity of the electrical device. The need for atomic-resolution studies becomes paramount in the low-field regime because the associated phenomena are expected to be short-range, on the scale of tens of picometers.

In the present study, a bismuth ferrite (BFO) single crystal grown by the flux method (details are given in Supplementary 1, in Supporting Information) used in a capacitor-like configuration was investigated by in situ STEM (Cs-corrected Jeol ARM 200 CF STEM operated at 200 kV combined with a Protochips Aduro system). The goal was to monitor with

Received: July 20, 2022
Revised: November 18, 2022
Published: December 2, 2022

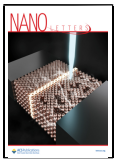

https://doi.org/10.1021/acs.nanolett.2c02857
Nano Lett. 2023, 23, 750−756

atomic resolution the DW interaction with a static subcoercive electric field, in a miniaturized capacitor-like device. The hypothesis is that, even in weak (subcoercive) fields, various nano- to atomic-scale phenomena can occur at the wall level, including changes to the wall morphology and in the unit-cell distortion.

We employed a focused ion beam (FIB) (Helios Nanolab 650 with Ga ions source) to prepare the specimen on electrical biasing optimized chips.[18] The specimen was prepared as with the classic lift-out lamella method and fixed between two electrodes by Pt deposition (more details in Supplementary 2, in Supporting Information). We assume that the external electric field in the analyzed area is relatively homogeneous as we determined from finite element (FE) simulations (Supplementary 2, in Supporting Information).

Bright-field (BF) and high-angle annular dark-field (HAADF) images were acquired simultaneously and represent the same area, at the same scale. The specimen was oriented along the $[100]_{pc}$ (for indexing, pseudocubic pc notation was used). As HAADF imaging provides almost pure atomic-number contrast and is, thus, more robust and less sensitive to mistilts than BF,[19] the atomic coordinates and displacements, visualized by Fe-displacement vector maps, are determined from HAADF images throughout the publication (more details in Supplementary 3, in Supporting Information). The Fe-displacement vector is qualitatively related to the projected polarization; the displacement is proportional to, but points in the opposite direction to, the polarization.[19]

As shown by BF-STEM (Figure 1a), the DW region appears as a region of lower intensity (darker contrast) due to the presence of strain fields. The domain structure of a BFO single crystal exhibits a high degree of order and consists of zigzag domains embedded in lamellar features. This domain structure appears to be characteristic of a BFO single crystal grown using the flux method.[20,21] Calculations[22] attribute their formation and stabilization to competition between long- and short-range electrostatic forces. The same domain configuration was reported in TEM specimens that were not confined to a capacitor-like geometry[20,21] and in bulk polished samples for piezoresponse force microscopy.[20]

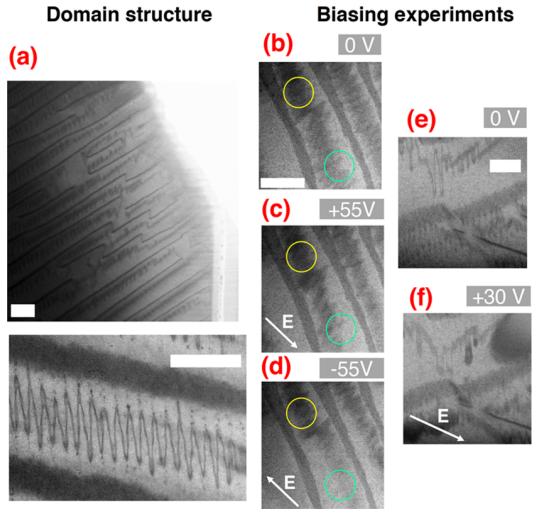

Figure 1. (a) BF images of the domain structure of the BFO single crystal; (b–d) BF images of the electric response of the domain structure at 0 V, +55 V, and −55 V, respectively. Marked with a green circle is a region that appears to respond to the electric field. Regions where the domain structure does not appear to respond to the electric bias are circled in yellow. (e, f) Another example of the evolution of the domain structure with the electric field. At +30 V, the DWs contrast smears off compared to 0 V. The scale bar marks 100 nm.

Jia et al.[21] performed a comprehensive atomic-resolution investigation of this type of DW in BFO single crystals, employing negative spherical aberration imaging TEM techniques. It was found that the zigzag DWs are ferroelectric 180° walls, while the lamellar ones are ferroelectric–ferroelastic walls. We confirmed the same type of zigzag walls by using HAADF-STEM (more details in Supplementary 3.1 and 3.2, in Supporting Information).

We found that the lamellar domains contain crystallographic defects, most probably related to the crystal-growth process (in Supplementary 3.2, in Supporting Information, antiphase boundaries and dislocations are shown). Nevertheless, the presence of defects on the lamellar DWs was not noted previously.[21] Irregularities in the TEM atomic contrast have been reported; these were assumed to result from the habit plane of the wall being tilted with respect to the viewing direction. We believe that this does not preclude the presence of defects, which could be concealed if the plane of the wall was not edged-on in the direction of the electron beam.

We applied an electric bias while monitoring the domain contrast (Figure 1b–f). The zigzag DWs are the first to respond to the electric field. At a relatively low magnification, an apparent switching takes place at some sites (circled in green in Figure 1b–d), while other sites do not respond (circled in yellow in Figure 1b–d). DW propagation appears to be favorable to random domain nucleation. Frequently, we cannot switch the zigzag domains, but we observed smearing of the contrast when an electric field is applied (Figure 1e,f), suggesting that a change in the morphology and the structure of the DW takes place. Different regions of the specimen respond differently depending on their own local electric field and strain distribution.[23] It was previously established that the ferroelectric switching processes are inhomogeneous on local scales.[24−27]

The lamellar features remain fixed in position when the voltage bias is applied, and we associate this with strong pinning on the crystallographic defects.

From the response of the specimen's domain structure, we conclude that we are working in a so-called low-field regime, i.e., in electric fields below the overall coercive field, where the coercive field is defined as the threshold field to change the orientation of the polarization permanently.[28] For BFO it is rarely reported in a single crystal but appears to be around a few tens of kV/cm.[29,30] Comparable values are reported for BFO ceramics,[31] while more significant values are reported for epitaxial thin films (100–200 kV/cm).[32] In any case, BFO is a material with a relatively high coercivity for a ferroelectric. For instance, its coercive field is at least 10 times higher than in the prototypical ferroelectric $BaTiO_3$.[14] Moreover, our specimens are thin (less than 100 nm), and it has been reported that the energy to switch the polarization in thin samples increases with decreasing thickness under the same conditions.[13] Therefore, thin BFO samples lend themselves perfectly to studying the evolution of the DW in subswitching electric field conditions.

We observed the local interactions between the mobile zigzag DWs and the electric field at the atomic level.

https://doi.org/10.1021/acs.nanolett.2c02857
Nano Lett. 2023, 23, 750−756

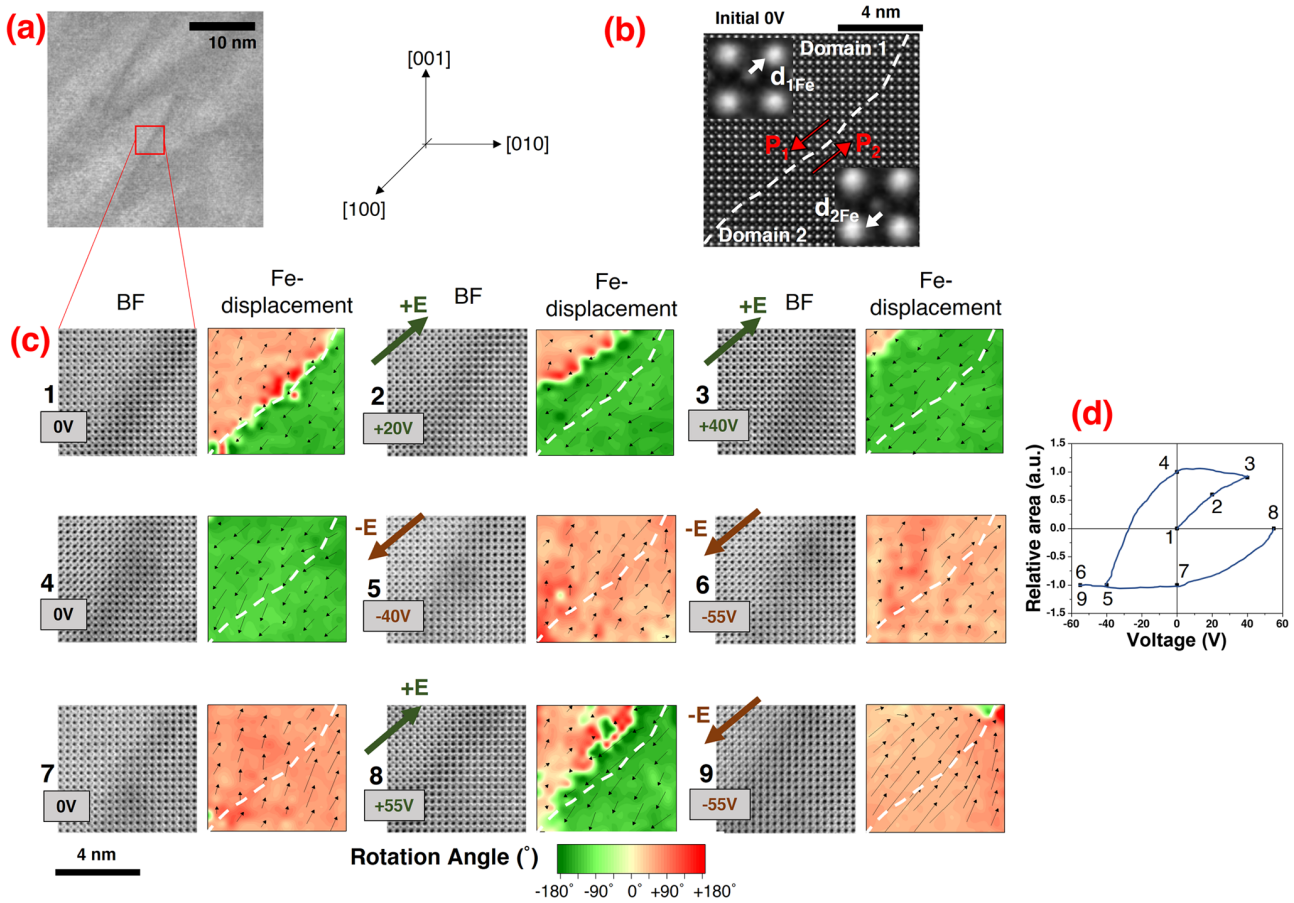

Figure 2. (a) BF image of a zigzag edge-on wall. The site that was further analyzed with atomic resolution is marked with a red rectangle. (b) HAADF image of the DW at the initial 0 V state. The Fe-displacement vector ($\mathbf{d}_{1Fe}$ and $\mathbf{d}_{2Fe}$) and polarization vector ($\mathbf{P}_1$ and $\mathbf{P}_2$) directions are indicated for each side of the wall. The DW is marked with a white dotted line. The inset is a close-up of one unit cell where the Bi and Fe atomic columns are seen. (c) Atomic-resolution BF-images at the wall location in the $[100]_{pc}$ zone axis together with an Fe-displacement vectors for a few unit cells (black arrows) superimposed on the colored map of the Fe-displacement rotation angle for the sequence 0 V, +20 V, +40 V, 0 V, −40 V, −55 V, 0 V + 55 V and −55 V. The sequence of applied voltages is numbered. The Fe-displacement information was extracted from the HAADF images (see Supplementary 4, in Supporting Information). The arrow lengths indicate the relative magnitude of the Fe-site displacement. The direction of the electric field (**E**) is indicated. A white dotted line marks the location of the enhanced BF contrast. (d) Plot of the relative area difference between Domain 2 and Domain 1 as a function of the applied voltage.

During an in situ experiment, we first concentrated on the central region of a segment of the zigzag edge-on DWs (Figure 2a) that is nominally uncharged (Figure 2b).

The contrast at the original position of the DW in the BF images during biasing (Figure 2c) is slightly altered; however, it does not vanish. Therefore, we took the area with enhanced dark contrast as a reference and kept it in the middle of the analyzed area.

We obtained an apparent switching in the analyzed area when a voltage bias is applied, as the Fe-displacement maps (Figure 2c) show. The projected Fe-displacement follows the direction of the field, i.e., from 0 V to +40 V, the DW seems to move toward the left, and Domain 2 grows. Going with the negative polarity, the polarization switches again, and no apparent DW is present in the analyzed area (Figure 2c, second line: 0 V, −40 V, and −55 V). When the field is applied directly from 0 V to +55 V, we can bring the DW back in the viewing area. The plot of the area difference between Domain 2 and Domain 1, relative to the total analyzed area, as a function of the voltage is shown in Figure 2d. The plot resembles a macroscopic polarization vs field hysteresis loop and is slightly asymmetric with respect to the voltage axis, an asymmetry that is characteristic for local measurements.[27,33] As far as we know, this is a rare case where a one-domain-wall hysteresis is derived from the displacement of individual atomic columns.

It is clear that by applying a voltage bias we can move the initial ferroelectric DW by a few nanometers relative to the position of the enhanced BF contrast. This result is intriguing because BF contrast is often considered the landmark of domain structure when describing its evolution with the electrical stimuli in low-magnification STEM in situ experiments.

Here we show that BF-enhanced contrast and the DW do not coincide, and they respond independently when a voltage bias is applied. We propose a scenario to explain this matter which assumes that point-charged defects are accountable for the strain contrast (BF contrast), marking the presence of the DW at 0 V. When a bias voltage is applied, the DW moves, but the defects do not follow the wall movement. Considering that the strain field contrast is smearing, we can hypothesize that the defects migrate and redistribute for a few unit cells. Therefore, the defects that are present must have low diffusivity. A similar scenario was proposed by Stolichnov et

https://doi.org/10.1021/acs.nanolett.2c02857
Nano Lett. 2023, 23, 750−756

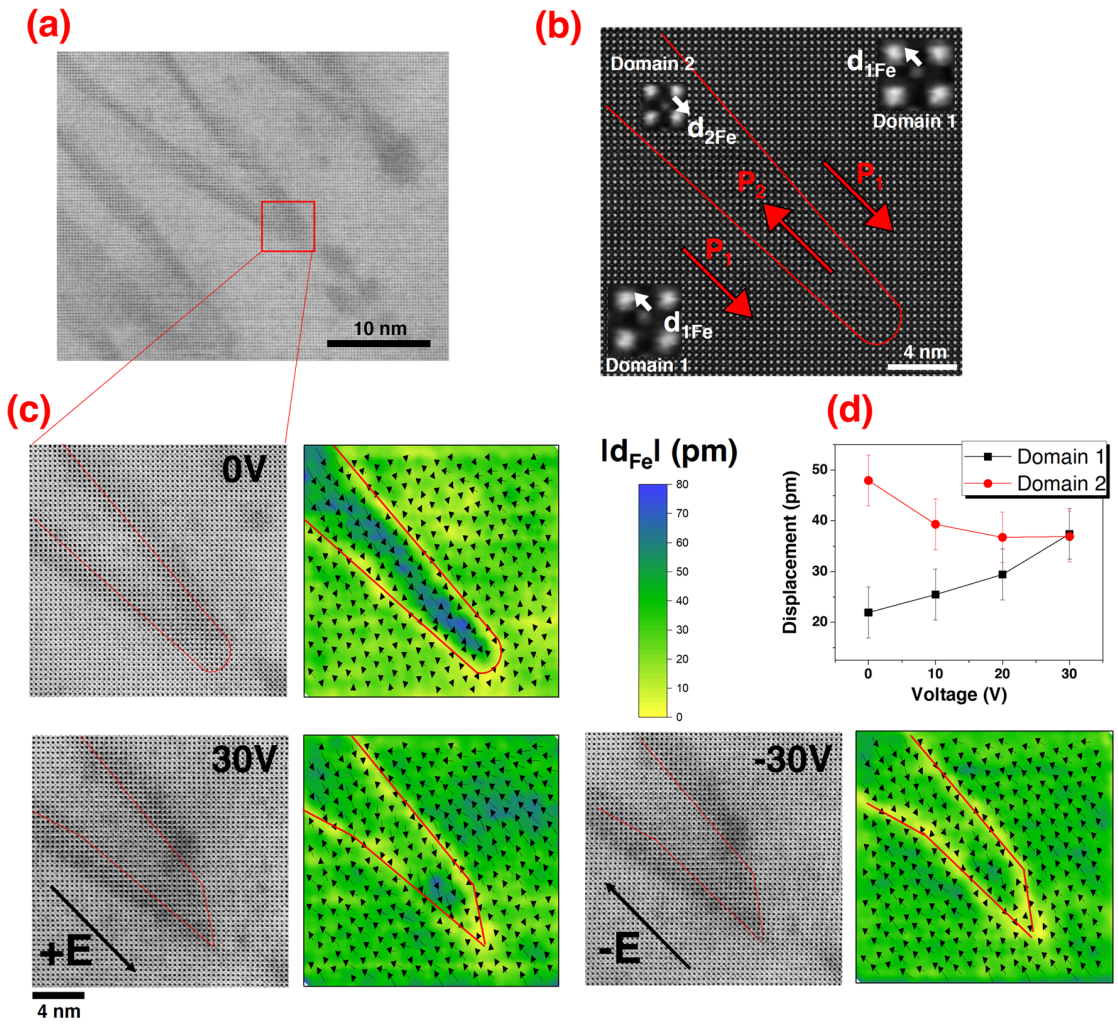

Figure 3. (a) BF image of a zigzag edged-on wall. The site that was further analyzed with atomic resolution is marked with a red rectangle. (b) HAADF image of the DW at the initial 0 V state. The Fe-displacement vector ($\mathbf{d}_{1Fe}$ and $\mathbf{d}_{2Fe}$) and polarization vector ($\mathbf{P}_1$ and $\mathbf{P}_2$) directions are indicated for each side of the wall. The inset is a close-up of one unit cell where the Bi and Fe atomic columns are visible. (c) Atomic-resolution BF images at the wall location together with Fe-displacement vectors for a few unit cells (black arrows) overlaid on a colored map of the Fe-displacement magnitude for the 0 V, + 30 V, and −30 V sequence. The Fe-displacement information was extracted from HAADF images (see Supplementary 4, in Supporting Information). The arrow lengths indicate the relative magnitude of the Fe-site displacement. The direction of the electric field (**E**) is indicated. The approximative position of the DW is marked with a red line. (d) Fe-displacement vector magnitude as a function of the external applied voltage.

al.[34] Among the possible point-charge defects in BFO systems, Bi-vacancies have been reported together with Fe^{4+}, the latest being linked with enhanced electrical conductivity at the wall.[31] In our crystals, electron-energy-loss spectroscopy (EELS) did not show the presence of Fe^{4+} (Supplementary 6.3, in Supporting Information), and this was also supported by conductive atomic force microscopy, which showed no enhanced DW conduction in the pristine BFO single crystal (Supplementary 6.4, in Supporting Information). Despite no observable drop of the integrated Bi atomic columns' intensity at the DW position in the HAADF images (Supplementary 6.1, in Supporting Information), we cannot rule out the segregation of the Bi-vacancies at original the DWs, as a large number of Bi-vacancies (up to 30 at. %)[31] should be present for them to be detected. Our EELS analysis indicated that O-vacancies are present at the zigzag walls with a smaller intensity of the O K edge at the wall location compared to the domain matrix (Supplementary 6.5, in Supporting Information). However, in the present study, the unequivocal detection or quantification of O-vacancies is beyond the capabilities of the method. While O-vacancies are generally considered highly mobile, their mobility can be reduced by ordering at high densities[34] or by forming defect complexes with Bi-vacancies.[35]

The second experiment tracked the interaction between the charged apex (i.e., the needle-domain's extremity) of the zigzag walls and the electric bias voltage at the atomic level (Figure 3a). The apex is strongly tail-to-tail negatively charged (as shown in Figure 3b,c). The intention was to have similar conditions as in the experiment describing the uncharged part of the walls. As the BF images show, the apex of the zigzag DWs changes its morphology under a voltage bias (Figure 3c), i.e., it becomes asymmetric. However, when equal and opposite voltages are applied, the apex plane's change could not be reversed (the BF image at +30 V is similar to the one at −30 V). The rest of the BF-STEM images for other intermediate voltages are shown in Supplementary 7.1, in Supporting

https://doi.org/10.1021/acs.nanolett.2c02857
Nano Lett. 2023, 23, 750−756

Information. Looking at the Fe-displacement maps in Figure 3c leads to the same conclusions. The plane of the apex becomes asymmetric, and the change is not reversible when the opposite voltage is applied (the rest of the Fe-displacement maps for other intermediate voltages are shown in Supplementary 7). Interestingly, the same asymmetry induced by an electric field in the plane of the tip was reported for needle-like 90° DWs in tetragonal $BaTiO_3$[36] that form at the intersection of three sets of domains.

Please note that, for the initial 0 V situation, the magnitude of the projected Fe-displacement is not equal in the two neighboring domains (Figure 3c); a similar structural asymmetry was observed for 90° DWs and is specific to most ferroelectric interfaces.[37] A noticeable change in the magnitude and orientation of the projected Fe-displacement on either side of the wall occurs when a voltage bias is applied (Figure 3c). The plot in Figure 3d shows how the average (the center of mass) of the Fe-displacement magnitude in the analyzed area changes with the voltage in one domain and the other. The magnitude of $\mathbf{d}_{1Fe}$ in Domain 1 grows (projected polarization $\mathbf{P}_1$ in the same direction as the electric field), while the magnitude of $\mathbf{d}_{2Fe}$ in Domain 2 is reduced (projected polarization $\mathbf{P}_2$ pointing in the opposite direction than the electric field). The changes in the atomic displacements due to electrical stimuli are almost never discussed in the literature. We show here that, for the weak-field regime in which the experiment takes place, the Fe-displacement, and hence the in-plane polarization, is altered. The Fe displaced about 1.8 times further from the body center at 30 V compared to the initial 0 V configuration in Domain 1, whereas in Domain 2 the Fe-displacement was reduced 1.3-fold. This information might be overlooked in low-magnification in situ studies, where details about the unit-cell distortion are not accessible. A quantitative statement about the polarization change would be inaccurate because we do not have access to the position of the O sublattice. However, qualitatively, we might expect the polarization to follow the same trend as the Fe-displacement. Moreover, the O sublattice displacement is supposed to be higher than the Fe-displacement relative to the body center of the Bi lattice when the electric field is applied.[38] Therefore, the factors of increasing/decreasing the polarization are expected to be higher than those for the Fe-displacements.

Because of the interesting charge state of the zigzag DWs, a question arises about the defect compensation in the vicinity of the strongly charged tip.[39] As discussed above, we did not detect any Fe^{4+} in this work. Segregation of Bi-vacancies is suggested by the intensity drop of the atomic columns of Bi in the vicinity of the tip (Figure 4a) (the Bi intensity maps for all voltage ranges are shown in Supplementary 6.2, in Supporting Information). This analysis suggests a higher segregation of Bi-vacancies at the apex compared to the midsection of the zigzag walls, which could be a reason for the observed pinning. If we assume that the negatively charged tail-to-tail apex could attract defects with a net positive charge, we can expect the presence of O-vacancies forming complexes with Bi-vacancies.[35]

The electric field most likely influences the redistribution of the Bi intensities, concomitantly with a redistribution of the strain evaluated by the geometric phase analysis (Figure 4). At 30 V there is an apparent segregation of the Bi-vacancies where the abrupt change in the apex plane takes place (Figure 4a), which coincides with an increase in the local strain (Figure 4b). Moreover, we reveal in Supplementary 8, in Supporting

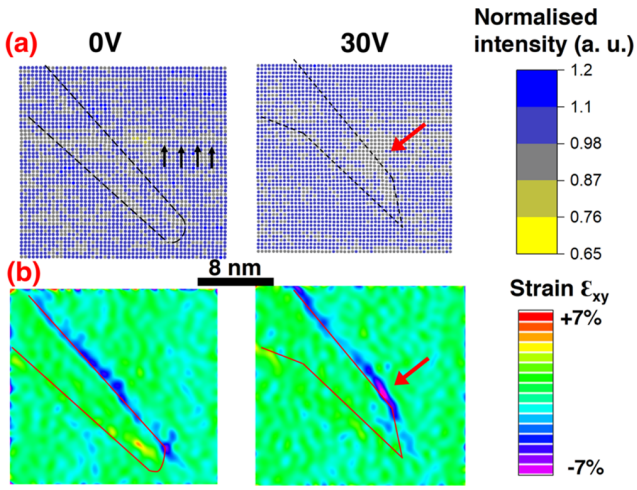

Figure 4. (a) Normalized Bi atomic columns' intensity maps for 0 and 30 V. The black line marks the position of the DW. Note that the intensity drop extended along the horizontal is likely due to a scanning artifact and it is marked with black arrows. (b) Strain maps calculated by Geometric Phase Analysis for 0 and 30 V. The DW region is marked with a red line. For 30 V in panels a and b, the red arrow marks the location where the intensity drop is substantial and the strain is enhanced.

Information, that under the influence of the electric field, the polarization bound charges redistribute in the vicinity of the walls as well (as a result of the change in the plane of the wall and the change in the Fe-displacement magnitude and orientation). Our simplified considerations show that at 30 V the bound charges increase on the segments (DWI, DWII) but decrease at the apex compared to the initial 0 V configuration.

Different charge states across the zigzag wall (uncharged midsection vs tail-to-tail charged apex) might set expectations of different dynamics when a voltage bias is applied. In the case of needle-like non-180° ferroelectric/ferroelastic DWs, it is assumed that the apex site will be activated first when the electric field is applied.[13,15,40] In the present experiment, however, the negatively charged apex seemed to be pinned, while a short-range switching took place for the uncharged central part of the zigzag walls. A higher concentration of defects (O-vacancies + Bi-vacancies) segregating at the apex could explain this experimental observation.

In summary, we applied a dedicated capacitor-like in situ STEM technique to observe the interaction between the weak subcoercive electric field and the zigzag 180° DWs in a BFO single crystal with atomic resolution. We monitored short-range movement with respect to the viewing plane for the neutral segment of the zigzag walls. The DW movement determined from the Fe-displacement map is decoupled from the strain field marked by an enhanced contrast in BF images. This can be explained as low mobility defect segregation at the initial DW position, such as ordered clusters of O-vacancies. In contrast, the zigzag wall's apex is pinned but atomic displacement response is observed when the electric field is applied. The pinning of the apex can be related to a higher segregation of Bi- and O-vacancies. Furthermore, we show that we can electrically bend the tip plane and induce different strain and bound charge-state configurations. The induced changes appear to be irreversible when an equal, but opposite, electric field is applied. The zigzag domain morphology is not unique to the BFO single crystal; hence, the current atomistic

https://doi.org/10.1021/acs.nanolett.2c02857
Nano Lett. 2023, 23, 750−756

implications revealed here might be applied to other ferroelectric systems, as well. To the best of our knowledge, this publication represents one of the first experimental works showing in situ the behavior of a ferroelectric material under a subswitching electric field near a DW at the atomic level.

■ ASSOCIATED CONTENT

Supporting Information

The Supporting Information is available free of charge at https://pubs.acs.org/doi/10.1021/acs.nanolett.2c02857.

Additional details including sample preparation and characterization approaches, calculations, images, and displacement maps (PDF)

■ AUTHOR INFORMATION

Corresponding Authors

Oana Condurache − *Electronic Ceramics Department, Jožef Stefan Institute, 1000 Ljubljana, Slovenia; Jožef Stefan International Postgraduate School, 1000 Ljubljana, Slovenia;* orcid.org/0000-0001-9398-2952; Email: oana.condurache@ijs.si

Andreja Benčan − *Electronic Ceramics Department, Jožef Stefan Institute, 1000 Ljubljana, Slovenia; Jožef Stefan International Postgraduate School, 1000 Ljubljana, Slovenia;* Email: andreja.bencan@ijs.si

Authors

Goran Dražić − *Electronic Ceramics Department, Jožef Stefan Institute, 1000 Ljubljana, Slovenia; Jožef Stefan International Postgraduate School, 1000 Ljubljana, Slovenia; National Institute of Chemistry, 1001 Ljubljana, Slovenia;* orcid.org/0000-0001-7809-8050

Tadej Rojac − *Electronic Ceramics Department, Jožef Stefan Institute, 1000 Ljubljana, Slovenia; Jožef Stefan International Postgraduate School, 1000 Ljubljana, Slovenia*

Hana Uršič − *Electronic Ceramics Department, Jožef Stefan Institute, 1000 Ljubljana, Slovenia; Jožef Stefan International Postgraduate School, 1000 Ljubljana, Slovenia;* orcid.org/0000-0003-4525-404X

Brahim Dkhil − *CentraleSupélec, Laboratoire Structures, Propriétés et Modélisation des Solides, Université Paris-Saclay, 91190 Gif-sur-Yvette, France;* orcid.org/0000-0002-9862-625X

Andraž Bradeško − *CentraleSupélec, Laboratoire Structures, Propriétés et Modélisation des Solides, Université Paris-Saclay, 91190 Gif-sur-Yvette, France*

Dragan Damjanovic − *Institute of Materials, Swiss Federal Institute of Technology−EPFL, 1015 Lausanne, Switzerland;* orcid.org/0000-0002-9596-7438

Complete contact information is available at: https://pubs.acs.org/10.1021/acs.nanolett.2c02857

Author Contributions

The manuscript was written through contributions of all authors. All authors have given approval to the final version of the manuscript. A. Benčan, G.D., and O.C. designed the experiments. B.D. prepared the single-crystal samples. O.C. prepared the samples for electron microscopy investigations by FIB. H.U. conducted the AFM analysis. A. Bradeško performed the finite-element simulations. O.C., A. Benčan, and G.D. performed the STEM investigations. O.C. wrote the manuscript. A. Benčan supervised the project. T.R. and D.D. contributed to the interpretation of the results. All the authors revised and edited the manuscript.

Notes

The authors declare no competing financial interest.

■ ACKNOWLEDGMENTS

This work is supported by Slovenian Research Agency in the frame of young-researcher program and core funding P2-0105 and projects J2-2497, J2-3041. Andraž Bradeško and Brahim Dkhil thank the European Union's Horizon 2020 research and innovation program under grant agreement no. 964931 through the project TSAR. The authors thank Val Fišinger and Jena Cilenšek for help with the AFM measurements.

■ ABBREVIATIONS

DW, domain wall; STEM, scanning transmission electron microscopy; BF, bight field; HAADF, high-angle annular dark field

■ REFERENCES

(1) Catalan, G.; Seidel, J.; Ramesh, R.; Scott, J. F. Domain Wall Nanoelectronics. *Rev. Mod. Phys.* **2012**, *84* (1), 119−156.

(2) Meier, D.; Selbach, S. M. Ferroelectric Domain Walls for Nanotechnology. *Nat. Rev. Mater.* **2022**, *7*, 157−173.

(3) Lu, H.; Tan, Y.; McConville, J. P. V.; Ahmadi, Z.; Wang, B.; Conroy, M.; Moore, K.; Bangert, U.; Shield, J. E.; Chen, L.; Gregg, J. M.; Gruverman, A. Electrical Tunability of Domain Wall Conductivity in $LiNbO_3$ Thin Films. *Adv. Mater.* **2019**, *31* (48), 1902890.

(4) Godau, C.; Kämpfe, T.; Thiessen, A.; Eng, L. M.; Haußmann, A. Enhancing the Domain Wall Conductivity in Lithium Niobate Single Crystals. *ACS Nano* **2017**, *11* (5), 4816−4824.

(5) Daniels, J. E.; Finlayson, T. R.; Davis, M.; Damjanovic, D.; Studer, A. J.; Hoffman, M.; Jones, J. L. Neutron Diffraction Study of the Polarization Reversal Mechanism in [111]c-Oriented $Pb(Zn_{1/3}Nb_{2/3})O_3 - xPbTiO_3$. *J. Appl. Phys.* **2007**, *101* (10), 104108.

(6) Pramanick, A.; Damjanovic, D.; Nino, J. C.; Jones, J. L. Subcoercive Cyclic Electrical Loading of Lead Zirconate Titanate Ceramics I: Nonlinearities and Losses in the Converse Piezoelectric Effect. *J. Am. Ceram. Soc.* **2009**, *92* (10), 2291−2299.

(7) Pantel, D.; Chu, Y.-H.; Martin, L. W.; Ramesh, R.; Hesse, D.; Alexe, M. Switching Kinetics in Epitaxial $BiFeO_3$ Thin Films. *J. Appl. Phys.* **2010**, *107* (8), 084111.

(8) Winkler, C. R.; Damodaran, A. R.; Karthik, J.; Martin, L. W.; Taheri, M. L. Direct Observation of Ferroelectric Domain Switching in Varying Electric Field Regimes Using *in situ* TEM. *Micron* **2012**, *43* (11), 1121−1126.

(9) Kundys, B.; Iurchuk, V.; Meny, C.; Majjad, H.; Doudin, B. Sub-Coercive and Multi-Level Ferroelastic Remnant States with Resistive Readout. *Appl. Phys. Lett.* **2014**, *104* (23), 232905.

(10) Pramanick, A.; Damjanovic, D.; Daniels, J. E.; Nino, J. C.; Jones, J. L. Origins of Electro-Mechanical Coupling in Polycrystalline Ferroelectrics During Subcoercive Electrical Loading: Origins of Electro-Mechanical Coupling in Polycrystalline Ferroelectrics. *J. Am. Ceram. Soc.* **2011**, *94* (2), 293−309.

(11) Kwamen, C.; Rössle, M.; Leitenberger, W.; Alexe, M.; Bargheer, M. Time-Resolved X-Ray Diffraction Study of the Structural Dynamics in an Epitaxial Ferroelectric Thin $Pb(Zr_{0.2}Ti_{0.8})O_3$ Film Induced by Sub-Coercive Fields. *Appl. Phys. Lett.* **2019**, *114* (16), 162907.

(12) Gao, P.; Britson, J.; Jokisaari, J. R.; Nelson, C. T.; Baek, S.-H.; Wang, Y.; Eom, C.-B.; Chen, L.-Q.; Pan, X. Atomic-Scale Mechanisms of Ferroelastic Domain-Wall-Mediated Ferroelectric Switching. *Nat. Commun.* **2013**, *4* (1), 2791.

(13) Chen, Z.; Li, F.; Huang, Q.; Liu, F.; Wang, F.; Ringer, S. P.; Luo, H.; Zhang, S.; Chen, L.-Q.; Liao, X. Giant Tuning of

https://doi.org/10.1021/acs.nanolett.2c02857
Nano Lett. 2023, 23, 750−756

Ferroelectricity in Single Crystals by Thickness Engineering. *Sci. Adv.* **2020**, *6* (42), No. eabc7156.
(14) Ignatans, R.; Damjanovic, D.; Tileli, V. Local Hard and Soft Pinning of 180° Domain Walls in $BaTiO_3$ Probed by *in situ* Transmission Electron Microscopy. *Phys. Rev. Mater.* **2020**, *4* (10), 104403.
(15) Gao, P.; Britson, J.; Nelson, C. T.; Jokisaari, J. R.; Duan, C.; Trassin, M.; Baek, S.-H.; Guo, H.; Li, L.; Wang, Y.; Chu, Y.-H.; Minor, A. M.; Eom, C.-B.; Ramesh, R.; Chen, L.-Q.; Pan, X. Ferroelastic Domain Switching Dynamics under Electrical and Mechanical Excitations. *Nat. Commun.* **2014**, *5* (1), 3801.
(16) Zhang, Y.; Han, M.-G.; Garlow, J. A.; Tan, Y.; Xue, F.; Chen, L.-Q.; Munroe, P.; Valanoor, N.; Zhu, Y. Deterministic Ferroelastic Domain Switching Using Ferroelectric Bilayers. *Nano Lett.* **2019**, *19* (8), 5319−5326.
(17) Li, L.; Jokisaari, J. R.; Pan, X. *In Situ* Electron Microscopy of Ferroelectric Domains. *MRS Bull.* **2015**, *40* (1), 53−61.
(18) Moering, J.. NEW FIB-OPTIMIZED E-CHIPS, 2018 https://www.protochips.com/news/fib-optimized-e-chips/ (accessed 2022-07-19).
(19) Nelson, C. T.; Winchester, B.; Zhang, Y.; Kim, S.-J.; Melville, A.; Adamo, C.; Folkman, C. M.; Baek, S.-H.; Eom, C.-B.; Schlom, D. G.; Chen, L.-Q.; Pan, X. Spontaneous Vortex Nanodomain Arrays at Ferroelectric Heterointerfaces. *Nano Lett.* **2011**, *11* (2), 828−834.
(20) Berger, A.; Hesse, D.; Hähnel, A.; Arredondo, M.; Alexe, M. Regular Nanodomain Vertex Arrays in $BiFeO_3$ Single Crystals. *Phys. Rev. B* **2012**, *85* (6), 064104.
(21) Jia, C.-L.; Jin, L.; Wang, D.; Mi, S.-B.; Alexe, M.; Hesse, D.; Reichlova, H.; Marti, X.; Bellaiche, L.; Urban, K. W. Nanodomains and Nanometer-Scale Disorder in Multiferroic Bismuth Ferrite Single Crystals. *Acta Mater.* **2015**, *82*, 356−368.
(22) Zhang, J.; Wang, Y.-J.; Liu, J.; Xu, J.; Wang, D.; Wang, L.; Ma, X.-L.; Jia, C.-L.; Bellaiche, L. Origin of Sawtooth Domain Walls in Ferroelectrics. *Phys. Rev. B* **2020**, *101* (6), 060103.
(23) Jesse, S.; Rodriguez, B. J.; Choudhury, S.; Baddorf, A. P.; Vrejoiu, I.; Hesse, D.; Alexe, M.; Eliseev, E. A.; Morozovska, A. N.; Zhang, J.; Chen, L.-Q.; Kalinin, S. V. Direct Imaging of the Spatial and Energy Distribution of Nucleation Centres in Ferroelectric Materials. *Nat. Mater.* **2008**, *7* (3), 209−215.
(24) Aravind, V. R.; Morozovska, A. N.; Bhattacharyya, S.; Lee, D.; Jesse, S.; Grinberg, I.; Li, Y. L.; Choudhury, S.; Wu, P.; Seal, K.; Rappe, A. M.; Svechnikov, S. V.; Eliseev, E. A.; Phillpot, S. R.; Chen, L. Q.; Gopalan, V.; Kalinin, S. V. Correlated Polarization Switching in the Proximity of a 180° Domain Wall. *Phys. Rev. B* **2010**, *82* (2), 024111.
(25) Nataf, G. F.; Salje, E. K. H. Avalanches in Ferroelectric, Ferroelastic and Coelastic Materials: Phase Transition, Domain Switching and Propagation. *Ferroelectrics* **2020**, *569* (1), 82−107.
(26) Tagantsev, A. K.; Stolichnov, I.; Setter, N.; Cross, J. S.; Tsukada, M. Non-Kolmogorov-Avrami Switching Kinetics in Ferroelectric Thin Films. *Phys. Rev. B* **2002**, *66* (21), 214109.
(27) Gao, P.; Nelson, C. T.; Jokisaari, J. R.; Baek, S.-H.; Bark, C. W.; Zhang, Y.; Wang, E.; Schlom, D. G.; Eom, C.-B.; Pan, X. Revealing the Role of Defects in Ferroelectric Switching with Atomic Resolution. *Nat. Commun.* **2011**, *2* (1), 591.
(28) Boddu, V.; Endres, F.; Steinmann, P. Molecular Dynamics Study of Ferroelectric Domain Nucleation and Domain Switching Dynamics. *Sci. Rep.* **2017**, *7* (1), 806.
(29) Teague, J. R.; Gerson, R.; James, W. J. Dielectric Hysteresis in Single Crystal $BiFeO_3$. *Solid State Commun.* **1970**, *8* (13), 1073−1074.
(30) Lebeugle, D.; Colson, D.; Forget, A.; Viret, M.; Bonville, P.; Marucco, J. F.; Fusil, S. Room-Temperature Coexistence of Large Electric Polarization and Magnetic Order in $BiFeO_3$ Single Crystals. *Phys. Rev. B* **2007**, *76* (2), 024116.
(31) Rojac, T.; Bencan, A.; Drazic, G.; Sakamoto, N.; Ursic, H.; Jancar, B.; Tavcar, G.; Makarovic, M.; Walker, J.; Malic, B.; Damjanovic, D. Domain-Wall Conduction in Ferroelectric $BiFeO_3$ Controlled by Accumulation of Charged Defects. *Nat. Mater.* **2017**, *16* (3), 322−327.
(32) Shelke, V.; Mazumdar, D.; Srinivasan, G.; Kumar, A.; Jesse, S.; Kalinin, S.; Baddorf, A.; Gupta, A. Reduced Coercive Field in $BiFeO_3$ Thin Films Through Domain Engineering. *Adv. Mater.* **2011**, *23* (5), 669−672.
(33) Jablonski, M. L.; Liu, S.; Winkler, C. R.; Damodaran, A. R.; Grinberg, I.; Martin, L. W.; Rappe, A. M.; Taheri, M. L. Asymmetric Response of Ferroelastic Domain-Wall Motion under Applied Bias. *ACS Appl. Mater. Interfaces* **2016**, *8* (5), 2935−2941.
(34) Stolichnov, I.; Iwanowska, M.; Colla, E.; Ziegler, B.; Gaponenko, I.; Paruch, P.; Huijben, M.; Rijnders, G.; Setter, N. Persistent Conductive Footprints of 109° Domain Walls in Bismuth Ferrite Films. *Appl. Phys. Lett.* **2014**, *104*, 132902.
(35) Geneste, G.; Paillard, C.; Dkhil, B. Polarons, vacancies, vacancy associations, and defect states in multiferroic $BiFeO_3$. *Phys. Rev. B* **2019**, *99*, 024104.
(36) Zhang, Z. H.; Qi, X. Y.; Duan, X. F. Two-Step Evolution Mechanism of Multi-Domains in $BaTiO_3$ Single Crystal Investigated by in Situ Transmission Electron Microscopy. *Scr. Mater.* **2008**, *58* (6), 441−444.
(37) Chandrasekaran, A.; Wei, X.-K.; Feigl, L.; Damjanovic, D.; Setter, N.; Marzari, N. Asymmetric Structure of 90° Domain Walls and Interactions with Defects in $PbTiO_3$. *Phys. Rev. B* **2016**, *93* (14), 144102.
(38) Lee, H. J.; Guo, E.-J.; Min, T.; Hwang, S. H.; Lee, S. Y.; Dörr, K.; Lee, J.; Jo, J. Y. In Situ Observation of Atomic Movement in a Ferroelectric Film under an External Electric Field and Stress. *Nano Res.* **2018**, *11* (7), 3824−3832.
(39) Sluka, T.; Tagantsev, A. K.; Damjanovic, D.; Gureev, M.; Setter, N. Enhanced Electromechanical Response of Ferroelectrics Due to Charged Domain Walls. *Nat. Commun.* **2012**, *3* (1), 748.
(40) Lu, G.; Li, S.; Ding, X.; Sun, J.; Salje, E. K. H. Electrically Driven Ferroelastic Domain Walls, Domain Wall Interactions, and Moving Needle Domains. *Phys. Rev. Materials* **2019**, *3* (11), 114405.

https://doi.org/10.1021/acs.nanolett.2c02857
Nano Lett. 2023, 23, 750−756

Atomic-level response of the Domain Walls in bismuth ferrite in a subcoercive-field regime

Oana Condurache[†,‡], Goran Dražić [†,‡,#], Tadej Rojac[†,‡], Hana Uršič[†,‡], Brahim Dkhil[§], Andraž Bradeško[§], Dragan Damjanovic[||] and Andreja Benčan [†,‡]

† Electronic Ceramics Department, Jožef Stefan Institute, 1000 Ljubljana, Slovenia; ‡ Jožef Stefan International Postgraduate School, 1000 Ljubljana, Slovenia; # National Institute of Chemistry, 1001 Ljubljana, Slovenia; §CentraleSupélec, Laboratoire Structures, Propriétés et Modélisation des Solides, Université Paris-Saclay, 91190 Gif-sur-Yvette, France; || Institute of Materials, Swiss Federal Institute of Technology–EPFL, 1015 Lausanne, Switzerland.

Key words: Domain Walls, in situ STEM, Ferroelectric Switching, Bismuth Ferrite

Supplementary 1- **Bismuth ferrite (BFO) single crystal preparation and structural characterization**

The single crystals were grown using flux method starting with high purity powders of Fe_2O_3 and Bi_2O_3 with the flux proportion of 0.15/0.85. The mixture was placed into a platinum crucible, and sealed to prevent the loss of bismuth oxide during the thermal treatment. Further, it was heated to 900°C for 4 h and the temperature was decreased slowly (0.5°C/h) till 790°C and then more rapidly

(~100°C/h) to room temperature. Finally, tiny crystals were extracted after washing with boiling dilute (20%) nitric acid.

The purity of the crystal has been confirmed by X-ray diffraction (Figure S1.1) and Raman Spectroscopy (Figure S1.2).

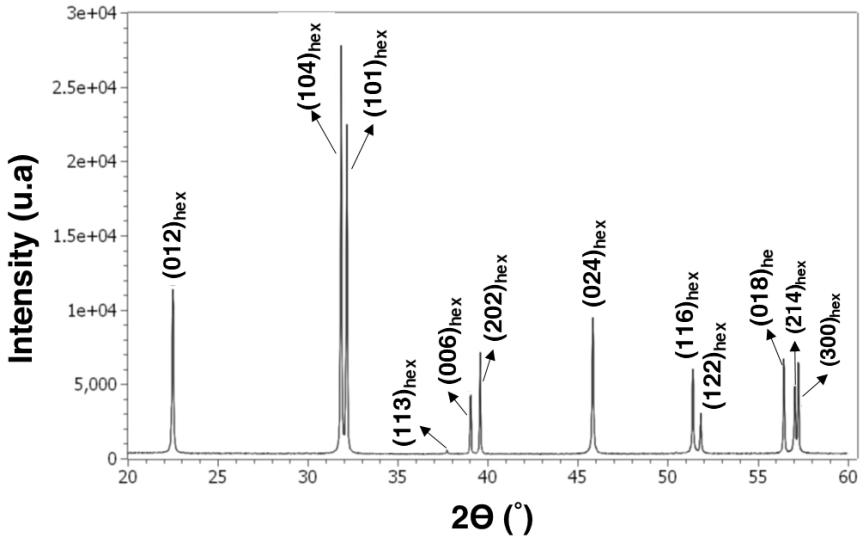

Figure S1.1 X-ray diffraction pattern of crushed crystals. The peaks were indexed according to rhombohedral symmetry with R3c space group. The reported indexation is done in the hexagonal setting. No other peaks other than the ones corresponding to bismuth ferrite (standard card JCPDS no. 86-1518) can be evidenced

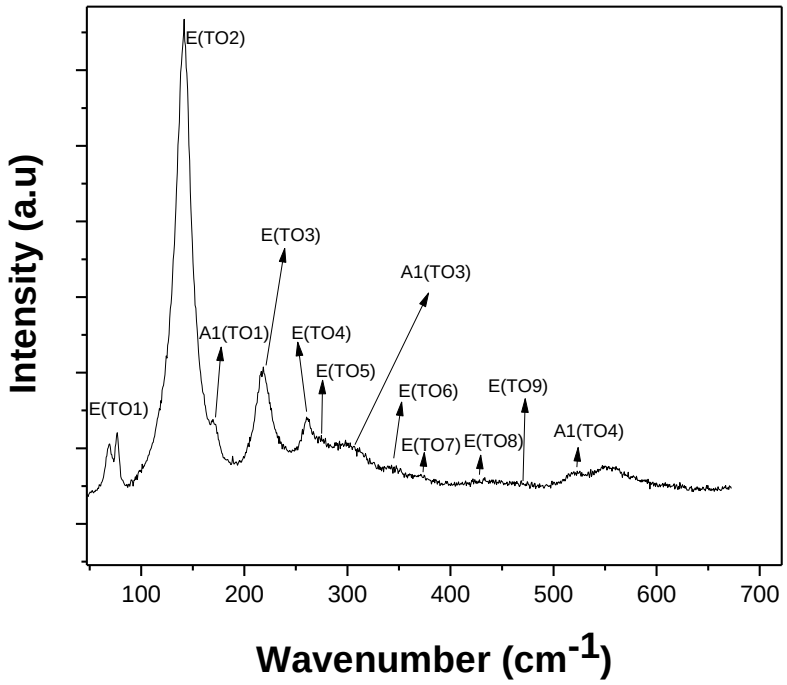

Figure S 1.2 Raman spectrum measured using T6400 Jobin-Yvon, Horiba spectrometer with a green 514nm laser source at room temperature. Only the phonon modes corresponding to bismuth ferrite have been identified. No trace of any parasitic phase can be detected.

Supplementary 2- **Specimen preparation and electrostatic finite element calculations of the electric field distribution in the device**

Specimen preparation

The specimen is prepared on optimized Protochips-Fusion electrical Si-based chips with patterned electrodes by focused ion beam[1] (FIB) (Helios Nanolab 650 with Ga ions source). This type of FIB support chip[1] offers the possibility to prepare sufficiently thin, high-quality specimens in order to achieve atomic resolution while simultaneously applying electric field in situ.

A capacitor-like configuration offers the advantage of a relatively homogeneous electric field [2,3], compared to other more frequently used configurations such as the probe techniques.

The first step of the specimen preparation was electron deposition of a thin layer of Pt (0.4 μm) which allow protection of the top surface of the sample before using the ion beam, which reduces ion implantation and improves sample quality. A next layer of Pt is further deposited with ions to create a thick protection layer for the FIB sample preparation process (2 μm). The sample is then milled using the ion beam to create a standing lamella which is then transferred with the aid of a manipulator on the biasing support chip.

The electrical contacts are made by ion beam assisted Pt-deposition (30 kV, ≈ 0.23 nA). The spacing between the electrodes is by default 20 μm.

A scanning electron microscopy (SEM) image of the specimen on the biasing chip is shown in Figure S2.1a. The specimen is thinned with ions until electron transparency is reached. To maintain mechanical stability, the specimen is not uniformly thinned. Some isolated windows with thickness less than 100nm are done (green color in Figure S2.1a), while the rest of the lamella is kept thicker

≈200 nm (blue color in Figure S2.1a). We always perform the in situ STEM analysis on areas where the domain structure is preserved and which are not thinner than 50 nm. In this way, the effects associated with the reduced thickness (reduction/annihilation of polarization, domain structure alteration) are avoided[4].

Thinning of the specimen was done at 30 kV in 3 steps by progressively lowering the ion beam current (typically 0.8nA, 0.2nA and 8 pA). In addition, low energy ion beam cleaning is performed in order to gradually remove surface amorphization or any other kind of contamination.

The ion beam characteristics that we used for FIB lamella preparation are listed in the table below.

Table S 2 – The ion/electron beam accelerating voltages and currents used during the FIB specimen preparation procedure

<table>
<tr><th>Procedure</th><th>Voltage</th><th>Current</th></tr>
<tr><td>E-beam Pt deposition</td><td>2 kV</td><td>1.6 nA</td></tr>
<tr><td>I-beam Pt deposition</td><td>30 kV</td><td>0.2 nA</td></tr>
<tr><td>Electrical contacts</td><td>30 kV</td><td>0.2 nA</td></tr>
<tr><td rowspan="3">Thinning of the specimen</td><td rowspan="3">30 kV</td><td>0.8nA</td></tr>
<tr><td>0.2nA</td></tr>
<tr><td>80 pA</td></tr>
<tr><td rowspan="4">Cleaning of the specimen</td><td>5 kV</td><td rowspan="4">40-100 pA</td></tr>
<tr><td>2 kV</td></tr>
<tr><td>1 kV</td></tr>
<tr><td>0.5 kV</td></tr>
</table>

Additional cuts are done on top to avoid short circuit through Pt layer when bias voltage is applied. In addition, a cut is made at the bottom of the specimen[2] to remove the material that was redeposited during ion milling and which may potentially be more conductive than the rest.

In order to check the amount of Ga contamination we performed energy dispersive X-ray analysis (EDXS) analysis. Quantitative EDXS/STEM mapping (Bi M, Fe K and Ga L lines shown in Figure S2.2 a)-d)) was done across a BFO lamella prepared by FIB with the same conditions as the samples for in situ studies (a STEM dark field (DF) image is shown in Figure R1 e)). The EDXS-mapping shows an inhomogeneous distribution of Ga throughout the lamella with the highest concentration on the top Pt-deposited layer, as expected. A line EDXS analysis on mid-section (red line marked in Figure S2.2 e)) shows that for the most part the concentration of Ga is around 1 wt% but increases very close to the edge because the specimen is mostly amorphous in this area. The in situ experiments presented in the manuscript are done in regions of the sample which are mostly crystalline. Therefore, we would expect that the Ga concentration was around 1 wt%; we expect that a much smaller amount is incorporated in the perovskite lattice, most of the contamination should be set in the very thin amorphous sidewall.

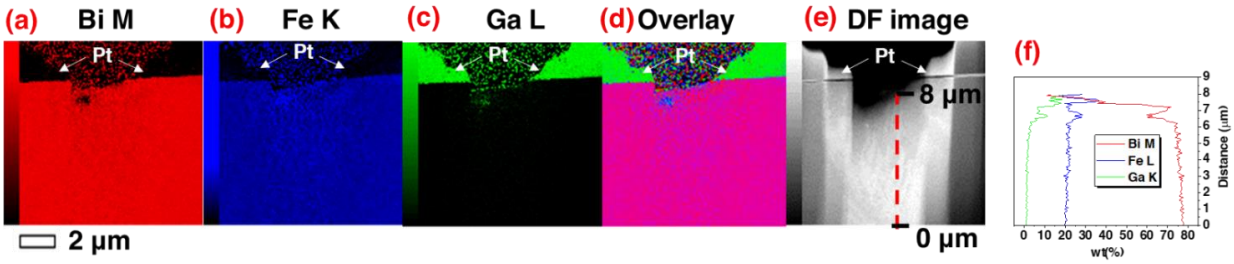

Figure S 2.1 EDXS quantitative elemental maps for (a) Bi M, (b) Fe K, (c) Ga L and their overlaid image (d) for the region of the specimen shown in the DF image in (e). The red dotted line marks the region where the EDXS line analysis show in (f) was taken

Electrostatic finite element model calculations

The electric field distribution was simulated using the finite element method (FEM) implemented in Comsol Multiphysics 5.2 with microelectromechanical systems module. The geometric model (Figure S2a-d) was built considering the three dimensions of the specimen.

The sections used to build the geometric model for FEM are marked with matching colors (Figure S2a, c-d):

- Section 1 (pink): parts which are in direct contact with the electrodes and are relatively thick: 1.2 µm.
- Section 2 (green): electron transparent windows with thickness between 70 and 150 nm.
- Section 3 (blue): electron transparent window of about 200 nm thickness.

Figure S2c-d shows the simplified built geometric model along with in-plane and cross section dimensions used for the electrostatic FEM. The (z,y) dimensions were measured from scanning

SEM) imaging (Figure S2c). The thickness profile (z,x) was determined by scanning transmission electron microscopy (STEM) - electron energy loss spectroscopy (EELS) thickness mapping (Figure S2b) for the very thin sections (2 and 2') and approximated from SEM imaging for the other sections (1, 1', 3) (Figure S2d).

Tetrahedral adaptive mesh was used for the FEM simulation (mesh element maximum 1.6 μm and minimum 0.2 μm). The potential difference between the electrodes was set to +55 V (maximum value applied in the experiment) and it was used as a boundary condition. The relative dielectric permittivity was considered $\varepsilon_{BFO} \approx 80$[5] for the bismuth ferrite and $\varepsilon_{Pt} \approx \infty$ for the Pt layer.

The results of the FEM simulations are shown in Figure S2e-f.

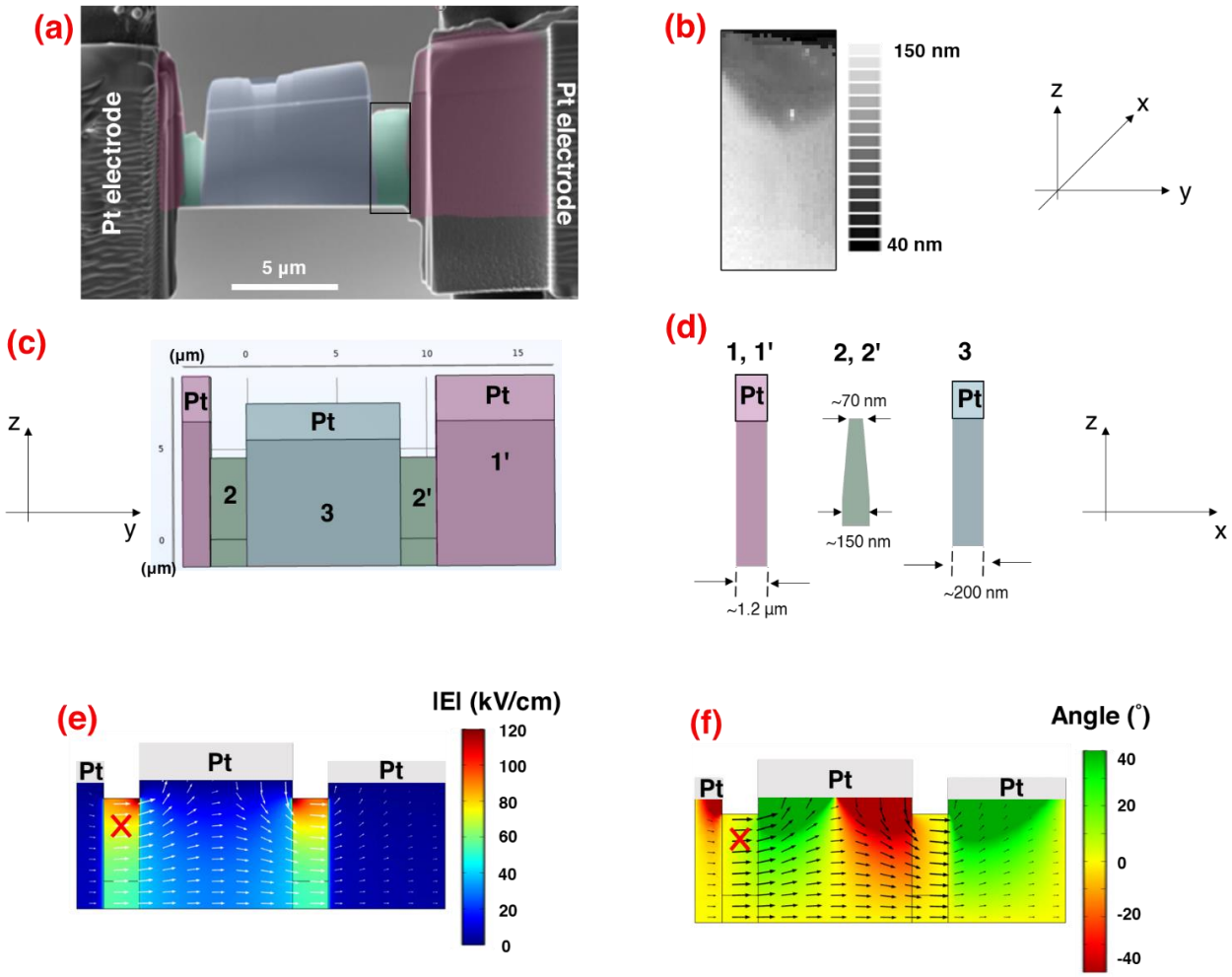

Figure S 2.2 (a) False colored SEM image of the specimen prepared in FIB. The sections of the specimen considered further in the FEM model are colored.

(b) EELS-thickness map of the region marked with black rectangle in (a).

(c) In-plane z-y geometric configuration of the model. (d) The cross-section z-x geometric configuration of the model.

Colored map of the distribution of the electric-field e) magnitude and f) orientation in the specimen as calculated by FEM. White and black arrows, respectively, mark the direction of the field on each location. The density of arrows is arbitrary. With red cross the approximate location of the experiment is indicated.

Supplementary 3- **Types of domain walls in BFO single crystal**

The BFO single crystal presents two types of domain walls morphology as described in the main manuscript: zigzag-like (Figure S3.1) and lamellar-like DWs (Figure S3.2).

From HAADF images acquired in $[100]_{pc}$ zone axis, the coordinates of the atomic columns were determined using a 2D Gaussian fit according to a previously reported methodology[5]. We can identify the position of Fe and Bi. However, the position of O, which accounts for the center of negative charge of the unit cell, is concealed. It has been experimentally demonstrated that the position of O is redundant because Fe-displacement in respect to the Bi sublattice ($\boldsymbol{d_{Fe}}$) gives enough qualitative information on the projected polarization direction: namely, the projected polarization is proportional but points in opposite direction to Fe-displacement vector[6].

In rhombohedral symmetry of BFO (space group *R*3*c*), the spontaneous polarization can lie along one of the four diagonals in the pseudocubic perovskite unit cell (along the $[111]_{pc}$ direction). If one, two or three components of the polarization vector are reversed in one domain compared to the adjacent domain, the DW will be: 71°, 109° or 180°, respectively[7].

In the case of uncharged configurations (head-to-tail or tail-to-head configuration), in order to minimize the electrostatic and elastic energy, the walls usually lie on (or close to) the neutral plane, namely 71º will lie on {110}pc, 109º on {100}pc and 180º on {110}pc[8-11]. No assumptions can be made about the crystallographic plane in which the charged DWs (head-to-head or tail-to-tail configuration) are lying.

We were able to assign the zigzag walls as being of 180˚- type: $\boldsymbol{d_{Fe}}$ is antiparallel in one side compared to the other of the wall and the DW lays approximately on neutral $\{110\}_{pc}$ plane[10] (Figure S3.1).

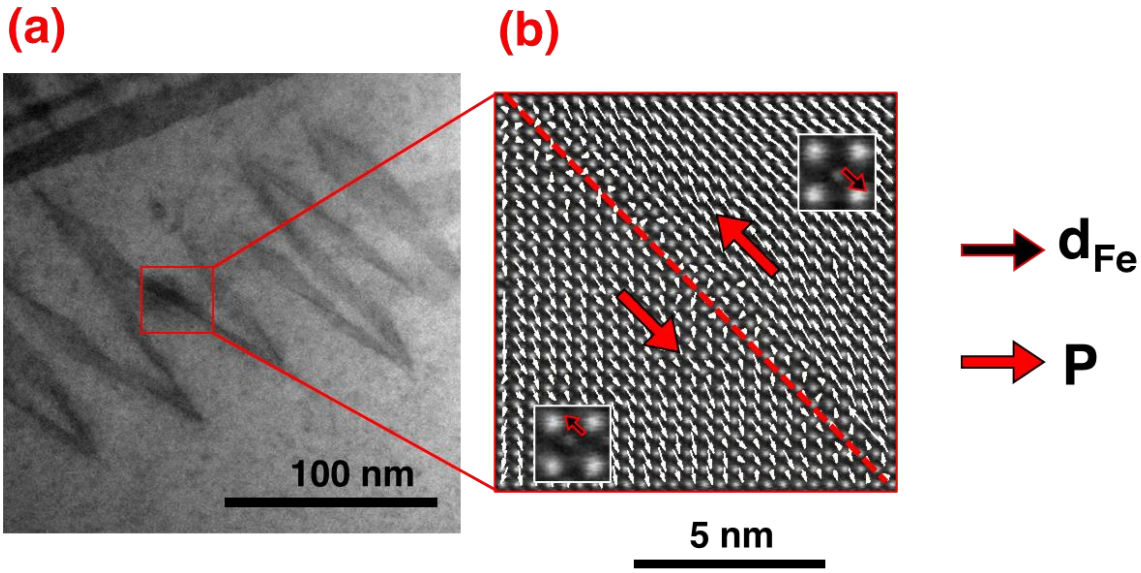

*Figure S3.1 (a) Bright field (BF) image of the zigzag domain structure. (b) HAADF atomic resolution image of a region on a zigzag wall with the corresponding Fe-displacement map overlaid. The position of the wall is marked with red dotted line. The insets on each side of the wall show an one-unit cell close-up and the approximate direction of the Fe-displacement (black arrow ($\boldsymbol{d_{Fe}}$)) in respect to the center of Bi lattice. The direction of the polarization is indicated with red arrow (**P**).*

The lamellar features appear to contain different crystallographic defects (Figure S3.2a). The crystallographic defects have been identified to be dislocations (Figure S3.2b), and antiphase boundaries (Figure S3.2c-d). Moreover, the lamellar features are nominally head-to-head charged DWs (see the direction of Fe-displacement and projected polarization, respectively in Figure S3.2

c)-d)). Because we have access only to the projected polarization in the imaging plane (we can determine only 2 components out of 3) and the DWs are charged so there are no restrictions on the plane they should lay[10,11], we cannot univocally determine the angle type of the lamellar DWs. They can be either 180˚ or 109˚ DWs. Previous studies[12] report this type of DWs to be ferroelastic so, the 109˚ DWs scenario is more plausible.

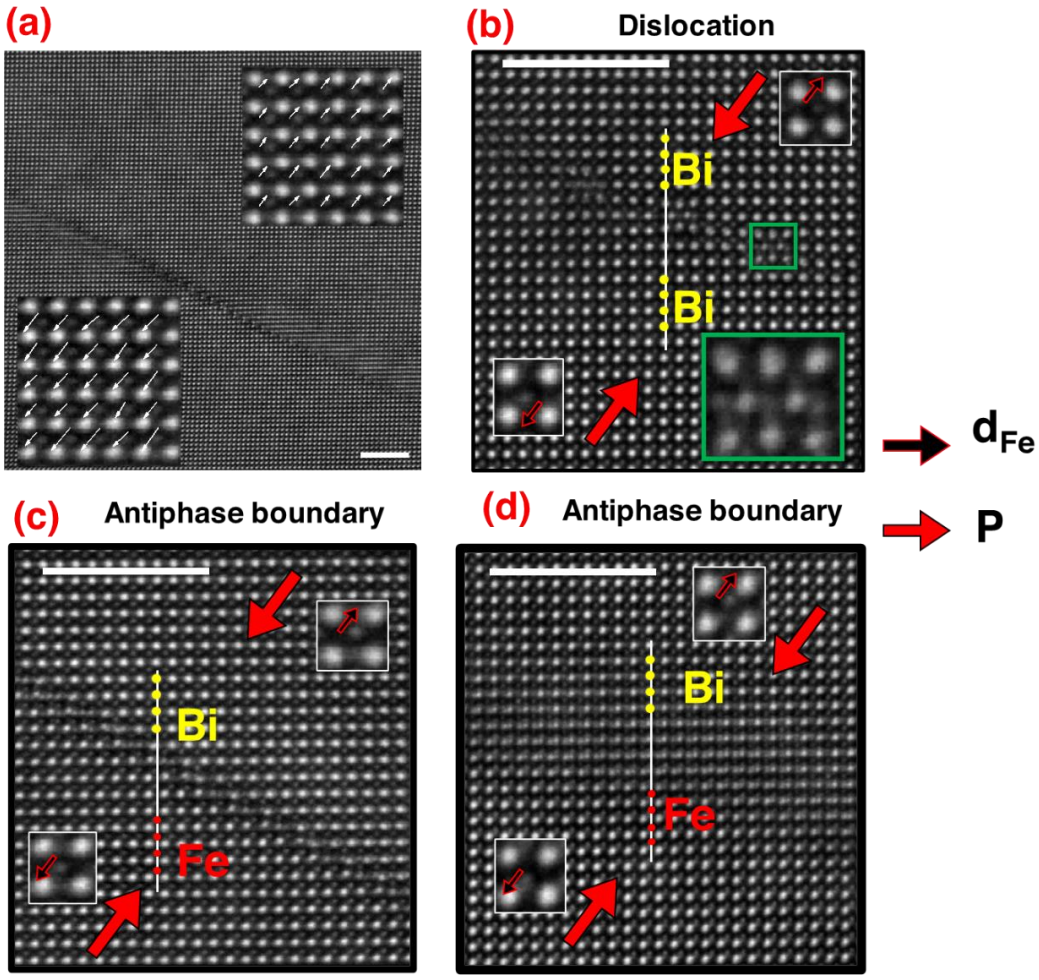

Figure S 3.2 (a) HAADF image of lamellar-like features. On each side of the lamellar-like features a close-up of 5x5 unit cells is shown, together with the overlapped Fe-displacement vectors.

Atomic resolution HAADF image on a location of the lamellar wall showing (b) a dislocation defect (green inset) and (c)-(d) antiphase boundaries (half unit cell shift from one domain to the other is marked: Bi-atomic columns align to Fe-atomic columns).

*The white scale bar marks 4 nm. The insets on each side of the defect show an one-unit cell close-up and the approximate direction of the Fe-displacement (black arrow ($\mathbf{d_{Fe}}$)) in respect to the center of Bi lattice. The direction of the polarization is indicated with red arrow (**P**).*

Supplementary 4 – **Original HAADF images**

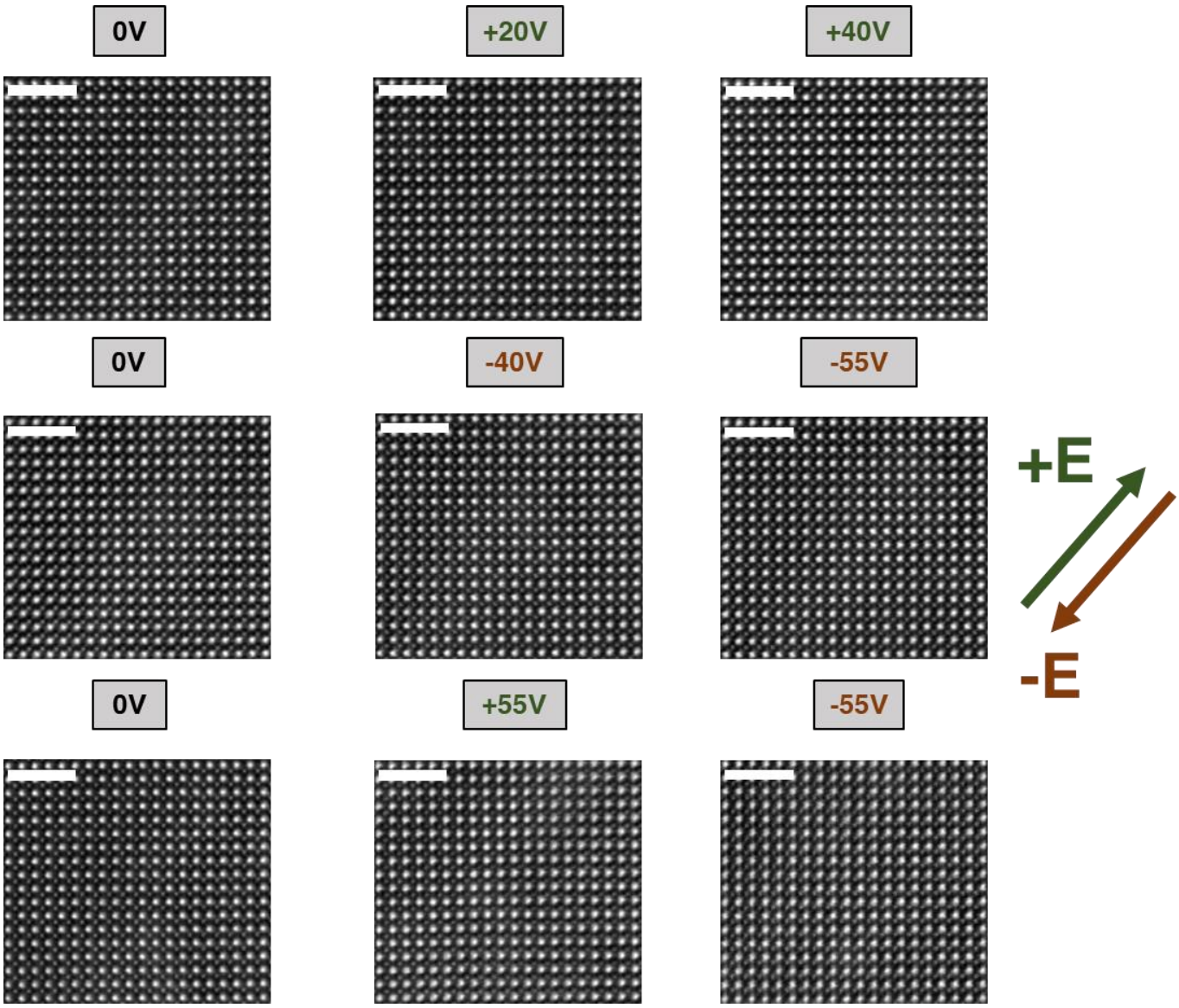

Figure S 4.1 Original HAADF images for the 0V, +20V, +40V, 0V, -40V, -55V, 0V, +55V and -55V sequence. The direction of the electric field is indicated by arrows. The images correspond to the experiment shown in Figure 2 in the main manuscript. Each HAADF image is an integration of 10 frames. The scale bar is 2 nm.

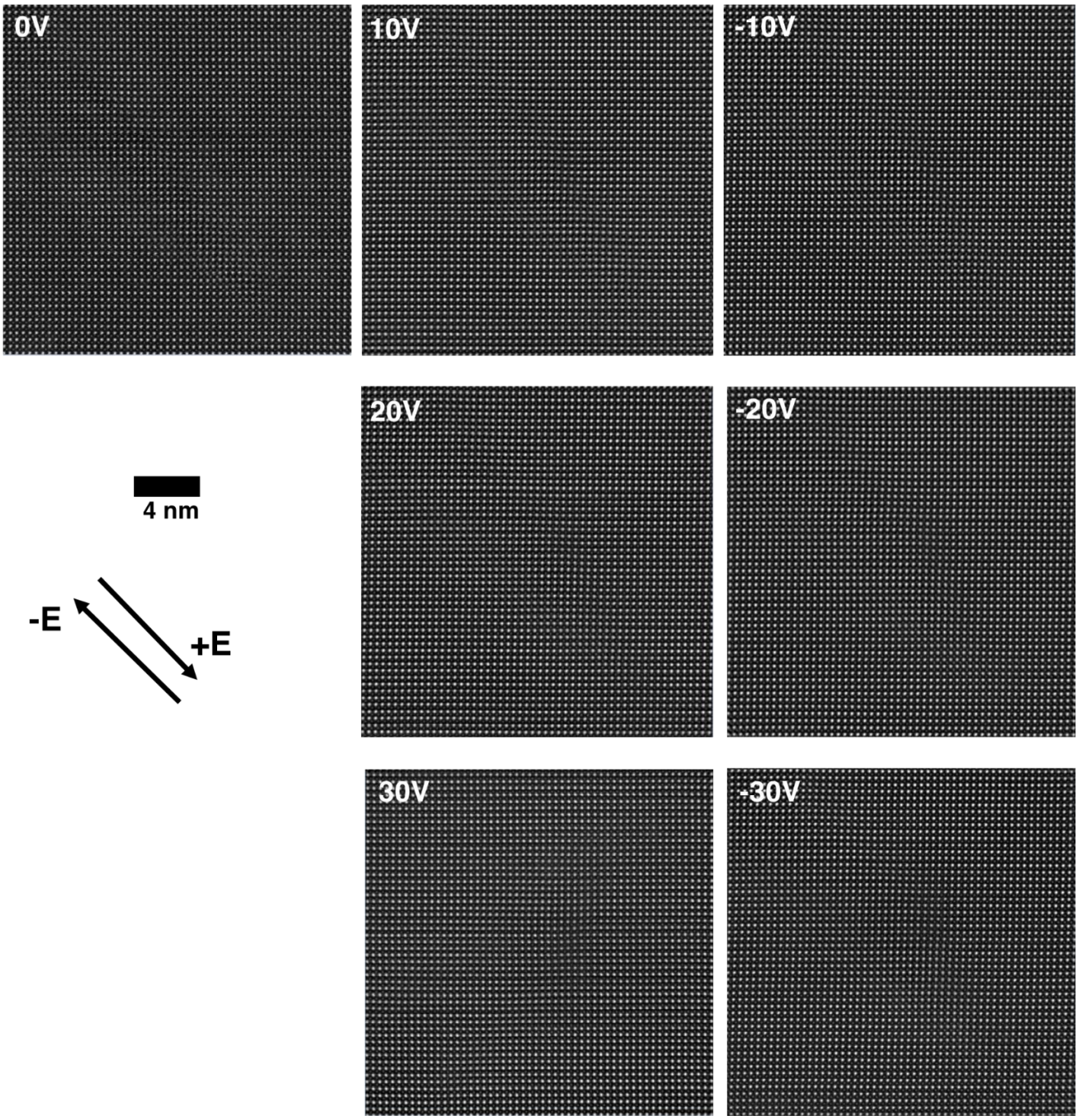

Figure S 4.2 Original HAADF images for the 0V, 10V, -10V, 20V, -20V, +30V and -30V sequence. The direction of the electric field is indicated by arrows. The images correspond to the experiment shown in Figure 3 in the main manuscript. Each HAADF image is one individual frame.

Supplementary 5 - **Displacement maps for all voltages following the experiment shown in Figure 2 in the main manuscript**

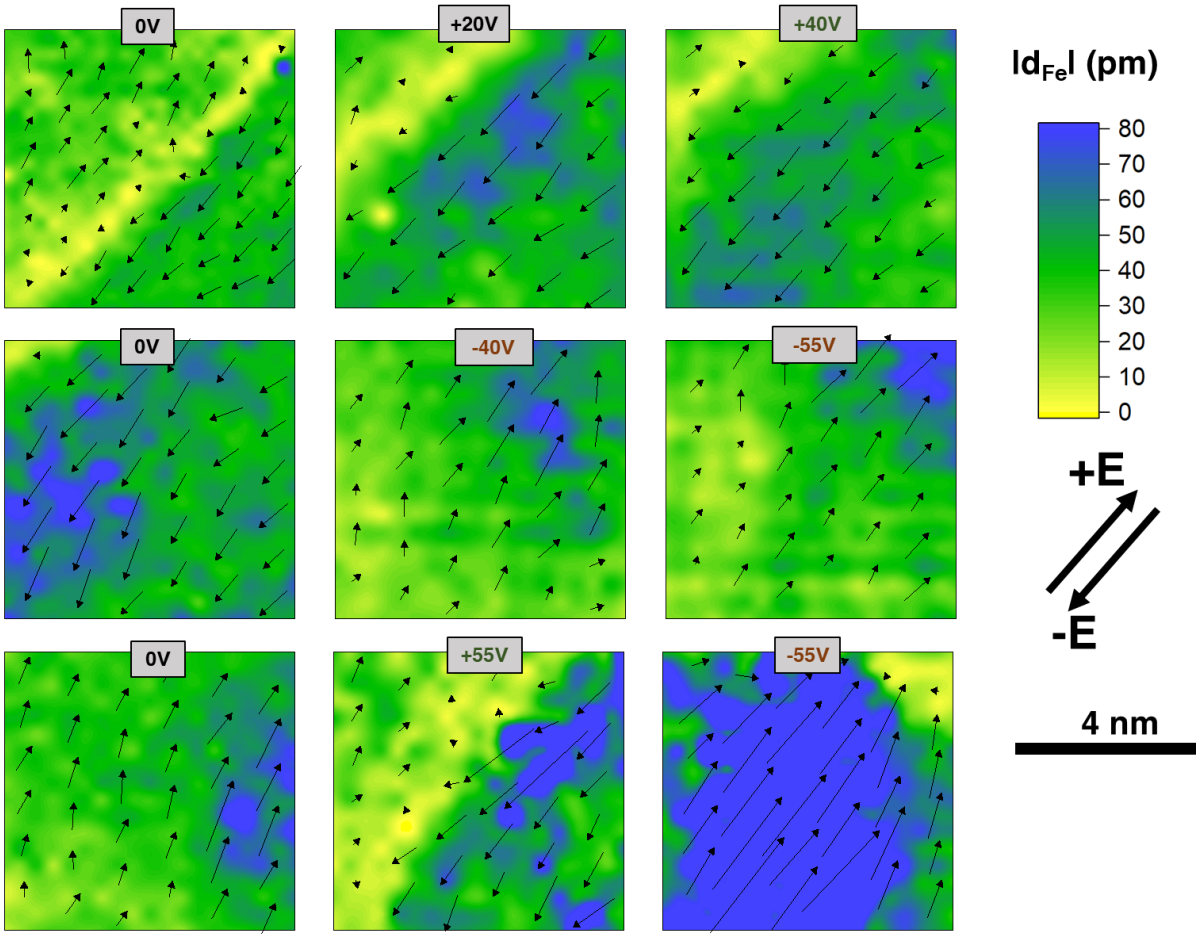

Figure S5 Fe-displacement map (black arrows) superimposed on the colored map of the value of Fe-displacement magnitude for the 0V, +20V, +40V, 0V, -40V, -55V, 0V, +55V and -55V sequence.

Supplementary 6– **Probing possible charged defects on the zigzag DWs.**

Probing Bi vacancies.

The normalized Bi-column intensities were determined from HAADF images using a previously reported method[5,11]. The detector's background intensity is subtracted from the intensity of each pixel in the raw HAADF image. Further, the intensities of the atomic columns were extracted by the integration of the pixel values within one sigma, approximating a Gaussian-type intensity distribution.

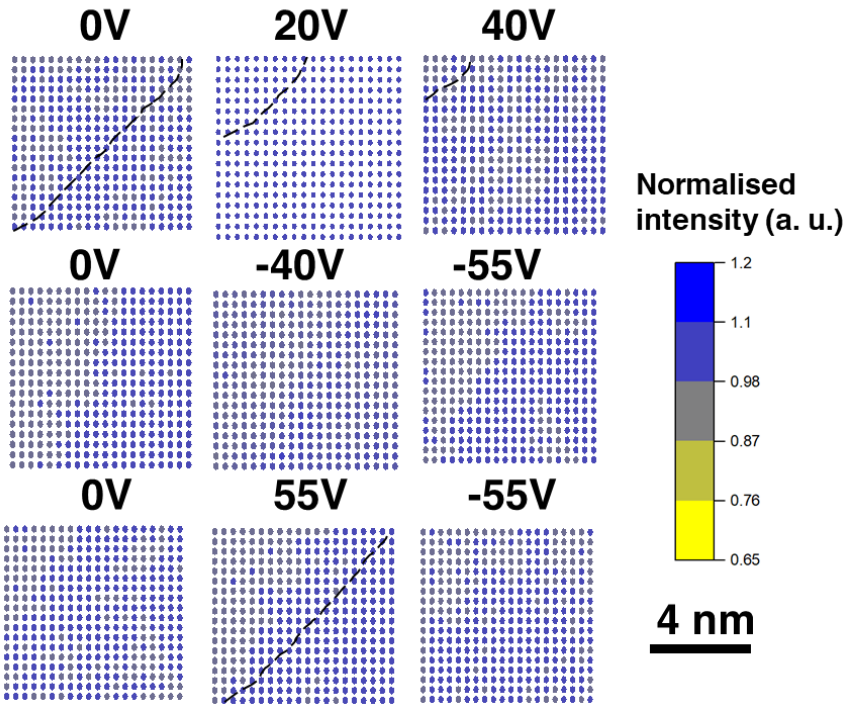

Figure S 6.1 Normalized Bi-atomic columns intensity maps in the following sequence of voltages: 0V, 20V, 40V, 0V, -40V, -55V, 0V, 55V and -55V for the experiment following the central part of the zigzag DWs (Figure 2 in the main manuscript). With black dotted line the position of the DW which moves is marked based on Fe-displacement map (Figure 2 in the main manuscript).

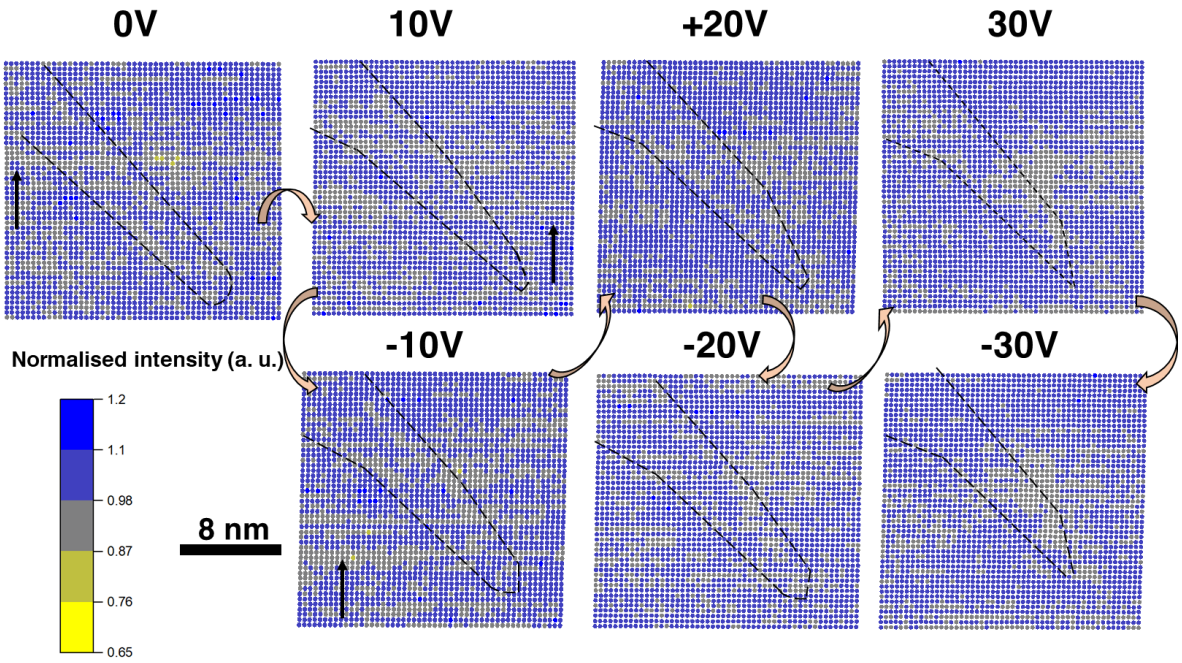

Figure S 6.2 Normalized Bi-atomic columns intensity maps in the following sequence of voltages: 0V, 10V, -10V, 20V, -20V, 30V, -30V for the experiment following the tip of the zigzag DWs (Figure 3 in the main manuscript). With black line the position of the DW is marked based on Fe-displacement map (Figure 3 in the main manuscript). Note that intensity drop extended along the horizontal it is likely due to scanning artefact and it is marked with black arrows

Probing Fe^{4+}

From the EELS spectra we extracted the energy onset difference between O-K and Fe-L_3 edges (chemical shift), which is sensitive to the oxidation state of Fe. Both on and off the DW, we detect a value of the chemical shift of about ΔE=178 eV, fingerprint of Fe^{3+}.[5]

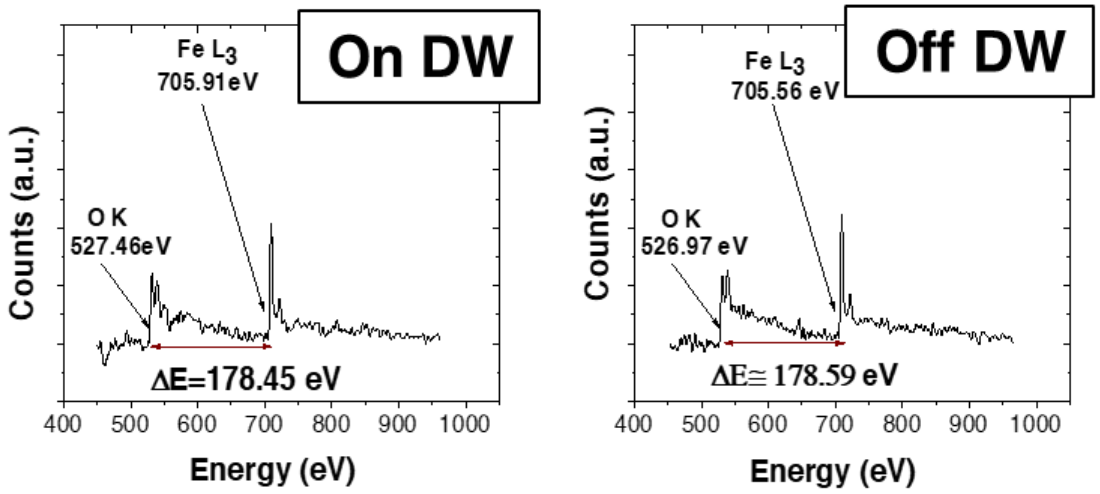

Figure S 6.3 EELS spectra on and off the location of the zigzag DWs. The energy onset ΔE difference between O-K and Fe-L_3 edges is shown.

Probing DWs' conduction

Piezoresponse force microscopy (PFM) and conductive atomic force microscopy (c-AFM) were performed using an atomic force microscope (AFM) Asylum Research, Molecular Force Probe 3D, Santa Barbara, CA, USA. A tetrahedrally shaped silicone AFM tip with a silicone cantilever, both coated with Ti/Ir, was used for the analyses (Asylec, AtomicForce F&E GmBH). Out-of-plane PFM imaging was performed in dual AC resonance tracking mode (DART) using an AC voltage of 10 V. The c-AFM imaging was performed by applying a DC voltage ranging from 5 to 30 V to the tip (the c-AFM image in Fig. S6.4 was acquired at 30V DC). The c-AFM investigation showed no increased conductivity on DWs (Fig. S6.4e).

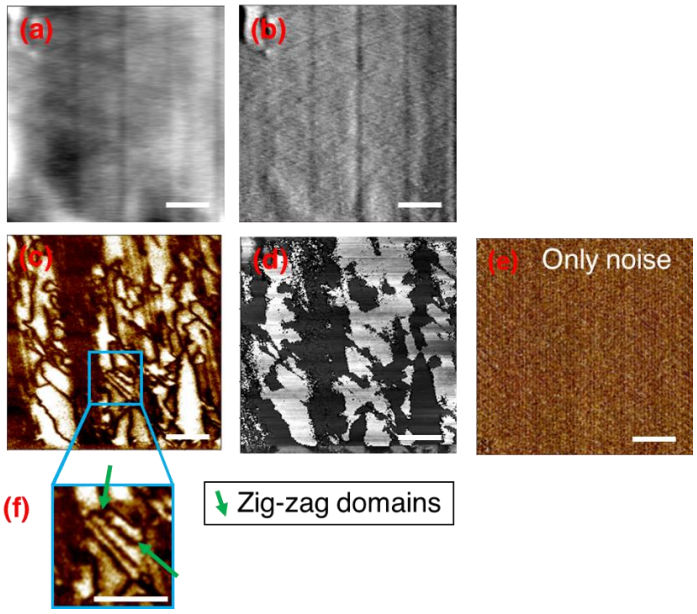

Figure S 6.4 Topography (a) height and (b) deflection; out-of-plane PFM DART (c) amplitude and (d) phase images; (e) c-AFM current image and (f) the closer look to the area marked in panel (c) by blue square. The scale bar marks 1 µm.

O vacancies on zigzag DW

The O K edge intensity appears to be slightly lower in the DW location (marked with black line in Figure S6.5) compared to the domain matrix (marked with red line in Figure S6.5). The present result suggests probable segregation of O vacancies point charged defects at the zigzag walls.

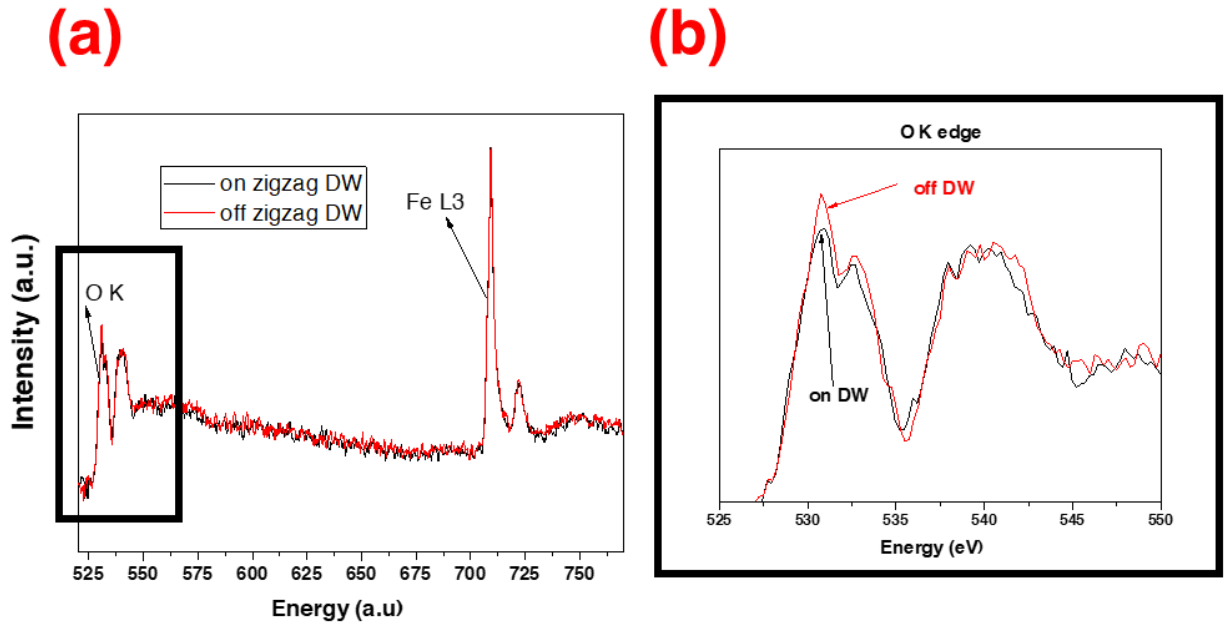

Figure S 6.5 (a) EELS spectra on and off the location of the zigzag DWs. (b) Close-up of the O K edge from the region marked with black rectangle in a).

Supplementary 7 - **BF images and Fe-displacement maps for all voltages following the experiment shown in Figure 3 in the main manuscript**

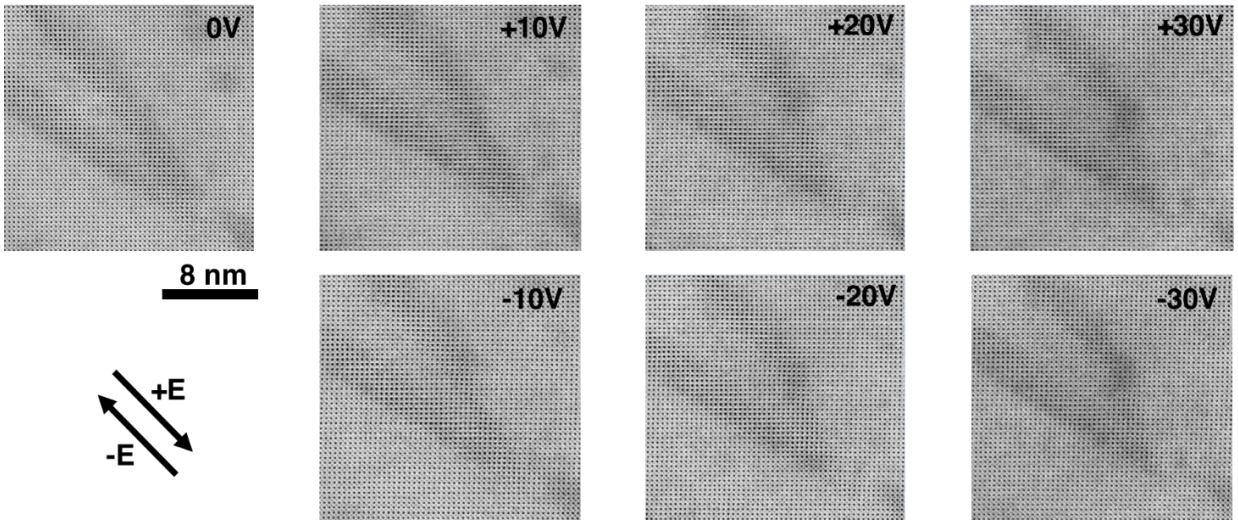

Figure S 7.1 Atomic resolution BF images at the wall location for 0V, +10V, -10V, +20V, -20V, +30V and -30V sequence. The BF images for 0V, +30V and -30V have been already shown in the main manuscript but for the sake of comparison we decided to show them together with the images for the other voltages.

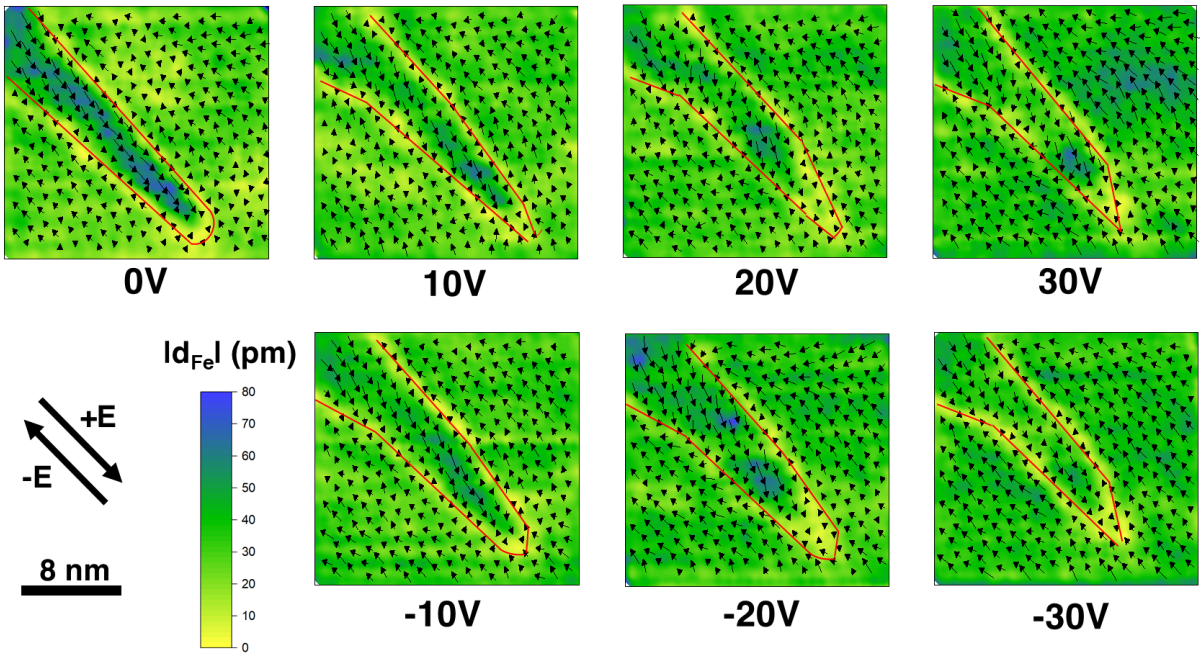

Figure S 7.2 Fe-displacement vector map (black arrows) overlaid on colored map of the Fe-displacement magnitude for 0V, 10V, -10V, 20V, -20V, 30V and -30V sequence. The DW region is marked with red line. The direction of the electric field is indicated by black arrows. The Fe-displacement vector map for 0V, 30V and -30V have been already shown in the main manuscript but for the sake of comparison we decided to show them together with the maps for the other voltages.

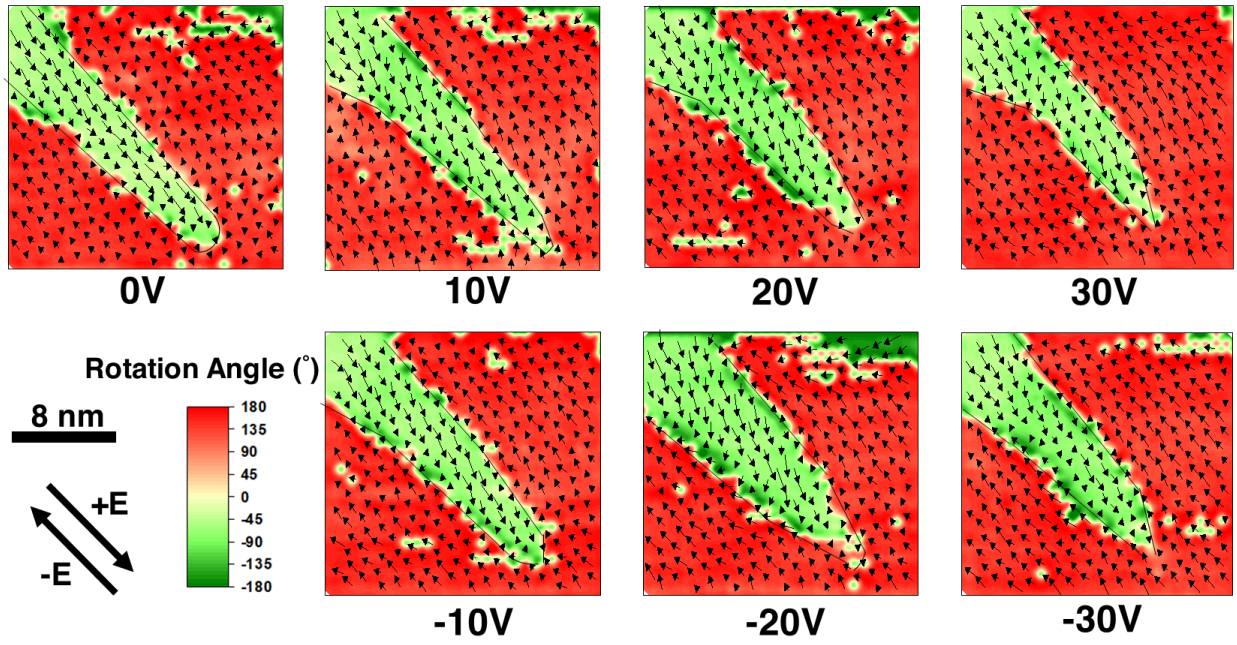

Figure S 7.3 Fe-displacement vector map (black arrows) overlaid on colored map of the Fe-displacement rotation angle for 0V, 10V, -10V, 20V, -20V, 30V and -30V sequence. The DW region is marked with black line. The direction of the electric field is indicated by black arrows.

Supplementary 8- **Estimations of the normal component of the Fe-displacement before and after the application of the electric field for the experiment following the tip of the zigzag DWs**

The amount of bound charge (σ) is given by the change of the normal polarization component to the DW plane: $-\sigma = \triangle \boldsymbol{P} \cdot \boldsymbol{n}$, where $\triangle \boldsymbol{P}$ is the difference between polarization of adjacent domains and $\boldsymbol{n}$ is the DW normal[13]. Polarization and Fe-displacement are in relation of direct proportionality[6], therefore, $-\sigma \sim \triangle \boldsymbol{d}$.

Three segments were considered to form the tip of the zigzag walls: DWI, DWII and apex. The normal component of Fe-displacement was calculated for each of these three segments at 0 and 30V.

The displacement vector (its magnitude and orientation) on either side of the wall was considered to be center of mass of the polar distribution (noted as $\boldsymbol{d_{1,2}}$).

The plane of the wall was evaluated from Fe-displacement maps.

The normal Fe-displacement component is: $\Delta \boldsymbol{d} = \boldsymbol{d_{1n}^{I,II,apex}} - \boldsymbol{d_{2n}^{I,II,apex}}$, where $\boldsymbol{d_{1n}^{I,II,apex}}$ and $\boldsymbol{d_{2n}^{I,II,apex}}$ represents the normal component of the Fe-displacement of Domain 1 and Domain 2, respectively, relative to the plane of DWI, DWII or the apex.

$\left|\boldsymbol{d_{1,2n}^{I,II,apex}}\right|$is calculated as $\left|\boldsymbol{d_{1,2n}^{I,II,apex}}\right| = \left|\boldsymbol{d_{1,2}}\right| \sin \theta_{1,2}^{I,II,apex}$ where $\theta_{1,2}^{I,II,apex}$ is the angle between the $\boldsymbol{d_{1,2}}$ vectors and the wall plane DWI, DWII or apex.

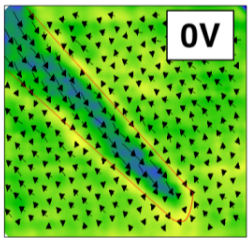

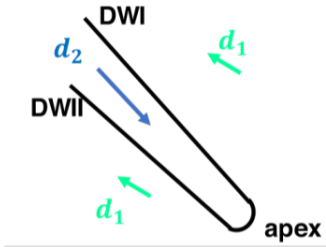

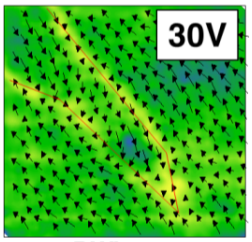

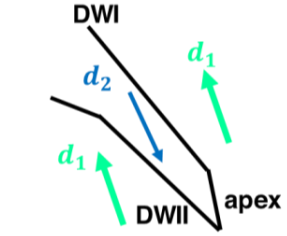

$\theta_1^I =< (\mathrm{DWI}, \boldsymbol{d_1}) = -17°$

$|\boldsymbol{d_{1n}^I}| = |\boldsymbol{d_1}| \sin\theta_1^I = -6\mathrm{pm}$

$\theta_2^I =< (\mathrm{DWI}, \boldsymbol{d_2}) = 0°$

$|\boldsymbol{d_{2n}^I}| = |\boldsymbol{d_2}| \sin\theta_2^I = 0\mathrm{pm}$

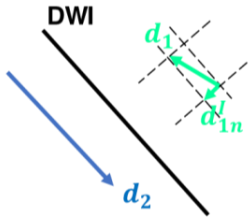

|Δdl|=6 pm

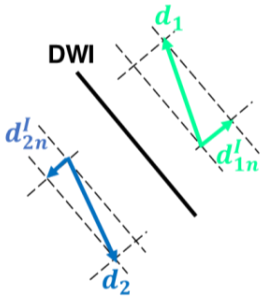

$\theta_1^I =< (\mathrm{DWI}, \boldsymbol{d_1}) = 23°$

$|\boldsymbol{d_{1n}^I}| = |\boldsymbol{d_1}| \sin\theta_1^I = 14\mathrm{pm}$

$\theta_2^I =< (\mathrm{DWI}, \boldsymbol{d_2}) = -17°$

$|\boldsymbol{d_{2n}^I}| = |\boldsymbol{d_2}| \sin\theta_2^I = -11\mathrm{pm}$

|Δdl|=25 pm

$\theta_1^{II} =< (\mathrm{DWII}, \boldsymbol{d_1}) = -11°$

$|\boldsymbol{d_{1n}^{II}}| = |\boldsymbol{d_1}| \sin\theta_1^{II} = -4\mathrm{pm}$

$\theta_2^{II} =< (\mathrm{DWII}, \boldsymbol{d_2}) = -6°$

$|\boldsymbol{d_{2n}^{II}}| = |\boldsymbol{d_2}| \sin\theta_2^{II} = -5\mathrm{pm}$

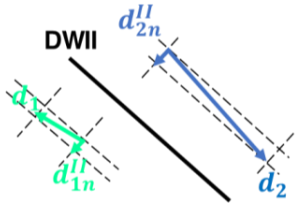

|Δdl|=1 pm

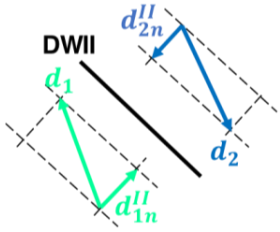

$\theta_1^{II} =< (\mathrm{DWII}, \boldsymbol{d_1}) = 29°$

$|\boldsymbol{d_{1n}^{II}}| = |\boldsymbol{d_1}| \sin\theta_1^{II} = 18\mathrm{pm}$

$\theta_2^{II} =< (\mathrm{DWII}, \boldsymbol{d_2}) = -23°$

$|\boldsymbol{d_{2n}^{II}}| = |\boldsymbol{d_2}| \sin\theta_2^{II} = -6\mathrm{pm}$

|Δdl|=24 pm

$\theta_1^{apex} =< (\mathrm{DWapex}, \boldsymbol{d_1}) = 99°$

$|\boldsymbol{d_{1n}^{apex}}| = |\boldsymbol{d_1}| \sin\theta_1^{apex} = 22\mathrm{pm}$

$\theta_2^{apex} =< (\mathrm{DWapex}, \boldsymbol{d_2}) = -83°$

$|\boldsymbol{d_{2n}^{apex}}| = |\boldsymbol{d_2}| \sin\theta_2^{apex} = -46\mathrm{pm}$

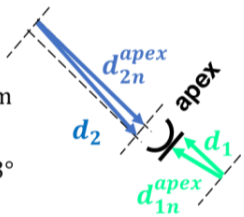

|Δdl|=68 pm

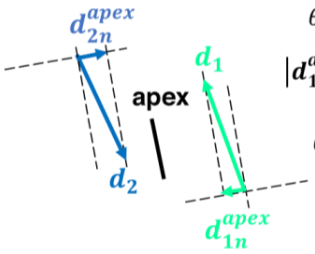

$\theta_1^{apex} =< (\mathrm{DWapex}, \boldsymbol{d_1}) = -13°$

$|\boldsymbol{d_{1n}^{apex}}| = |\boldsymbol{d_1}| \sin\theta_1^{apex} = -15\mathrm{pm}$

$\theta_2^{apex} =< (\mathrm{DWapex}, \boldsymbol{d_2}) = 7°$

$|\boldsymbol{d_{2n}^{apex}}| = |\boldsymbol{d_2}| \sin\theta_2^{apex} = 5\mathrm{pm}$

|Δdl|=20 pm

(1) Moering, J.. NEW FIB-OPTIMIZED E-CHIPS, 2018 https://www.protochips.com/news/fib-optimized-e-chips/ (accessed 2022-07-19).
(2) Ignatans, R.; Damjanovic, D.; Tileli, V. Local Hard and Soft Pinning of 180° Domain Walls in $BaTiO_3$ Probed by *in Situ* Transmission Electron Microscopy. *Phys. Rev. Materials* **2020**, *4* (10), 104403.
(3) Vogel, A.; Sarott, M. F.; Campanini, M.; Trassin, M.; Rossell, M. D. Monitoring Electrical Biasing of $Pb(Zr_{0.2}Ti_{0.8})O_3$ Ferroelectric Thin Films In Situ by DPC-STEM Imaging. *Materials* **2021**, *14* (16), 4749.
(4) Li, L.; Xie, L.; Pan, X. Real-time studies of ferroelectric domain switching: a review. *Rep. Prog. Phys.* **2019**, *82*, 26502.
(5) Rojac, T.; Bencan, A.; Drazic, G.; Sakamoto, N.; Ursic, H.; Jancar, B.; Tavcar, G.; Makarovic, M.; Walker, J.; Malic, B.; Damjanovic, D. Domain-Wall Conduction in Ferroelectric $BiFeO_3$ Controlled by Accumulation of Charged Defects. *Nat. Mater.* **2017**, *16* (3), 322–327.
(6) Nelson, C. T.; Winchester, B.; Zhang, Y.; Kim, S.-J.; Melville, A.; Adamo, C.; Folkman, C. M.; Baek, S.-H.; Eom, C.-B.; Schlom, D. G.; Chen, L.-Q.; Pan, X. Spontaneous Vortex Nanodomain Arrays at Ferroelectric Heterointerfaces. *Nano Lett.* **2011**, *11* (2), 828–834.
(7) Catalan, G.; Scott, J. F. Physics and Applications of Bismuth Ferrite. *Adv. Mater.* **2009**, *21* (24), 2463–2485.
(8) Streiffer, S. K.; Parker, C. B.; Romanov, A. E.; Lefevre, M. J.; Zhao, L.; Speck, J. S.; Pompe, W.; Foster, C. M.; Bai, G. R. Domain Patterns in Epitaxial Rhombohedral Ferroelectric Films. I. Geometry and Experiments. *J. Appl. Phys.* 1998, *83* (5), 2742–2753.
(9) Taherinejad, M.; Vanderbilt, D.; Marton, P.; Stepkova, V.; Hlinka, J. Bloch-Type Domain Walls in Rhombohedral $BaTiO_3$. *Phys. Rev. B* **2012**, *86* (15), 155138.
(10) Wang, W.-Y.; Tang, Y.-L.; Zhu, Y.-L.; Xu, Y.-B.; Liu, Y.; Wang, Y.-J.; Jagadeesh, S.; Ma, X.-L. Atomic Level 1D Structural Modulations at the Negatively Charged Domain Walls in $BiFeO_3$ Films. *Adv. Mater. Interfaces* **2015**, *2* (9), 1500024.
(11) Condurache, O.; Dražić, G.; Sakamoto, N.; Rojac, T.; Benčan, A. Atomically Resolved Structure of Step-like Uncharged and Charged Domain Walls in Polycrystalline $BiFeO_3$. *J. Appl. Phys.* **2021**, *129* (5), 054102.
(12) Jia, C.-L.; Jin, L.; Wang, D.; Mi, S.-B.; Alexe, M.; Hesse, D.; Reichlova, H.; Marti, X.; Bellaiche, L.; Urban, K. W. Nanodomains and Nanometer-Scale Disorder in Multiferroic Bismuth Ferrite Single Crystals. *Acta Mater.* **2015**, *82*, 356–368.
(13) *Topological Structures in Ferroic Materials*; Seidel, J., Ed.; Springer Series in Materials Science; Springer International Publishing: Cham, **2016**; Vol. 228.

Chapter 4

Voltage-Driven Ferroelectric Domain Dynamics in (K,Na)NbO_3 Investigated by In-Situ Transmission Electron Microscopy

Switching kinetics at the local scales is determined by local variations of the free energy, leading to a relatively inhomogeneous process.[84] In the present study, we monitor the ferroelectric switching dynamics in a (K,Na)NbO_3 single crystal, where mobile, needlelike DWs coexist and interact during switching with immobile DWs.

Our dynamic results show that immobile DWs act as randomly bound pinning defects, pinning areas of up to 0.35 μm^2. The specimen edge, which is an inherent interface in a capacitor-like device, promotes the nucleation of new domains.

With one polarity of the electric field, the needlelike DWs have a traditional forward tip movement until they encounter an obstacle (e.g., an immobile DW), after which they grow laterally. If the polarity of the electric field is reversed, the domains growth in the orthogonal direction. In this case, the needles grow as forward tip propagation and coalesce only up to a certain threshold voltage, after which the propagation stops, and the domains split into fine needles and nanodomains. This unexpected phenomenon could be a result of built-in stress as it correlates with an enhanced diffraction contrast (in BF/LAADF images).

During the switching process, discontinuities occur when two orthogonal needles meet, and a pinning event takes place. Pinning between orthogonal needles is overcome by further increasing the voltage.

We believe that the present results describing the ferroelectric kinetics of needlelike DWs in the presence of other defects, can contribute to the general knowledge on ferroelectric switching, since they are studied directly and locally.

This chapter addresses thesis objectives: 2 and 5.

Published in: O. Condurache, G. Dražić and A. Benčan, "Voltage-driven ferroelectric domain dynamics in (K,Na)NbO_3 investigated by in-situ transmission electron

microscopy," *Applied Physics Letters*, vol. 122, no. 20, pp. 202902, 2023, https://doi.org/10.1063/5.0149949 .

My contribution: I prepared the specimen by FIB. I performed the in-situ biasing STEM experiment. I analyzed the data. I interpreted the data, elaborated the concept of the manuscript and wrote the paper, together with the co-authors.

Applied Physics Letters ARTICLE pubs.aip.org/aip/apl

Voltage-driven ferroelectric domain dynamics in $(K,Na)NbO_3$ investigated by *in situ* transmission electron microscopy

Cite as: Appl. Phys. Lett. **122**, 202902 (2023); doi: 10.1063/5.0149949
Submitted: 10 March 2023 · Accepted: 3 May 2023 ·
Published Online: 15 May 2023

Oana Condurache,[1,2,a)] Goran Dražić,[1,2,3] and Andreja Benčan[1,2]

AFFILIATIONS

[1]Electronic Ceramics Department, Jožef Stefan Institute, 1000 Ljubljana, Slovenia
[2]Jožef Stefan International Postgraduate School, 1000 Ljubljana, Slovenia
[3]Department of Materials Chemistry, National Institute of Chemistry, 1001 Ljubljana, Slovenia

[a)]Author to whom correspondence should be addressed: oana.condurache@ijs.si

ABSTRACT

Ferroelectric domain dynamics is at the heart of any ferroelectric-based application. *In situ* transmission electron microscopy (TEM) offers an exciting opportunity to directly image ferroelectric switching and domain dynamics, revealing phenomena that might be concealed in macroscopic measurements. Here, we investigate the voltage-driven response of the mobile, needlelike domains and domain walls (DWs) of a $(K,Na)NbO_3$ single crystal (KNN_{sc}) using *in situ* TEM in a miniaturized capacitor. Our experimental results reveal that the immobile DWs can act as random bound pinning centers, pinning an area of up to 0.35 μm^2. The edge of the sample can promote the nucleation of new domains. Domain growth and coalescence are not always continuous but can be interrupted at a certain voltage in favor of fine domain splitting and the formation of nanoscale domains. Other discontinuities are generated in the functional response when two orthogonal, needlelike domains meet and soft-pinning events occur. These findings shed light on the kinetics of ferroelectric domains and are probably not limited to KNN_{sc}, being applicable to other perovskite-based ferroelectric materials where a needlelike domain morphology is present or where mobile and immobile DWs coexist.

The switching of polarization carries the functionality of any ferroelectric material. Switching dynamics is a complex process involving the movement of ferroelectric domain walls (DWs), the growth of domains, and the nucleation of new domains.

The response of ferroelectric domains and DWs is often investigated indirectly, e.g., by nonlinear ferroelectric/piezoelectric measurements[1,2] or *in situ* x-ray diffraction techniques,[2,3] which have contributed to our understanding of the relationship between the domain structure and functional properties. However, indirect studies only provide an average, collective response, and information about individual events cannot be decoupled. For example, a nonlinear response [e.g., a pinched polarization-field P(E) loop[2]] might be associated with the pinning of DWs; however, the origin of the pinning mechanism cannot be identified from bulk measurements alone.

To realize the full application potential of ferroelectrics, local imaging and a direct understanding of the kinetics of domains and DWs, especially in the presence of interfaces, become paramount. These interfaces, which are often present in real materials, can cause unpredictability in the switching process.[4] Interfaces that have been shown to affect the domain structure's response to an electric field include crystallographic defects,[4,5] other immobile DWs,[6] electrodes,[7] and grain boundaries.[8,9]

In this study, we observed the evolution of the ferroelectric domain structure of $K_{0.5}Na_{0.5}NbO_3$ single crystal (KNN_{sc}) *in situ* using (scanning) transmission electron microscopy-(S)TEM, in a new generation of capacitor-like configuration that provides, above all, a relatively homogeneous electric field distribution.[10–12] We explored the complex domain structure of KNN_{sc} and investigated the dynamics of needlelike DWs in the presence of other immobile domain boundaries. From a scientific perspective, single crystals are excellent candidates to gain insights into the ferroelectric switching process *in situ*, since they lack grain boundaries and have little to no porosity that could contribute to extrinsic effects. KNN is one of the most promising lead-free ferroelectrics.[13] From an applicative point of view,

Applied Physics Letters ARTICLE pubs.aip.org/aip/apl

KNN in single-crystal form was reported to exhibit a comparable[14] or higher[15] piezoelectric coefficient (d_{33}) and a significantly higher electrostrictive coefficient (M_{33}) than polycrystalline KNN.[14] The performance of a KNN-based single crystal is attributed to the presence of nanoscale-strain domains and a high density of DWs.[16,17] The dynamic behavior of the ferroelectric domains in KNN (especially a KNN single crystal) has rarely been reported.[18]

Here, we directly probe various local switching-associated events: soft-pinning associated with the tip-to-tip interaction between two perpendicular needle-domains; hard, long-range pinning near the immobile DWs; the reversible splitting of the domain structure into nanodomains; and the nucleation of new domains from the edge of the specimen.

The KNN_{sc} was grown using a solid-state, single-crystal growth method. More details about the crystal growth are given in Refs. 19 and 20. A monoclinic symmetry was assigned based on x-ray diffraction.[20] We transformed the monoclinic unit cell into the corresponding orthorhombic metric[21,22] to index the domain structure. In this paper, the pseudo-cubic notation is used (noted as pc).[23]

In an orthorhombic symmetry, the polar direction runs along $[110]_{pc}$,[15,24,25] leading to 12 polar orientations and the formation of 60°, 90°, 120°, and 180° DWs, depending on the angle between the polarization in the adjacent domains.[26] The planes to which these DWs are confined were previously discussed in detail.[24] Briefly, a 180° DW will lie on planes parallel to the direction of polarization (these walls are denoted W_∞); charged and uncharged 90° DWs are fixed to $\{100\}_{pc}$, while uncharged 120° and charged 60° are limited to $\{110\}_{pc}$ (denoted as W_f). The planes of charged 120° and uncharged 60° have irrational indices and depend on the piezoelectric and electrostrictive coefficients (denoted W_S).

Thus, the domain configuration in an orthorhombic symmetry will be rather complex, and, for a given zone axis, edge-on DWs will coexist alongside non-edge-on DWs. A sharp contrast at the DW can be seen when the DW is edge-on, i.e., the viewing direction is perpendicular to the DW plane; conversely, the DW is not edge-on when the wall's plane is tilted with respect to the viewing direction, and the projection at the DW site is diffuse and shows an overlap between the two domains.

A common domain structure of the KNN_{sc}, investigated by TEM in $[100]_{pc}$, is shown in Fig. 1. Generally, three characteristic features can be seen in a $[100]_{pc}$-oriented specimen: irregularly shaped features [white arrow in Figs. 1(a) and 1(b)], needlelike domains [closed, blue arrow in Fig. 1(b)], and fine irregular lamellar domains [open, black arrow in Fig. 1(b)].

The irregularly shaped features can be seen throughout the TEM specimen [Fig. 1(a)]. These features, which show a strong diffraction contrast [Figs. 1(a) and 1(c)], are not always located on the main crystallographic planes. The crystal lattice at their location is tilted with respect to the electron beam, as shown by an atomic resolution STEM-High Angle Annular Dark Field (STEM-HAADF) image [Fig. 1(d)]. Therefore, we classify these features as being DWs that are not edge-on in the direction of the beam. At the same time, the two domains on each side of the non-edge-on DW have a sharp and regular atomic contrast [Fig. 1(d)].

The needlelike DWs are close to the $\{100\}_{pc}$ planes, which, based on the assumption of mechanical compatibility and electrical neutrality,[25] implies that they are of the 90°-type. While a nominally head-to-tail configuration is assumed for the body of these domains to preserve electrical neutrality, an accumulation of bound charge occurs at the curved tip.[5] This needlelike morphology was previously associated with 90° DWs.[27–29] Selected-area electron diffraction (SAED) on a needlelike DW is shown in Fig. 1(e) and demonstrates the splitting of certain reflections, due to the polarization rotation from one domain to another. The experimental SAED agrees well with a simulated SAED on a 90° DW when the polarization is in the plane of the viewing direction [as shown in the sketch in Fig. 1(f)]. More details about the SAED simulation are given in the supplementary material, 1.

The fine lamellar structure might be a 180° DW structure, as discussed in a previous study.[20]

We have gone one step further and tackled the response of ferroelectric domains in KNN_{sc} during the application of an electric field using *in situ* STEM. In the biasing experiment, the specimens are confined to a capacitor-like configuration with Pt-electrodes on the side. The end-voltage values are ±55 V. Details about the *in situ* experimental set-up and the focused-ion-beam (FIB) specimen-preparation are given in the supplementary material, 2, and described in detail elsewhere.[10]

Figure 2(a) shows a STEM-Bright Field (STEM-BF) image of the entire FIB lamella before the application of the electric field. Here, the non-edge-on DWs cover the entire specimen prepared using the FIB. A close-up of the area marked with a white rectangle in Fig. 2(a) reveals that alongside the non-edge-on DW, the needlelike domain structure dominates[11] [STEM-BF and STEM-Low Angle Annular Dark Field (STEM-LAADF) in Fig. 2(c)].

For comparison, the same areas are shown at +55 V, which is the end value of the applied voltage [Figs. 2(b) and 2(d)]. The direction of the electric field is perpendicular to the electrodes and is indicated in Fig. 2 (it forms an angle of 22° with $[100]_{pc}$).

A first observation is that the non-edge-on walls hardly respond to the electric field bias, i.e., they are overall immobile [compare Figs. 2(a) and 2(b)].

The needlelike domain pattern, on the contrary, clearly responds to the electrical stimuli [compare Figs. 2(c) and 2(d)]. The complex dynamics of the needlelike domain pattern will be discussed in the next paragraph.

One hypothesis is that the polar direction in the needlelike DWs is favorable to the direction of the electric field. In contrast, the non-edge-on DW could separate domains, for which the polarization has an unfavorable orientation. Another possible reason for the non-edge-on DWs being immobile is pinning on defects, which can be crystallographic defects or point-charge defects. The analysis presented in Fig. 1(d) does not reveal discontinuities in the lattice; however, we do not exclude the possibility that the immobile DWs couple with crystallographic defects such as antiphase boundaries.[30] In addition, point-charge defects can be present (such as oxygen vacancies or alkaline vacancies[31]).

Figure 3 shows the evolution of the needlelike pattern at different bias voltages. We chose to observe a representative region, for which the initial domain configuration includes a set of domains approximatively parallel to each other with walls that lie on $\{100\}_{pc}$ (colored red), perpendicular to them is another set of domains on $\{010\}_{pc}$ (colored blue), and the domain matrix (in the original gray scale). The successive images at different voltages are obtained slightly off axis to enhance the domain contrast.

To easily follow the evolution of the domain structure, the corresponding region for each domain set was left colored in Fig. 3(a).

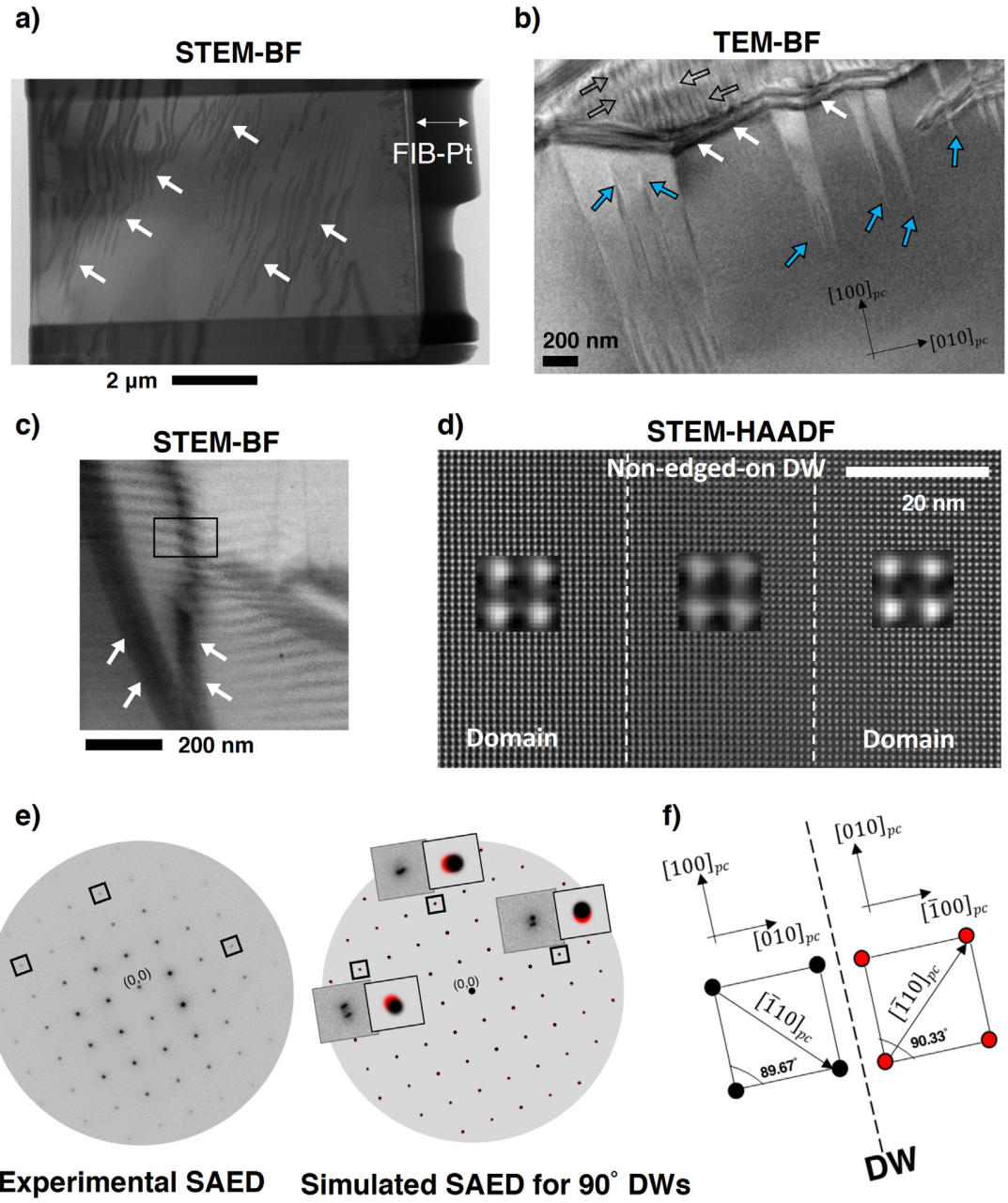

FIG. 1. (a) STEM-BF image of a FIB specimen lamella of KNN_{sc}. (b) TEM-BF image of different domain morphologies in KNN_{sc}. (c) STEM-BF of a non-edge-on feature. Non-edge-on features, needlelike, and fine lamellar domain structure are marked with white, blue, and black arrows, respectively. (d) STEM-HAADF atomic resolution image of the region marked with a black rectangle in (c). The inset represents one unit cell. Strong bright contrast corresponds to Nb atomic columns. (e) Experimental SAED on needle-shaped DWs, together with simulated SAED pattern across 90° DWs with in-plane polar axis. The insets show side-by-side a zoom-in of some experimental and simulated reflections. (f) Schematics of the 90° DW configuration simulated in (e). The polarization direction is indicated.

The original STEM-BF and STEM-LAADF images can be seen in the supplementary material, 3. In Fig. 3, only one bias cycle is shown (0 to +55 V to −55 to 0 V); the complete bias cycle is shown in the supplementary material, 4.

Due to the lack of direct technique capabilities, the actual polar configuration is concealed. However, we can rely on indirect assumptions to offer a hypothesis on the polarization configuration. We have already discussed that a plausible assumption is that the needlelike

Applied Physics Letters ARTICLE pubs.aip.org/aip/apl

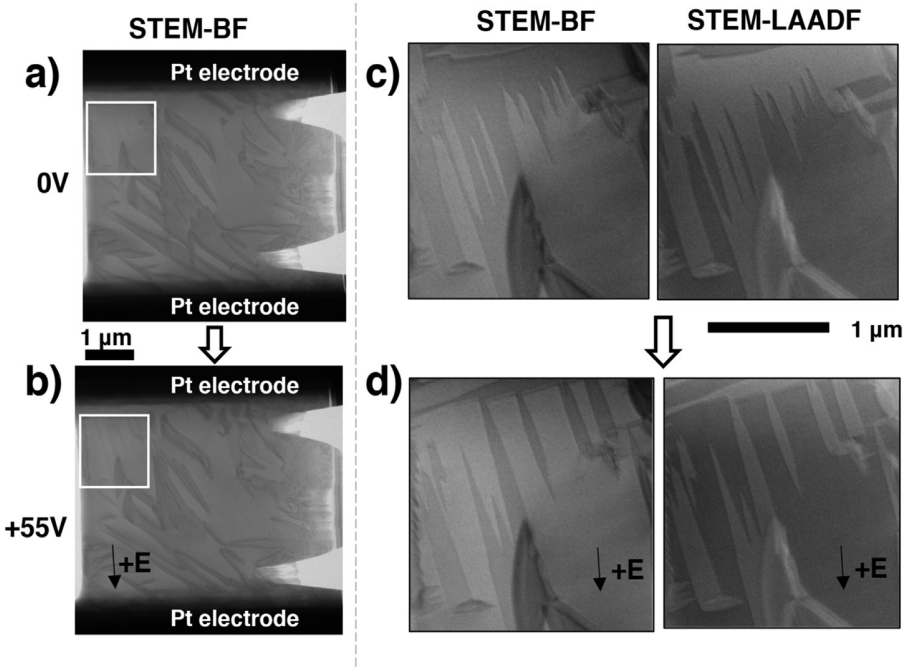

FIG. 2. (a) STEM-BF image of the FIB lamella fabricated on the *in situ* biasing chip at (a) 0 and (b) 55 V. The STEM-BF and STEM-LAADF of the magnified area marked with a white rectangle are shown at (c) 0 and (d) 55 V. The position of the electrodes and the approximate direction of the electric field are indicated.

domain walls are 90° DWs with the polarization in the viewing plane. Another assumption is that the walls are uncharged, except for the very tip of the needle where the charge accumulates. On the positive side of the voltage, the red domains grow. Thus, the polarization of the red domains is favorable for the direction of the electric field, while the gray matrix, which shrinks, is not.[11] On the other hand, the blue domains grow when the electric field is flipped to the negative side. With the black arrow in Fig. 3(a) for the 0 V image, we marked what

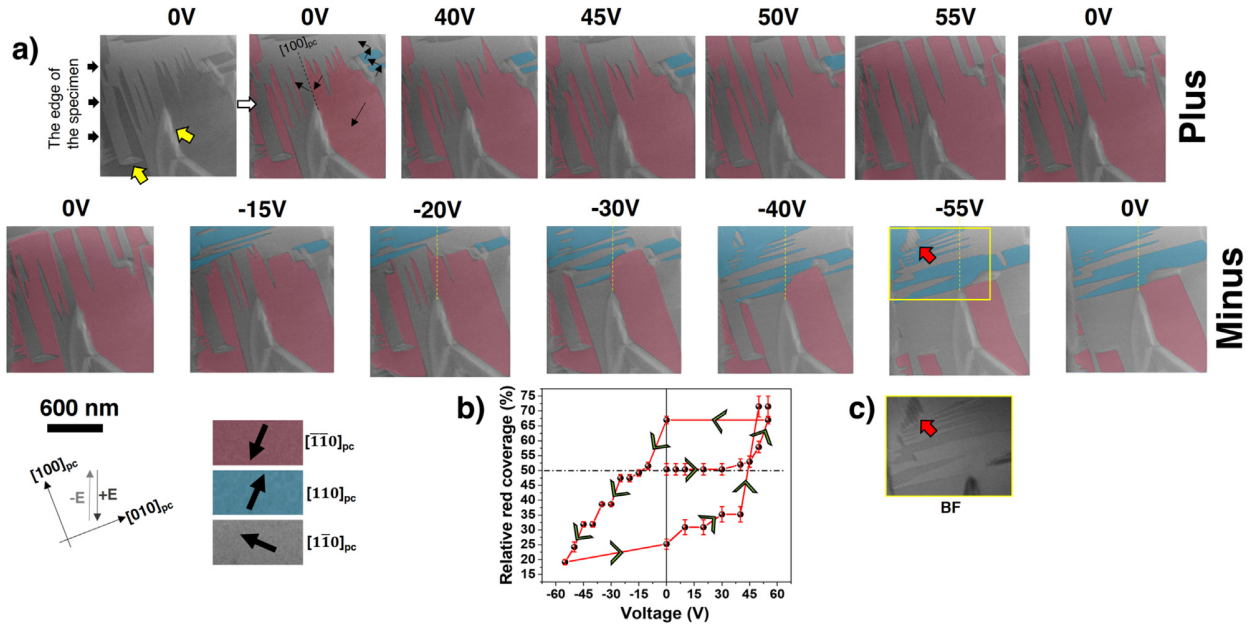

FIG. 3. (a) Evolution of the domain structure at different voltages. A sequence of false-colored STEM-LAADF images is shown. A possible polar direction for the red, blue, and gray matrix domains is indicated. At 0 V, a white arrow marks the presence of an immobile DW. (b) Plot of the relative coverage of the red domains as a function of voltage. The error bars represent standard deviation. (c) A STEM-BF close-up at −55 V of the yellow-highlighted region. The strong contrast corresponding to the nano-islands is marked with a red arrow.

Applied Physics Letters ARTICLE pubs.aip.org/aip/apl

such a configuration could be: the polar axis in red domains along $[\bar{1}\bar{1}0]_{pc}$, along $[1\bar{1}0]_{pc}$ in the matrix, and along $[110]_{pc}$ in the blue domains.

Let us now explore the kinetics of domains and DWs when an electric field is applied.

The initial domain configuration is dominated by a comb of needles (red). When the polarity of the voltage is positive, they grow by tip motion and maintain a needlelike morphology, if they have a free path. When they encounter an obstacle (in this case, another DW on the top of the observable area), they start growing sideways and they coalesce. The needlelike pattern changes to a rather parallelepipedal-shape pattern. This behavior is a classic domain evolution during polarization switching.[32] On the positive side, we do not observe nucleation of any new domains. The red domains show no back-switching when the voltage is turned off.

When the voltage changes polarity (conventionally labeled as negative in the paper), the switching occurs as a combination between the retraction of the "red" domains and the nucleation/growth of the "blue" domains. Figure 3(b) shows the evolution of the area of the red domains as a function of a cyclic electric potential. The coverage of a set of domains is proportional to the polarization, and its plot vs voltage is an illustration of a local polarization vs electric field [P(E)] hysteresis loop. In this case, the plot resembles a "hard" ferroelectric loop, and its most striking feature is the horizontal shift on the voltage axis, indicating a built-in electric field, probably due to asymmetric electrodes.[33] Some other discontinuities that characterize the switching process in Fig. 3(b) will be discussed later in the context of pinning.

The switching on the negative side shows a few particularities. First, some of the blue domains start nucleating from the edge of the specimen (−15 V), while others nucleate from the existing red domains, indicating the important role of interfaces in the kinetics of domains in a miniaturized device. A striking feature is that while on the positive voltage, the number of DWs decreases, following the growth and coalescence, the number of DWs on the negative side increases (Fig. 4). The set of blue domains growing from the edge of the sample along $[010]_{pc}$ stop at a certain voltage (−30 V), after which they retract and split, forming fine needles. The question arises as to why the growth of the domains is impeded, and they stabilize by forming a fine structure? One possible scenario is that when the negative voltage is applied, internal stresses are created, and the system reorganizes into nanodomains to release the emerging strain. In addition, some nano-islands form within the blue domains, which, as Fig. 3(c) shows, exhibit a strong diffraction contrast, indicating increased strain. This process is completely reversible, and when the voltage is turned off (0 V), the splitting reverses and the nano-islands disappear. The nucleation of nanodomains by mechanical loading was previously reported.[34–36]

Pinning during polarization reversal is a recurring event in this experiment. The area of red/blue-domain coverage as a function of the applied potential is shown in Fig. 5.

As mentioned earlier, there could be a built-in electric field that lowers the switching threshold on the negative polarity. As seen in Figs. 3(a) and 5(a), the domain pattern is pinned until +40 V, but for the negative polarity, the switching begins at −10 V.

Another interesting observation is that the regions near the pre-existing, immobile DWs are frozen (Fig. 3), regardless of their polarization direction (both the red and "gray" domains are pinned). This makes the immobile DWs act like random bound pinning defects. The interaction is relatively long range, and an area of up to 0.35 μm^2 is pinned for the voltage range used (±55 V). The pinning mechanism could be a complex interplay between electrostatic and strain fields.[37]

A few distinct steps can be seen in the plot of the coverage area for both the red and blue domains for the negative voltage polarity [indicated by a black arrow in Fig. 5(a) at −30 and −40 V]. These discontinuities, reflected in the local P(E) loop, are often referred to as a "crackling" noise or Barkhausen pulses.[12] The steps mark random, soft-pinning events, and, in the present case, we can clearly correlate them with a domain–domain interaction [Fig. 5(b)]. Explicitly, this event takes place when two, perpendicular, needlelike domains come into contact [the tip of a red needle meets the tip of a blue needle, Fig. 5(c)]. As suggested by theoretical calculations, the tip-to-tip arrangement of needlelike 90° DWs marks a metastable equilibrium configuration and can deepen the switching potential well, leading to soft pinning.[12,28] When the needles interact, a strong strain field is generated [as directly evidenced by the strong contrast in the STEM-BF image in Fig. 5(c)]. It is possible that the interaction between two tips is also mediated by an electrostatic field, since the two tips are strongly charged.

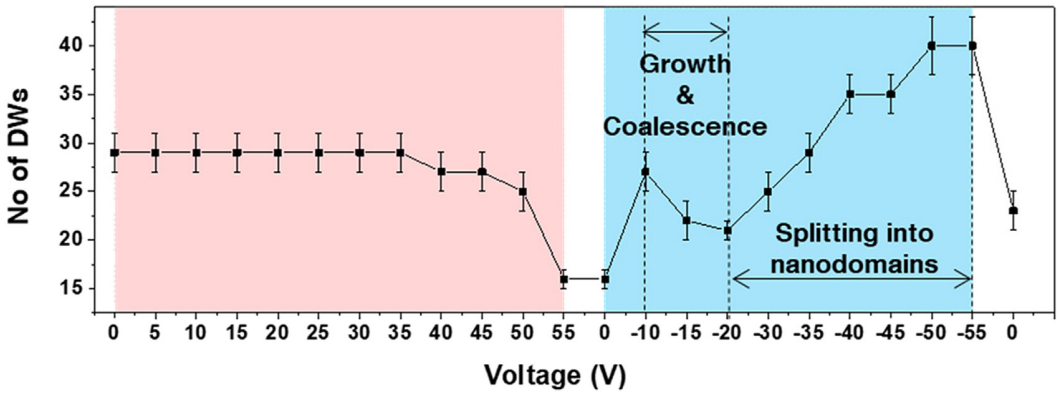

FIG. 4. Evolution of the number of DWs as a function of applied voltage. The error bars represent ±7% uncertainty.

Applied Physics Letters ARTICLE pubs.aip.org/aip/apl

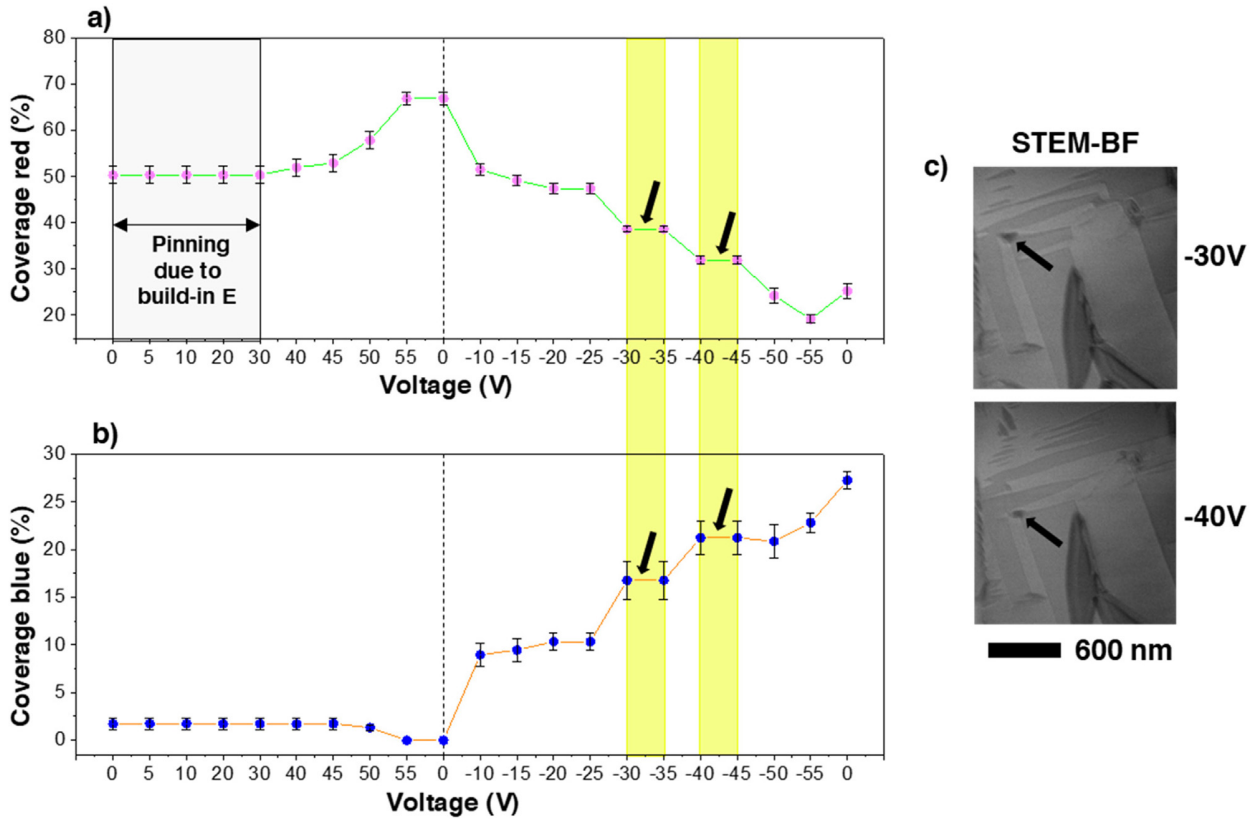

FIG. 5. Coverage of (a) red-marked and (b) blue-marked set of domains (from Fig. 1). The error bars represent standard deviation. Steps in the coverage plot are indicated at −30 and −40 V. (c) A sequence of STEM-BF images at −30 and −40 V. Intersection of two orthogonal domains is indicated, corresponding to the enhanced strain contrast in the STEM-BF images.

In summary, the TEM analysis of $[100]_{pc}$-oriented KNN_{sc} revealed needlelike and fine, lamellar domain structures alongside irregular features identified as non-edge-on DWs. When the specimen was prepared in a capacitor-like configuration with side electrodes, the needlelike structure surrounded by non-edge-on DWs dominated. The comb of needlelike DWs showed high mobility during the application of an electric field, in contrast to the non-edge-on DWs, which did not respond. The coverage area of a set of needlelike domains vs voltage illustrated a polarization–electric field loop, marking a typical ferroelectric hysteretic behavior. We showed that domain growth and coalescence can be arrested, followed by the domain retraction and formation of a high density of nano-strain domains. Our data suggest that this is a consequence of stress buildup. The experimental results prove that the main mechanism of pinning is on preexisting immobile DWs, which restrict the movement of the needlelike mobile DWs. Meanwhile, the edge of the specimen promotes the nucleation of new domains. We directly and locally monitored other discontinuities in the switching process, associated with soft pinning, which occurs when the tips of two orthogonal, needlelike domains meet, with the interaction mediated by strain. We believe that our results, derived from the direct imaging of domain dynamics in the presence of interfaces, give fundamental insights into ferroelectric switching in KNN_{sc} and can potentially provide input for simulations.

See the supplementary material for details about selected-area electron diffraction simulation (1), *in situ* biasing experimental procedure (2), the original STEM-BF and STEM-LAADF images (3), and the false-colored STEM-LAADF images for the complete bias cycle (4).

This work was supported by the Slovenian Research Agency in the frame of young-researcher program and core funding P2-0105, projects J2-2497, J2-3041, J2-4637, and BI-TR/20-23-003.

AUTHOR DECLARATIONS

Conflict of Interest

The authors have no conflicts to disclose.

Author Contributions

Oana Condurache: Conceptualization (equal); Investigation (lead); Methodology (equal); Validation (lead); Visualization (lead); Writing – original draft (lead); Writing – review & editing (equal). **Goran Dražić:** Conceptualization (equal); Investigation (supporting); Methodology (equal); Resources (supporting); Validation (supporting); Visualization (supporting); Writing – review & editing (equal). **Andreja Benčan:** Conceptualization (equal); Investigation (supporting); Methodology (equal); Project administration (lead); Resources (lead); Supervision

(lead); Validation (supporting); Visualization (supporting); Writing – review & editing (equal).

DATA AVAILABILITY

The data that support the findings of this study are available from the corresponding author upon reasonable request.

REFERENCES

[1]T. Rojac, H. Ursic, A. Bencan, B. Malic, and D. Damjanovic, Adv. Funct. Mater. **25**, 2099 (2015).
[2]M. Otonicar, M. Dragomir, and T. Rojac, J. Am. Ceram. Soc. **105**, 6479 (2022).
[3]A. Pramanick, D. Damjanovic, J. E. Daniels, J. C. Nino, and J. L. Jones, J. Am. Ceram. Soc. **94**, 293 (2011).
[4]M. L. Jablonski, S. Liu, C. R. Winkler, A. R. Damodaran, I. Grinberg, L. W. Martin, A. M. Rappe, and M. L. Taheri, ACS Appl. Mater. Interfaces **8**, 2935 (2016).
[5]C. R. Winkler, A. R. Damodaran, J. Karthik, L. W. Martin, and M. L. Taheri, Micron **43**, 1121 (2012).
[6]P. Yudin, K. Shapovalov, T. Sluka, J. Peräntie, H. Jantunen, A. Dejneka, and M. Tyunina, Sci. Rep. **11**, 1899 (2021).
[7]J. K. Lee, G. Y. Shin, K. Song, W. S. Choi, Y. A. Shin, S. Y. Park, J. Britson, Y. Cao, L.-Q. Chen, H. N. Lee, and S. H. Oh, Acta Mater. **61**, 6765 (2013).
[8]D. M. Marincel, H. R. Zhang, J. Britson, A. Belianinov, S. Jesse, S. V. Kalinin, L. Q. Chen, W. M. Rainforth, I. M. Reaney, C. A. Randall, and S. Trolier-McKinstry, Phys. Rev. B **91**, 134113 (2015).
[9]W. Qu, X. Zhao, and X. Tan, J. Appl. Phys. **102**, 084101 (2007).
[10]O. Condurache, G. Dražić, T. Rojac, H. Uršič, B. Dkhil, A. Bradeško, D. Damjanovic, and A. Benčan, Nano Lett. **23**, 750 (2023).
[11]R. Ignatans, D. Damjanovic, and V. Tileli, Phys. Rev. Mater. **4**, 104403 (2020).
[12]R. Ignatans, D. Damjanovic, and V. Tileli, Phys. Rev. Lett. **127**, 167601 (2021).
[13]S. Zhang, B. Malič, J.-F. Li, and J. Rödel, J. Mater. Res. **36**, 985 (2021).
[14]H. Uršič, A. Benčan, M. Škarabot, M. Godec, and M. Kosec, J. Appl. Phys. **107**, 033705 (2010).
[15]J. Koruza, H. Liu, M. Höfling, M.-H. Zhang, and P. Veber, J. Mater. Res. **35**, 990 (2020).
[16]K. Xu, J. Li, X. Lv, J. Wu, X. Zhang, D. Xiao, and J. Zhu, Adv. Mater. **28**, 8519 (2016).
[17]X. Lv, X. Zhang, and J. Wu, J. Mater. Chem. A **8**, 10026 (2020).
[18]H. Guo, S. Zhang, S. P. Beckman, and X. Tan, J. Appl. Phys. **114**, 154102 (2013).
[19]J. Tellier, B. Malic, B. Dkhil, D. Jenko, J. Cilensek, and M. Kosec, Solid State Sci. **11**, 320 (2009).
[20]A. Benčan, E. Tchernychova, M. Godec, J. Fisher, and M. Kosec, Microsc. Microanal. **15**, 435 (2009).
[21]H. Deng, H. Zhang, X. Zhao, C. Chen, X. Wang, X. Li, D. Lin, B. Ren, J. Jiao, and H. Luo, CrystEngComm **17**, 2872 (2015).
[22]G. Shirane, R. Newnham, and R. Pepinsky, Phys. Rev. **96**, 581 (1954).
[23]Y. Inagaki, K. Kakimoto, and I. Kagomiya, J. Am. Ceram. Soc. **93**, 4061 (2010).
[24]E. Wiesendanger, Czech. J. Phys. **23**, 91 (1973).
[25]S. Mantri and J. Daniels, J. Am. Ceram. Soc. **104**, 1619 (2021).
[26]J. Hirohashi, K. Yamada, H. Kamio, M. Uchida, and S. Shichijyo, J. Appl. Phys. **98**, 034107 (2005).
[27]F. Rubio-Marcos, A. Del Campo, R. E. Rojas-Hernandez, M. O. Ramírez, R. Parra, R. U. Ichikawa, L. A. Ramajo, L. E. Bausá, and J. F. Fernández, Nanoscale **10**, 705 (2018).
[28]D. Sui and J. E. Huber, Eur. J. Mech. A **80**, 103919 (2020).
[29]X. Y. Qi, H. H. Liu, and X. F. Duan, Appl. Phys. Lett. **89**, 092908 (2006).
[30]R. Eitel and C. A. Randall, Phys. Rev. B **75**, 094106 (2007).
[31]M. A. Rafiq, M. E. Costa, A. Tkach, and P. M. Vilarinho, Cryst. Growth Des. **15**, 1289 (2015).
[32]V. Shur and A. R. Akhmatkhanov, Philos. Trans. R. Soc. A **376**, 20170204 (2018).
[33]P. Gao, C. T. Nelson, J. R. Jokisaari, S.-H. Baek, C. W. Bark, Y. Zhang, E. Wang, D. G. Schlom, C.-B. Eom, and X. Pan, Nat. Commun. **2**, 591 (2011).
[34]Z. Chen, L. Hong, F. Wang, S. P. Ringer, L.-Q. Chen, H. Luo, and X. Liao, Phys. Rev. Lett. **118**, 017601 (2017).
[35]Z. Chen, Q. Huang, F. Wang, S. P. Ringer, H. Luo, and X. Liao, Appl. Phys. Lett. **112**, 152901 (2018).
[36]Q. Huang, J. Yang, Z. Chen, Y. Chen, M. J. Cabral, H. Luo, F. Li, S. Zhang, Y. Li, Z. Xie, H. Huang, Y.-W. Mai, S. P. Ringer, S. Liu, and X. Liao, ACS Appl. Mater. Interfaces **15**, 2313 (2023).
[37]B. J. Rodriguez, S. Jesse, A. P. Baddorf, T. Zhao, Y. H. Chu, R. Ramesh, E. A. Eliseev, A. N. Morozovska, and S. V. Kalinin, Nanotechnology **18**, 405701 (2007).

Supplementary Material

Voltage-driven ferroelectric domain dynamics in (K,Na)NbO_3 investigated by in situ transmission electron microscopy

Oana Condurache[a,b*], Goran Dražić[a,b,c] and Andreja Benčan[a,b]

[a] Electronic Ceramics Department, Jožef Stefan Institute, 1000 Ljubljana, Slovenia

[b] Jožef Stefan International Postgraduate School, 1000 Ljubljana, Slovenia

[c] Department of Materials Chemistry, National Institute of Chemistry, 1001 Ljubljana, Slovenia

*Corresponding author

Supplementary 1

A monoclinic symmetry was assigned to the $K_{0.5}Na_{0.5}NbO_3$ single crystal (KNN_{sc}) in our previous study (A. Benčan, E. Tchernychova, M. Godec, J. Fisher, and M. Kosec, Microsc. Microanal. **15**, 435 (2009)). The unit-cell parameters for the best refinement fit of the experimental X-ray diffraction pattern are:

$$\begin{cases} a_m = 4.0046\ \text{Å} \\ b_m = 3.9446\ \text{Å} \\ c_m = 4.0020\ \text{Å} \\ \alpha_m = \gamma_m = 90°,\ \beta_{m,} = 90.33° \end{cases}$$

The orthorhombic unit-cell parameters were derived from the monoclinic parameters as follows (G. Shirane, R. Newnham, and R. Pepinsky, Phys. Rev. 96, 581 (1954)):

$$\begin{cases} a_o = 2a_m \sin\dfrac{\beta_m}{2} \\ b_o = b_m \\ c_o = 2c_m \cos\dfrac{\beta_m}{2} \end{cases}$$

The selected-area electron diffraction (SAED) was simulated using CrystalMaker Software (version 10.7.2) together with SingleCrystal Software (Version 4.1.6). The *Bmm*2 orthorhombic structure was built in CrystalMaker using the following unit-cell parameters calculated from monoclinic metric:

$$\begin{cases} a_o = 5.6783\ \text{Å} \\ b_o = 3.9446\ \text{Å} \\ c_o = 5.6255\ \text{Å} \\ \alpha_o = \beta_o = \gamma_o = 90° \end{cases}$$

A SAED across a 90°-type domain wall (DW) in the $[100]_{pc}$ zone axis was simulated by superimposing the SAED from two equivalent orientations of the crystal structure where the polar axis is rotated by a 90° angle. The two equivalent orientations of the crystal structure correspond to Domain 1 (S.1 a)) and Domain 2 (S.1 b)). In this particular case the polar axis is in the plane of the viewing direction.

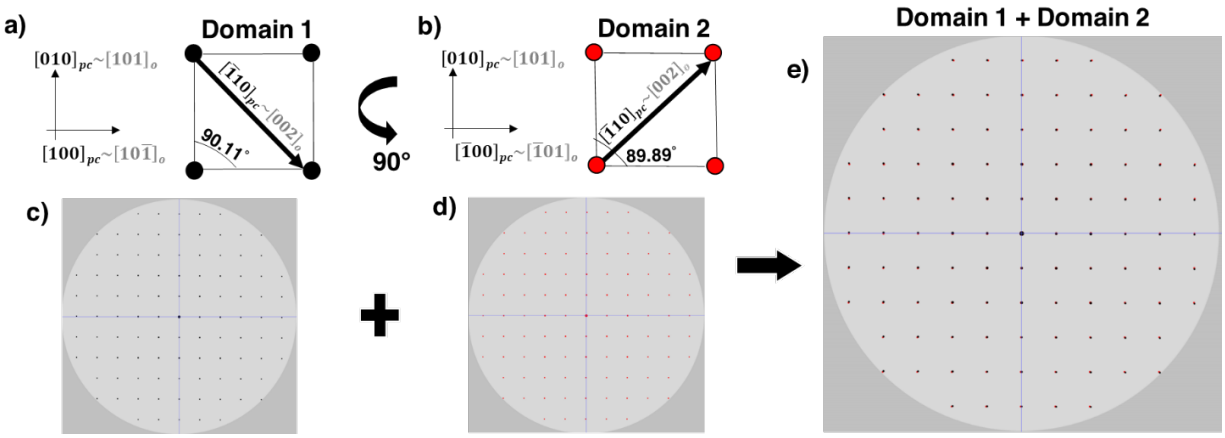

S.1 Crystal structure represented by one unit cell in a) Domain 1 and b) Domain 2. The polar axis is marked by a bold, black arrow. The crystallographic directions are shown in both pseudo-cubic (black) and orthorhombic (gray) notation. b) and d) the simulated SAED for Domain 1 and Domain 2, respectively. e) Superposition of b) and d) representing SAED on a 90° DW.

Supplementary 2

In situ biasing experimental procedure

A Protochips Fusion biasing/heating TEM holder has been used for the in situ STEM biasing experiments. The specimen is prepared by focused ion beam (FIB) (Helios Nanolab 650 with Ga ions source) on a capacitor-like FIB-optimized electrical E-chip with patterned electrodes (Figure S.2. a)).

The FIB specimen preparation follows the conventional lift-out lamella preparation route: deposition of Pt for surface protection by electrons/ions, lift-out and welding it with Pt between the E-chip electrodes (Figure S.2 a) and c)), thinning of the specimen by high voltage ion beam (30 kV) and cleaning of the specimen with low voltage ion beam (5 kV, 2kV, 1kV). The final specimen (Figure S.2. b)) has a thickness between 100-170 nm. The bottom of the specimen, which is more prone to Pt-redeposition, is cut to avoid leakage. In addition, the Pt-layer on top is cut to avoid short circuits (Figure S.2. c)).

All FIB parameters (current, voltage) and preparation steps are given in detail in: O. Condurache, G. Dražić, T. Rojac, H. Uršič, B. Dkhil, A. Bradeško, D. Damjanovic, and A. Benčan, Nano Lett. **23**, 750 (2023).

The holder is connected to a Keithley power supply. The distance between electrodes is by default 20 µm and the end values of the applied voltage are ±55V. An electrical DC voltage bias is applied with a 0.5V/s step and hold to a constant value while the STEM images are recorded. The experiment V(t) plot is shown in Figure S.2. d).

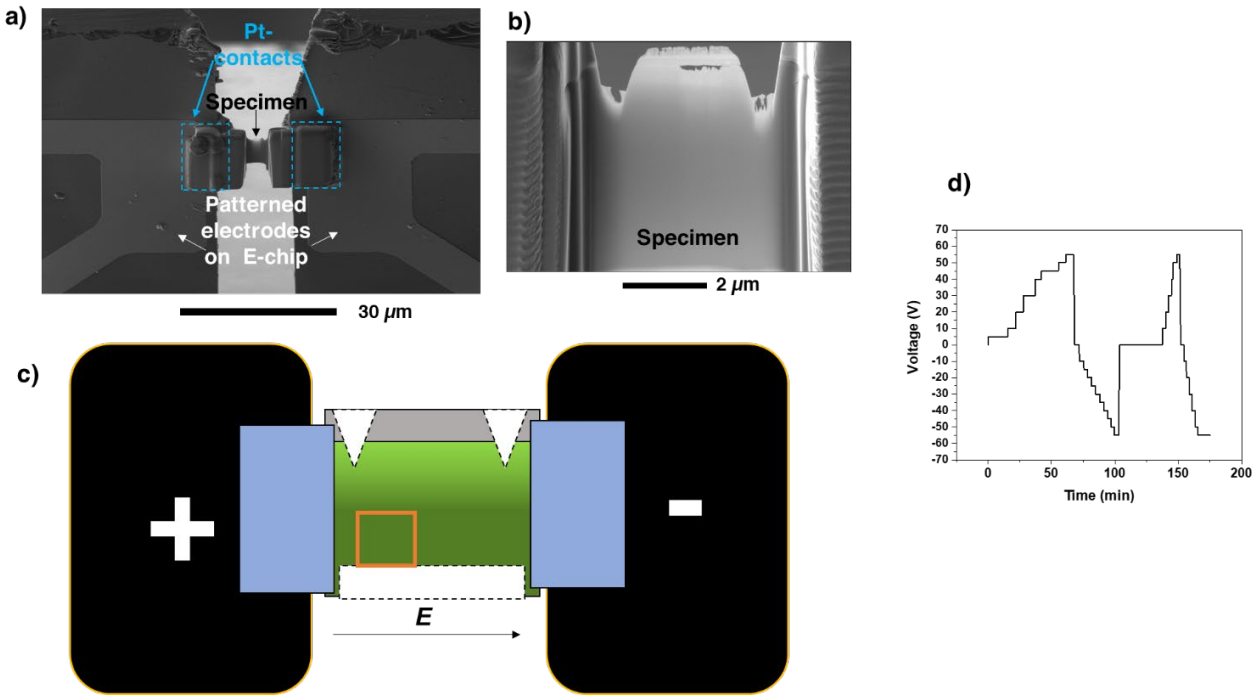

S.2. a) Scanning electron microscopy (SEM) image overview of a MEMS chip where the specimen is welded with Pt-contacts. b) SEM image of the specimen. c) Cartoon showing the specimen-MEMS chip system. Green represents the specimen, grey the Pt-deposited by FIB, blue the Pt-contacts and black the chip electrodes. The cuts are made on the bottom and top of the specimen (dotted line). The approximative area shown in the main manuscript is marked with orange rectangle. d) The voltage vs time dependence during the experiment.

Supplementary 3

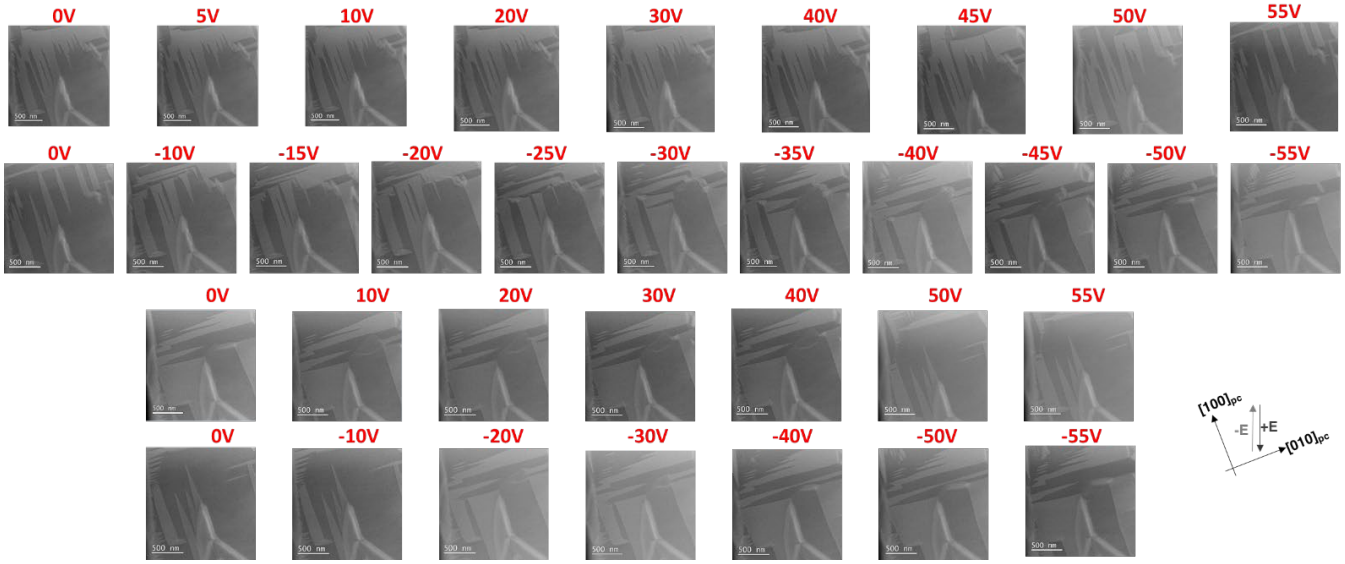

S.3.1 Original STEM-LAADF images in chronological sequence of the applied voltages

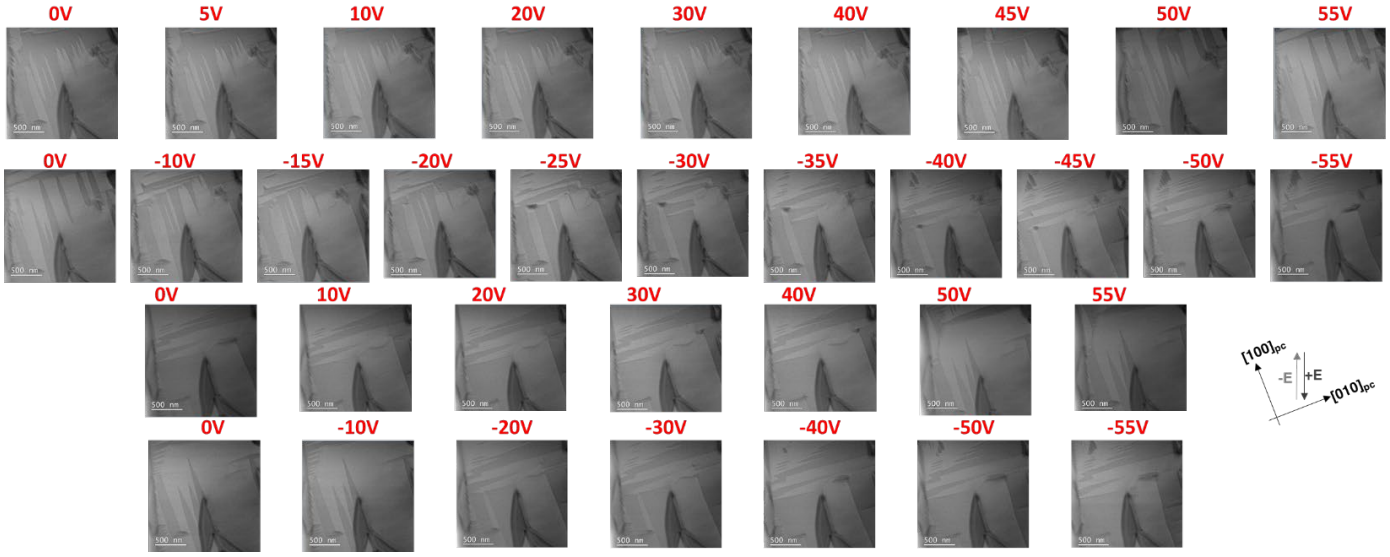

S.3.2 Original STEM-BF images in chronological sequence of applied voltages

Supplementary 4

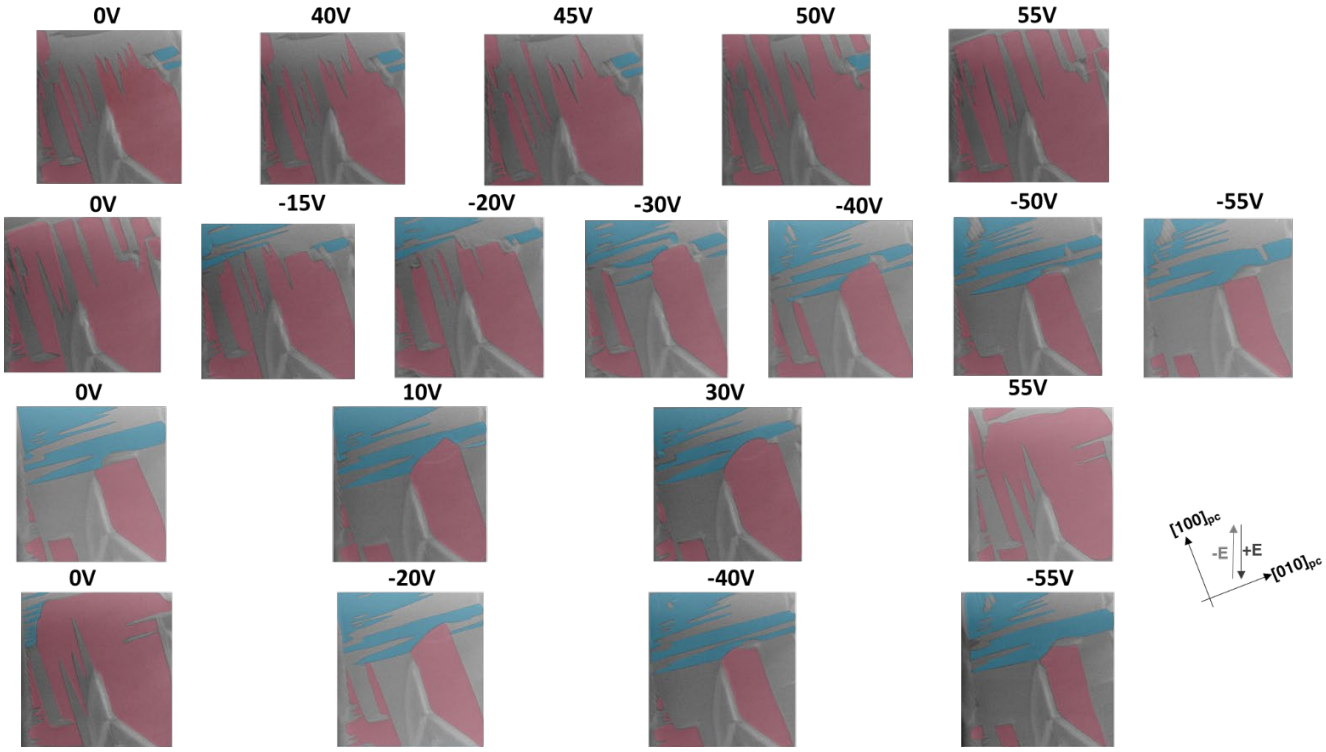

S.4. False-colored STEM-LAADF images in chronological sequence of applied voltages

The evaluation of the coverage area of each set of domains (red/blue) (presented in the main manuscript in Figure 3b) and Figure 5a)-b)) has been done by firstly drawing the contour for each domain using an imaging software (CorelDRAW x6) and further evaluating the relative area in ImageJ. The error bars expressed as the standard deviation (in Figure 3b) and Figure 5a)-b)) are evaluated according to the systematical error done when drawing the contours due to the resolution of the diffraction contrast.

Chapter 5

Summary and Conclusions

This work focuses on the ferroelectric DWs in lead-free perovskites ($BiFeO_3$ and $(K,Na)NbO_3$) in terms of structural characteristics and their dynamical response down to the atomic scale by (S)TEM and in-situ biasing (S)TEM.

5.1 Atomically Resolved Structure of Step-Like Uncharged and Charged Domain Walls in Polycrystalline $BiFeO_3$

The first study of the present work focuses on resolving the structure of charged/uncharged step-like DWs in polycrystalline $BiFeO_3$. Based on the results of this chapter, the following conclusions can be drawn:

- An atomic, step-like morphology was found in both uncharged and charged tail-to-tail $\{100\}_{pc}$-type DWs. Small steps (1-4 unit cells) or a larger, sharp rectangular step (~10 unit cells) were found.
- Regardless of their charged state, all the analyzed DWs have a comparable number of Bi vacancies. More of the Bi vacancies were found to segregate at the larger step.
- The strain (i.e., unit-cell distortion angle) perpendicular to the DW plane is always greater than the strain parallel to it.
- Uncharged DWs exhibiting a higher strain than the tail-to-tail charged one was associated with an intrinsic lattice mismatch according to simulated HAADF images. Moreover, the strain appeared to be more diffuse at the charged DWs and more concentrated in the center of the uncharged wall. This result confirms hypothesis 1.
- From a structural point of view, our results show that charged DWs are wider than the uncharged ones (~5 unit cells compared to ~10 unit cells), confirming previous reports [27] and hypothesis 1. A narrower and abrupt transition of the Fe-displacement vector across a DW could be associated with a higher and more concentrated strain.
- All the investigated DWs in the present study show a non-Ising behavior where the projected displacement vector (and consequently the projected polarization vector) changes both the magnitude and angle from one domain to the other.

5.2 Response of the Domain Walls in Bismuth Ferrite in a Subcoercive-Field Regime

In the second part, the response of a singular zigzag DW in a $BiFeO_3$ single crystal was probed at the atomic level in a subcoercive-field regime. Based on the results of this chapter, the following conclusions can be drawn:

- The domain structure of the $BiFeO_3$ single crystal is ordered and consists of lamellar domains, coupled to crystallographic defects (antiphase boundaries and dislocations) and 180° zigzag domains.
- The zigzag domains are more mobile than the lamellar domains, which did not respond within the voltage range used, probably due to pinning to the crystallographic defects. This result is in agreement with hypothesis 2, which predicted that the mobility of a DW depends on their type and morphology.
- Some areas switch faster than others, even if the type and morphology of the DWs were similar (180° zigzag DWs). This variation could be due to local variations in the free energy (i.e., different defects or strain fields). Often, the diffraction contrast corresponding to the 180° zigzag domains did not reflect long-range movement but it blurred, suggesting short-ranges changes in the structure and properties. Moreover, we concluded from this response that we are operating at electric fields below the coercive field.
- We further observed the local interactions between the mobile zigzag DWs and a low subcoercive electric field with atomic resolution.
- On the one hand, we monitored the movement of one neutral central segment of the zigzag wall. The DW movement determined from the Fe-displacement map is independent of the strain field marked by an enhanced diffraction contrast in BF images. One hypothesis is that defects with relatively low mobility segregate at the initial position of the DW (e.g., clusters of O vacancies).
- On the other hand, the apex of the zizgzag is pinned, but a lattice response is observed: the Fe-displacement (which is proportional to the polarization) changed the magnitude according to the direction of the electric field. The pinning of the apex may be related to a higher segregation of Bi and O vacancies. In addition, the apex bent its plane and we established that the atomic-scale implications of it are strain and Bi vacancy redistribution. These findings confirm the hypothesis 3, where it has been proposed that even at low fields (i.e., subcoercive field) various phenomena can occur at the wall level.

5.3 Voltage-Driven Ferroelectric Domain Dynamics in $(K,Na)NbO_3$ Investigated by In-Situ Transmission Electron Microscopy

In the last part the domain dynamics in a $(K,Na)NbO_3$ single crystal was probed. Based on the results of this chapter, the following conclusions can be drawn:

- In a given $[100]_{pc}$ zone axis the domain structure of the (K,Na)NbO_3 single crystal consists of: needlelike domains, irregular lamellar domains and non-edge-on domains.
- When the specimen is prepared on the in-situ biasing chip with Pt-electrodes on the side, the needlelike domains dominate along the non-edge on domains, and their interaction was further probed during the switching process in a representative region. The needlelike domains were classified to present 90º DWs based on a comparison between experimental and simulated SAED patterns.
- When a bias voltage was applied, the needles responded while the non-edge-on domains did not. The formulated hypothesis is that polarization in the needlelike domains favors the electric field orientation. Another viable explanation could be that the non-edge-on domains are pinned on crystallographic defects or segregation of the point-charge defects. In the present analysis, we did not prove the presence of defects.
- In one polarity, the growth of needlelike domains occurred as the forward motion of the tip until it encountered an obstacle (e.g., another DW), whereupon coalescence and lateral growth occurred. On the other polarity, needles initially grow in a perpendicular direction, but the growth stopped at a certain threshold voltage, whereupon, the domain splits into fine needles and nanodomains. Our experimental results indicated that this was a consequence of stress build-up.
- Pinning was observed between orthogonal needles. Direct observation of the emergent strain was probed when two orthogonal needles meet.
- The immobile non-edge-on DWs played an active role in the switching process by pinning the surrounding area, regardless of its polarity, thus, acting as randomly bound defects. Meantime, the edge of the specimen promoted nucleation of new domains. These results support hypothesis 4.

5.4 Future Work and Perspectives

Here, we summarize future work that may be relevant for developments in the field of atomically resolved transmission electron microscopy and the in-situ voltage-driven dynamic response of domain walls in lead-free ferroelectrics:

- Addressing the specimen thickness in relation to the switching dynamics in in-situ biasing STEM experiments.
- Application of advanced electron microscopy techniques, such as 4DSTEM-differential phase contrast, to directly determine the electrostatic fields. This will allow direct and unambiguous determination of the polar directions and domain structure; in addition, the bound charge distribution at the DW location and its evolution with the electric fields could also be probed.
- In the present study, the time dependence of the switching process has not been studied. Time relaxation studies could help address applicative potential for future devices based on the ferroelectric switching.

References

[1] A. J. Bell and O. Deubzer, "Lead-free piezoelectrics—The environmental and regulatory issues," *MRS Bulletin*, vol. 43, no. 8, pp. 581–587, 2018.

[2] Y. Saito, H. Takao, T. Tani, T. Nonoyama, K. Takatori, T. Homma, T. Nagaya, and M. Nakamura, "Lead-free piezoceramics," *Nature Materials*, vol. 432, pp. 84-87, 2004.

[3] T. Rojac, A. Bencan, B. Malic, G. Tutuncu, J.L. Jones, J.E. Daniels, and D. Damjanovic, "$BiFeO_3$ Ceramics: Processing, Electrical, and Electromechanical Properties," *J. Am. Ceram. Soc.*, vol. 97, no. 7, pp. 1993–2011, 2014.

[4] G.F. Nataf, M. Guennou, J.M. Gregg, D. Meier, J. Hlinka, E.K.H. Salje, and J. Kreisel, "Domain-wall engineering and topological defects in ferroelectric and ferroelastic materials," *Nat. Rev. Phys.*, vol. 2, no. 11, pp. 634–648, 2020.

[5] D.A. Ochoa, G. Esteves, T. Iamsasri, F. Rubio-Marcos, J.F. Fernández, J.E. García, and J.L. Jones, "Extensive domain wall contribution to strain in a (K,Na)NbO_3-based lead-free piezoceramics quantified from high energy X-ray diffraction," *Journal of the European Ceramic Society*, vol. 36, no. 10, pp. 2489–2494, 2016.

[6] J. Gonnissen, D. Batuk, G.F. Nataf, L. Jones, A.M. Abakumov, S. Van Aert, D. Schryvers, and E.K.H. Salje, "Direct Observation of Ferroelectric Domain Walls in $LiNbO_3$: Wall-Meanders, Kinks, and Local Electric Charges," *Adv. Funct. Mater.*, vol. 26, no. 42, pp. 7599–7604, 2016.

[7] W.-Y. Wang, Y.-L. Tang, Y.-L. Zhu, Y.-B. Xu, Y. Liu, Y.-J. Wang, S. Jagadeesh, and X.-L. Ma, "Atomic Level 1D Structural Modulations at the Negatively Charged Domain Walls in $BiFeO_3$ Films," *Adv. Mater. Interfaces*, vol. 2, no. 9, p. 1500024, 2015.

[8] T. Rojac, A. Bencan, G. Drazic, N. Sakamoto, H. Ursic, B. Jancar, G. Tavcar, M. Makarovic, J. Walker, B. Malic, and D. Damjanovic, "Domain-wall conduction in ferroelectric $BiFeO_3$ controlled by accumulation of charged defects," *Nature Materials*, vol. 16, no. 3, pp. 322–327, 2017.

[9] P. Gao, C.T. Nelson, J.R. Jokisaari, S.-H. Baek, C.W. Bark, Y. Zhang, E. Wang, D.G. Schlom, C.-B. Eom and X. Pan, "Revealing the role of defects in ferroelectric switching with atomic resolution," *Nat. Commun.*, vol. 2, no. 1, p. 591, 2011.

[10] P. Gao, J. Britson, J.R. Jokisaari, C.T. Nelson, S.-H. Baek, Y. Wang, C.-B. Eom, L.-Q. Chen, and X. Pan, "Atomic-scale mechanisms of ferroelastic domain-wall-mediated ferroelectric switching," *Nat. Commun.*, vol. 4, no. 1, p. 2791, 2013.

[11] D. Damjanovic, "Ferroelectric, dielectric and piezoelectric properties of ferroelectric thin films and ceramics," *Rep. Prog. Phys.*, vol. 61, no. 9, pp. 1267–1324, 1998.

[12] R. E. Cohen, "Origin of ferroelectricity in perovskite oxides," *Nature*, vol. 358, pp. 136-138, 1992.

[13] G. Catalan, J. Seidel, R. Ramesh, and J. F. Scott, "Domain wall nanoelectronics," *Rev. Mod. Phys.*, vol. 84, no. 1, pp. 119–156, 2012.

[14] B. Dupé, I. C. Infante, G. Geneste, P.-E. Janolin, M. Bibes, A. Barthélémy, S. Lisenkov, L. Bellaiche, S. Ravy, and B. Dkhil, "Competing phases in $BiFeO_3$ thin films under compressive epitaxial strain," *Phys. Rev. B*, vol. 81, no. 14, p. 144128, 2010.

[15] A. S. Sidorkin, Domain structure in ferroelectrics and related materials. Cambridge: Cambridge International Science Publishing, 2006.

[16] C. Kittel, "Theory of the Structure of Ferromagnetic Domains in Films and Small Particles," *Phys. Rev.*, vol. 70, no. 11–12, pp. 965–971, 1946.

[17] T. Mitsui and J. Furuichi, "Domain Structure of Rochelle Salt and KH_2PO_4," *Phys. Rev.*, vol. 90, no. 2, pp. 193–202, 1953.

[18] A. Schilling, T. B. Adams, R. M. Bowman, J. M. Gregg, G. Catalan, and J. F. Scott, "Scaling of domain periodicity with thickness measured in $BaTiO_3$ single crystal lamellae and comparison with other ferroics," *Phys. Rev. B*, vol. 74, no. 2, pp. 024115, 2006.

[19] A. Saxena and A. Planes, Eds., Mesoscopic Phenomena in Multifunctional Materials: Synthesis, Characterization, Modeling and Applications, Springer Series in Materials Science, vol. 198. Berlin, Heidelberg: Springer Berlin Heidelberg, 2014.

[20] M. Li, X. Li, Y. Li, H.-J. Liu, Y.-H. Chu, and P. Gao, "Atomic-environment-dependent thickness of ferroelastic domain walls near dislocations," *Acta Materialia*, vol. 188, pp. 635–640, 2020.

[21] S. Choudhury, Y. Li, N. Odagawa, A. Vasudevarao, L. Tian, P. Capek, V. Dierolf, A. N. Morozovska, E. A. Eliseev, S. Kalinin, Y. Cho, L.-q. Chen, and V. Gopalan, "The influence of 180° ferroelectric domain wall width on the threshold field for wall motion," *Journal of Applied Physics*, vol. 104, no. 8, p. 084107, 2008.

[22] P. V. Yudin, M. Y. Gureev, T. Sluka, A. K. Tagantsev, and N. Setter, "Anomalously thick domain walls in ferroelectrics," *Phys. Rev. B*, vol. 91, no. 6, p. 060102, 2015.

[23] W. T. Lee, E. K. H. Salje, and U. Bismayer, "Influence of point defects on the distribution of twin wall widths," *Phys. Rev. B*, vol. 72, no. 10, p. 104116, 2005.

[24] A. Bencan, G. Drazic, H. Ursic, M. Makarovic, M. Komelj, and T. Rojac, "Domain-wall pinning and defect ordering in $BiFeO_3$ probed on the atomic and nanoscale," *Nat. Commun.*, vol. 11, no. 1, p. 1762, 2020.

[25] A. K. Tagantsev, K. Shapovalov, and P. V. Yudin, "Thick domain walls in non-magnetic ferroics," *Ferroelectrics*, vol. 503, no. 1, pp. 163–179, 2016.

[26] B. Meyer and D. Vanderbilt, "*Ab initio* study of ferroelectric domain walls in $PbTiO_3$," *Phys. Rev. B*, vol. 65, no. 10, p. 104111, 2002.

[27] P. S. Bednyakov, B. I. Sturman, T. Sluka, A. K. Tagantsev, and P. V. Yudin, "Physics and applications of charged domain walls," *npj Comput. Mater.*, vol. 4, no. 1, p. 65, 2018.

[28] O. Condurache, G. Dražić, T. Rojac, H. Uršič, B. Dkhil, A. Bradeško, D. Damjanovic, and A. Benčan, "Atomic-Level Response of the Domain Walls in Bismuth Ferrite in a Subcoercive-Field Regime," *Nano Lett.*, vol. 23, no. 2, pp. 750–756, 2023.

[29] J. Ricote, R. W. Whatmore, and D. J. Barber, "Studies of the ferroelectric domain configuration and polarization of rhombohedral PZT ceramics," *J. Phys.: Condens. Matter*, vol. 12, no. 3, pp. 323–337, 2000.

[30] J. Zhang, Y.-J. Wang, J. Liu, J. Xu, D. Wang, L. Wang, X.-L. Ma, C.-L. Jia, and L. Bellaiche, "Origin of sawtooth domain walls in ferroelectrics," *Phys. Rev. B*, vol. 101, no. 6, p. 060103, 2020.

[31] M. Y. Gureev, A. K. Tagantsev, and N. Setter, "Head-to-head and tail-to-tail 180° domain walls in an isolated ferroelectric," *Phys. Rev. B*, vol. 83, no. 18, p. 184104, 2011.

[32] C.-L. Jia, S.-B. Mi, K. Urban, I. Vrejoiu, M. Alexe, and D. Hesse, "Atomic-scale study of electric dipoles near charged and uncharged domain walls in ferroelectric films," *Nature Materials*, vol. 7, no. 1, pp. 57–61, 2008.

[33] O. Condurache, G. Dražić, N. Sakamoto, T. Rojac, and A. Benčan, "Atomically resolved structure of step-like uncharged and charged domain walls in polycrystalline $BiFeO_3$," *Journal of Applied Physics*, vol. 129, no. 5, p. 054102, 2021.

[34] S. Mantri and J. Daniels, "Domain walls in ferroelectrics," *J Am Ceram Soc*, vol. 104, no. 4, pp. 1619–1632, 2021.

[35] P. Marton, I. Rychetsky, and J. Hlinka, "Domain walls of ferroelectric $BaTiO_3$ within the Ginzburg-Landau-Devonshire phenomenological model," *Phys. Rev. B*, vol. 81, no. 14, p. 144125, 2010.

[36] S. Mantri and J. E. Daniels, "Ferroelectric Domain Continuity Over Grain Boundaries for Tetragonal, Orthorhombic, and Rhombohedral Crystal Symmetries," *IEEE Trans. Ultrason., Ferroelect., Freq. Contr.*, vol. 65, no. 9, pp. 1517–1524, 2018.

[37] G. Catalan and J. F. Scott, "Physics and Applications of Bismuth Ferrite," *Adv. Mater.*, vol. 21, no. 24, pp. 2463–2485, 2009.

[38] J. Hirohashi, K. Yamada, H. Kamio, M. Uchida, and S. Shichijyo, "Control of specific domain structure in $KNbO_3$ single crystals by differential vector poling method," *Journal of Applied Physics*, vol. 98, no. 3, p. 034107, 2005.

[39] E. Wiesendanger, "Domain structures in orthorhombic $KNbO_3$ and characterisation of single domain crystals," *Czech J. Phys.*, vol. 23, no. 1, pp. 91–99, 1973.

[40] M. Bah, N. Alyabyeva, R. Retoux, F. Giovannelli, M. Zaghrioui, A. Ruyter, F. Delormea and I. Monot-Laffez, "Investigation of the domain structure and hierarchy in potassium–sodium niobate lead-free piezoelectric single crystals," *RSC Adv.*, vol. 6, no. 54, pp. 49060–49067, 2016.

[41] A. Lubk, M. D. Rossell, J. Seidel, Q. He, S. Y. Yang, Y. H. Chu, R. Ramesh, M. J. Hytch, and E. Snoeck, "Evidence of Sharp and Diffuse Domain Walls in $BiFeO_3$ by Means of Unit-Cell-Wise Strain and Polarization Maps Obtained with High Resolution Scanning Transmission Electron Microscopy," *Phys. Rev. Lett.*, vol. 109, no. 4, p. 047601, 2012.

[42] J. Guyonnet, *Ferroelectric Domain Walls: Statics, Dynamics, and Functionalities Revealed by Atomic Force Microscopy*, in Springer Theses, Cham: Springer International Publishing, 2014.

[43] R. C. Miller and G. Weinreich, "Mechanism for the Sidewise Motion of 180° Domain Walls in Barium Titanate," *Phys. Rev.*, vol. 117, no. 6, pp. 1460–1466, 1960.

[44] D. Lee, R. K. Behera, P. Wu, H. Xu, Y. L. Li, S. B. Sinnott, S. R. Phillpot, L. Q. Chen, and V. Gopalan, "Mixed Bloch-Néel-Ising character of 180° ferroelectric domain walls," *Phys. Rev. B*, vol. 80, no. 6, p. 060102, 2009.

[45] J. C. Wojdeł and J. Íñiguez, "Ferroelectric Transitions at Ferroelectric Domain Walls Found from First Principles," *Phys. Rev. Lett.*, vol. 112, no. 24, p. 247603, 2014.

[46] X.-K. Wei, C.-L. Jia, T. Sluka, B.-X. Wang, Z.-G. Ye, and N. Setter, "Néel-like domain walls in ferroelectric Pb(Zr,Ti)O_3 single crystals," *Nat. Commun.*, vol. 7, no. 1, p. 12385, 2016.

[47] S. Cherifi-Hertel, H. Bulou, R. Hertel, G. Taupier, K. D. (H) Dorkenoo, C. Andreas, J. Guyonnet, I. Gaponenko, Katia Gallo, and P. Paruch, "Non-Ising and chiral ferroelectric domain walls revealed by nonlinear optical microscopy," *Nat Commun*, vol. 8, no. 1, p. 15768, 2017.

[48] L. Liu, K. Xu, Q. Li, Y. Huang, L. Shu, Y.-Y.-S. Cheng, S. Zhang, J. Luo, J. Zhu, and J.-F. Li, "Ultrathin Non-Ising Charged Domain Walls Confined in $BiFeO_3$ Nanocrystals,"*Adv. Funct. Mater.*, vol. 32, no. 46, p. 2207730, 2022.

[49] Y. Gu, M. Li, A. N. Morozovska, Y. Wang, E. A. Eliseev, and L.-Q. Chen, "Non-Ising Character of a Ferroelectric Wall Arises from a Flexoelectric Effect", arXiv:1401.0194 [cond-mat.mtrl-sci] [Accessed 30.05.2023].

[50] L. Jin, F. Li, and S. Zhang, "Decoding the Fingerprint of Ferroelectric Loops: Comprehension of the Material Properties and Structures," *J. Am. Ceram. Soc.*, vol. 97, no. 1, pp. 1–27, 2014.

[51] R. Ignatans, "Ferroelectric Effects Probed by in situ Transmission Electron Microscopy," École Polytechnique Fédérale de Lausanne, Lausanne, Switzerland, 2022.

[52] J. F. Scott and C. A. Paz de Araujo, "Ferroelectric Memories," *Science*, vol. 246., no. 4936, pp. 1400-1405, 1989.

[53] M. Avrami, "Kinetics of Phase Change. II Transformation-Time Relations for Random Distribution of Nuclei," *The Journal of Chemical Physics*, vol. 8, no. 2, pp. 212–224, 1940.

[54] A. K. Tagantsev, I. Stolichnov, N. Setter, J. S. Cross, and M. Tsukada, "Non-Kolmogorov-Avrami switching kinetics in ferroelectric thin films," *Phys. Rev. B*, vol. 66, no. 21, p. 214109, 2002.

[55] D. Pantel, Y.-H. Chu, L. W. Martin, R. Ramesh, D. Hesse, and M. Alexe, "Switching kinetics in epitaxial $BiFeO_3$ thin films," *Journal of Applied Physics*, vol. 107, no. 8, p. 084111, 2010.

[56] D. Meier, "Functional domain walls in multiferroics," *J. Phys.: Condens. Matter*, vol. 27, no. 46, p. 463003, 2015.

[57] A. K. Tagantsev, L. E. Cross, and J. Fousek, *Domains in Ferroic Crystals and Thin Films*, New York, NY: Springer New York, 2010.

[58] D. B. Williams and C. B. Carter, *Transmission electron microscopy: a textbook for materials science*, 2nd ed. New York: Springer, 2008.

[59] S. J. Pennycook and P. D. Nellist, Eds., *Scanning Transmission Electron Microscopy*, New York, NY: Springer New York, 2011.

[60] P. Deb, M. C. Cao, Y. Han, M. E. Holtz, S. Xiea, J. Park, R. Hovden, D. A. Muller, "Imaging Polarity in Two Dimensional Materials by Breaking Friedel's Law," *Ultramicroscopy*, vol. 215, p. 113019, 2020.

[61] I. MacLaren and Q. M. Ramasse, "Aberration-corrected scanning transmission electron microscopy for atomic-resolution studies of functional oxides," *International Materials Reviews*, vol. 59, no. 3, pp. 115–131, 2014.

[62] A. Bencan, E. Oveisi, S. Hashemizadeh, V. K. Veerapandiyan, T. Hoshina, T. Rojac, M. Deluca, G. Drazic, and D. Damjanovic, "Atomic scale symmetry and polar nanoclusters in the paraelectric phase of ferroelectric materials," *Nat. Commun.*, vol. 12, no. 1, p. 3509, 2021.

[63] P. J. Phillips, M. De Graef, L. Kovarik, A. Agrawal, W. Windl, and M. J. Mills, "Atomic-resolution defect contrast in low angle annular dark-field STEM," *Ultramicroscopy*, vol. 116, pp. 47–55, 2012.

[64] T. Rojac, A. Bencan, G. Drazic, M. Kosec, and D. Damjanovic, "Piezoelectric nonlinearity and frequency dispersion of the direct piezoelectric response of $BiFeO_3$ ceramics," *Journal of Applied Physics*, vol. 112, no. 6, p. 064114, 2012.

[65] J.-F. Li, K. Wang, F.-Y. Zhu, L.-Q. Cheng, and F.-Z. Yao, "(K,Na)NbO_3 -Based Lead-Free Piezoceramics: Fundamental Aspects, Processing Technologies, and Remaining Challenges," *J. Am. Ceram. Soc.*, vol. 96, no. 12, pp. 3677–3696, 2013.

[66] M. Otonicar, M. Dragomir, and T. Rojac, "Dynamics of domain walls in ferroelectrics and relaxors," *J Am Ceram Soc.*, vol. 105, no. 11, pp. 6479–6507, 2022.

[67] G. Botton, *Analytical Electron Microscopy*, in Hawkes, P.W., Spence, J.C.H. (eds) Science of Microscopy, New York, NY: Springer New York, 2007.

[68] "Comparison between EDS and EELS & Periodic Table for EDS and EELS Analysis. Practical Electron Microscopy and Database," [Online]. Available: http://www.globalsino.com/EM/page4794.html [Date accessed: 5.05.2023].

[69] T. Malis, S. C. Cheng, and R. F. Egerton, "EELS log-ratio technique for specimen-thickness measurement in the TEM," *J. Elec. Microsc. Tech.*, vol. 8, no. 2, pp. 193–200, 1988.

[70] L. Li, J. R. Jokisaari, and X. Pan, "*In situ* electron microscopy of ferroelectric domains," *MRS Bull.*, vol. 40, no. 1, pp. 53–61, 2015.

[71] X. Y. Qi, H. H. Liu, and X. F. Duan, "*In situ* transmission electron microscopy study of electric-field-induced 90° domain switching in $BaTiO_3$ single crystals," *Appl. Phys. Lett.*, vol. 89, no. 9, p. 092908, 2006.

[72] E. Snoeck, L. Normand, A. Thorel, and C. Roucau, "Electron microscopy study of ferroelastic and ferroelectric domain wall motions induced by the *in situ* application of an electric field in $BaTiO_3$," *Phase Transitions*, vol. 46, no. 2, pp. 77–88, 1994.

[73] X. Tan, H. He, and J.-K. Shang, "In situ Transmission Electron Microscopy Studies of Electric-field-induced Phenomena in Ferroelectrics," *J. Mater. Res.*, vol. 20, no. 7, pp. 1641–1653, 2005.

[74] Z. Xu, X. Tan, P. Han, and J. K. Shang, "In situ transmission electron microscopy study of electric-field-induced microcracking in single crystal $Pb(Mg_{1/3}Nb_{2/3})O_3$ – $PbTiO_3$", vol. 76, no. 25, pp. 3732–3734, 2000.

[75] M. Zakhozheva, L. A. Schmitt, M. Acosta, W. Jo, J. Rödel, and H.-J. Kleebe, "*In situ* electric field induced domain evolution in $Ba(Zr_{0.2}Ti_{0.8})O_3$ -0.3$(Ba_{0.7}Ca_{0.3})TiO_3$ ferroelectrics," *Appl. Phys. Lett.*, vol. 105, no. 11, p. 112904, 2014.

[76] C. T. Nelson, P. Gao, J. R. Jokisaari, C. Heikes, C. Adamo, A. Melville, S.-H. Baek, C. M. Folkman, B. Winchester, Y. Gu, Y. Liu, K. Zhang, E. Wang, J. Li, L.-Q. Chen, C.-B. Eom, D. G. Schlom, and X. Pan, "Domain Dynamics During Ferroelectric Switching," *Science*, vol. 334, no. 6058, pp. 968–971, 2011.

[77] P. Gao, J. Britson, C. T. Nelson, J. R. Jokisaari, C. Duan, M. Trassin, S.-H. Baek, H. Guo, L. Li, Y. Wang, Y.-H. Chu, A. M. Minor, C.-B. Eom, R. Ramesh, L.-Q. Chen, and X. Pan, "Ferroelastic domain switching dynamics under electrical and mechanical excitations," *Nat Commun*, vol. 5, no. 1, p. 3801, 2014.

[78] M.-G. Han *et al.*, "Interface-induced nonswitchable domains in ferroelectric thin films," *Nat Commun*, vol. 5, no. 1, p. 4693, 2014.

[79] S. Vijayan, J. R. Jinschek, S. Kujawa, J. Greiser, and M. Aindow, "Focused Ion Beam Preparation of Specimens for Micro-Electro-Mechanical System-based Transmission Electron Microscopy Heating Experiments," *Microsc Microanal*, vol. 23, no. 4, pp. 708–716, 2017.

[80] T. Matsumoto and M. Okamoto, "Effects of electron irradiation on the ferroelectric 180° in-plane nanostripe domain structure in a thin film prepared from a bulk single crystal of $BaTiO_3$ by focused ion beam," *J. Appl. Phys.*, vol. 109, no. 1, p. 014104, 2011.

[81] J. L. Hart, S. Liu, A. C. Lang, A. Hubert, A. Zukauskas, C. Canalias, R. Beanland, A. M. Rappe, M. Arredondo, and M. L. Taheri, "Electron-beam-induced ferroelectric domain behavior in the transmission electron microscope: Toward deterministic domain patterning," *Phys. Rev. B*, vol. 94, no. 17, p. 174104, 2016.

[82] R. Ahluwalia, N. Ng, A. Schilling, R. G. P. McQuaid, D. M. Evans, J. M. Gregg, D. J. Srolovitz, and J. F. Scott, "Manipulating Ferroelectric Domains in Nanostructures Under Electron Beams," *Phys. Rev. Lett.*, vol. 111, no. 16, p. 165702, 2013.

[83] "Protochips. Fusion." [Online]. Available: https://www.protochips.com/products/fusion/, [Accessed 30.05.2023].

[84] S. Jesse, B. J. Rodriguez, S. Choudhury, A. P. Baddorf, I. Vrejoiu, D. Hesse, M. Alexe, E. A. Eliseev, A. N. Morozovska, J. Zhang, L.-Q. Chen, and S. V. Kalinin, "Direct imaging of the spatial and energy distribution of nucleation centres in ferroelectric materials," *Nature Mater*, vol. 7, no. 3, pp. 209–215, 2008.

Bibliography

Journal Articles Related to the Thesis

O. Condurache, G. Dražić, N. Sakamoto, T. Rojac and A. Benčan, "Atomically resolved structure of step-like uncharged and charged domain walls in polycrystalline $BiFeO_3$," *Journal of Applied Physics,* vol. 129, pp. 054102, 2021.

O. Condurache, G. Dražić, T. Rojac, H. Uršič, B. Dkhil, A. Bradeško, D. Damjanovic and A. Benčan, "Atomic-Level Response of the Domain Walls in Bismuth Ferrite in a Subcoercive-Field Regime, " *Nano Letters*, vol. 23, no. 2, pp. 750–756, 2023.

O. Condurache, G. Dražić and A. Benčan, "Voltage-driven ferroelectric domain dynamics in (K,Na)NbO_3 investigated by in situ transmission electron microscopy, " *Applied Physics Letters*, vol. 122, pp. 202902, 2023.

Awards

- 3rd place in the Young Ceramist Network Pitch Contest, June 2021, Virtual, Pitch presentation title: *Domain walls*
- 3rd place at the Student Paper Contest, 27th Annual Meeting of the Slovenian Chemical Society, September 2021, Portorose, Slovenia, Presentation title: *Static and dynamic study of domain walls in lead-free ferroelectrics*
- Student Scholar Award, Microscopy and Microanalysis, August 2022, Portland, Oregon, Presentation title: *Monitoring bismuth ferrite domain walls behavior under electric field with atomic resolution by in situ scanning transmission electron microscopy.*

Research Visits

- University A.I. Cuza, Faculty of Physics, Department of Dielectric, Ferroelectric and Multiferroic Materials, Research topic: *Functional characterisation of potassium sodium niobate-based and bismuth ferrite-based ceramics*, 2nd -23rd of December 2019, Iasi, Romania.
- University of Oxford, Department of Materials, Research topic: *Characterization of Ferroelectric Domain Walls by 4DSTEM*, 14th -23rd of May 2022, Oxford, United Kingdom.

Workshops Attendance

- Protochips In Situ Academy, September 2019, Berlin, Germany,
- YCN Pitch Me Your Idea!, Young Ceramic Network, June 2021, Virtual Workshop Contest

- AdSTEM 2023 - European School on 4D STEM imaging, May 2023, Piran, Slovenia

Other Scientific Articles

O. Condurache, K. Radan, U. Prah, M. Otoničar, B. Kmet, G. Kapun, G. Dražić, B. Malič and A. Benčan, "Heterogeneity challenges in multiple-element-modified lead-free piezoelectric ceramics," *Materials*, vol. 12, no. 24, pp. 4049, 2019

P. Cataldi, O. Condurache, D. Spirito, R. Krahne, I. S. Bayer, A. Athanassiou and G. Perotto. "Keratin-Graphene nanocomposite : transformation of waste wool in electronic device," *ACS sustainable Chemistry & Engineering*, vol. 7, no. 14, pp. 12544-12551, 2019

G. Canu, G. Bottaro, M. T. Buscaglia, C. Costa, O. Condurache, L. Curecheriu, L. Mitoseriu and V. Buscaglia. "Ferroelectric order driven Eu^{3+} photoluminescence in $BaZr_xTi_{1-x}O_3$ perovskite," *Scientific Reports*, vol. 9, no. 6441, 2020

J. Walker, A. Mirjanić, U. Prah, M. Šadl, O. Condurache, A. Benčan, T. Rojac, M. Grigoras and H. Uršič, "Magnetic contributions in multiferroic gadolinium modified bismuth ferrite ceramics," *Scripta Materialia*, vol. 188, pp. 233-237, 2020.

T. Schenk, A. Benčan, G. Dražić, O. Condurache, N. Valle, B. El Adib, N. Aruchamy, T. Granzow, E. Defay and S. Glinšek. "Enhancement of ferroelectricity and orientation in solution-derived hafnia thin films through heterogeneous grain nucleation," *Applied Physics Letters*, vol. 118, no. 16, pp. 162902, 2021.

V. A. Lukacs, G. Caruntu, O. Condurache, C. E. Ciomaga, L. P. Curecheriu, L. Padurariu, M. Ignat, M. Airimioaei, G. Stoian, A. Rotaru and L. Mitoseriu, "Preparation and properties of porous $BaTiO_3$ nanostructured ceramics produced from cuboidal nanocrystals," *Ceramics International*, vol. 47, no. 13, pp. 18105, 2021.

M. Sadl, O. Condurache, A. Benčan, M. Dragomir, U. Prah, B. Malič, M. Deluca, U. Eckstein, D. Hausmann, N. H. Khansur, K. G. Webber and H. Uršič, "Energy-storage-efficient $0.9Pb(Mg_{1/3}Nb_{2/3})O_3$–$0.1PbTiO_3$ thick films integrated directly onto stainless steel," *Acta Materialia*, vol. 221, pp. 117403, 2021.

A. Blázquez Martínez, N. Godard, N. Aruchamy, C. Milesi-Brault, O. Condurache, A. Benčan, S. Glinšek and T. Granzow. "Solution-processed $BiFeO_3$ thin films with low leakage current," *Journal of the European Ceramic Society.* 2021, vol. 41, no. 13, pp. 6449, 2021.

Invited Lecture at Foreign Universities

O. Condurache, H. Uršič, M. Sadl, K. Radan, U. Prah, M. Otoničar, B. Kmet, G. Dražić, B. Malič, A. Benčan, "Studies of different ceramic systems by means of electron microscopy techniques" Iasi, Romania: Laboratory for Dielectrics, Ferroelectrics and Multiferroics, Faculty of Physics, University “A.I. Cuza”, 2019.

Conference Contributions – Abstracts (Invited Lecture)

A. Benčan, G. Dražić, H. Uršič, M. Makarovič, O. Condurache, M. Komelj, D. Damjanović, T. Rojac, "Quantitative scanning transmission electron microscopy of lead-free piezoelectrics," in PINTAR, *Book of abstracts of the 26th Annual Meeting of the Slovenian Chemical Society,* Portorose, Slovenia: Slovensko kemijsko društvo, 2020.

A. Benčan, O. Condurache, G. Dražić, H. Uršič, D. Damjanović and T. Rojac, "Quantitative scanning transmission electron microscopy of local structures in lead-free piezoelectrics," in *QUORUM-2, the on-line conference on oxide electronics*, 2020.

B. Malič, K. Radan, O. Condurache, A. Benčan, M. Dragomir, T. Gindel and M. Deluca, "Tracing chemical heterogeneity across scales in alkali niobate based lead-free piezoelectric ceramics and its influence on functional properties," in *IEEE IFCS 2020 ISAF 2020 Virtual Conference,* Keystone, Colorado*:* joint Conference of the IEEE International Symposium on Applications of Ferroelectrics, USA, 2020.

A. Benčan, O. Condurache, G. Dražić, H. Uršič, D. Damjanović and T. Rojac, "Atomic-level-structural analysis of different crystal entities in lead-free Piezoelectrics," in *IEEE ISAF 2021 joint ISAF ISIF-PMF virtual Conference, IEEE International Symposium on Applications of Ferroelectric (ISAF), International Symposium on Integrated Functionalities (ISIF), Piezoresponse Force Microscopy Workshop (PFM),* Sydney, Australia: Institute of Electrical and Electronics Engineers (IEEE), 2021.

A. Benčan, O. Condurache, H. Uršič, T. Rojac, M. Komelj, B. Dkhil, A. Bradeško, D. Damjanović and G. Dražić, "Local structural features and their dynamics in lead-free ferroelectrics at atomic scale," in *CIMTEC 2022,* Perugia, Italy: Center for Imaging Technology Commercialization, 2022.

A. Benčan, O. Condurache, H. Uršič, T. Rojac, D. Damjanović and G. Dražić, "In situ scanning transmission electron microscopy of lead-free ferroelectrics with atomic resolution," in: *16th Multinational Congress on Microscopy*, Brno, Czech Republic: Czechoslovak Microscopy Society, 2022.

Published Scientific Conference Contributions – Abstracts

K. Radan, B. Kmet, S. Drnovšek, T. Rojac, B. Malič, U. Prah, O. Condurache and A. Benčan, "Compositional inhomogeneity in Mn-doped (K,Na,Li)(Nb,Ta)O_3–$CaZrO_3$ lead-free piezoceramics," in *Piezo 2019: Electroceramics for End-Users X*, Špindlerův Mlýn, Czech Republic, 2019.

O. Condurache, K. Radan, B. Kmet, G. Dražić, U. Prah, B. Malič and A. Benčan, "Multiscale investigation of the role of manganese oxide addition in lead-free sodium potasium niobate based piezoelectrics", *3rd Slovene Microscopy Symposium*, Ankaran, Slovenia: Slovene Society for Microscopy, 2019.

O. Condurache, K. Radan, B. Kmet, G. Dražić, B. Malič and A. Benčan, "Compositional study of lead-free sodium potassium niobate based piezoelectric ceramics", in *11th Jožef Stefan International Postgraduate School Students' Conference and 13th Young Researchers' Day*, Planica, Slovenia: Jožef Stefan International Postgraduate School, Jožef Stefan Institute, 2019.

G. Bottaro, V. Buscaglia, G. Canu, M. T. Buscaglia, C. Costa, O. Condurache, L. Curecheriu, L. Mitoseriu and L. Armelao, "The photoluminescence of Eu:$BaZr_xTi_{1-x}O_3$ ceramics", in *XVI. Conference of the European Ceramic Society, ECerS 2019*, Torino, Italy: Akadémiai Kiadó, 2019.

O. Condurache, K. Radan, M. Otoničar, B. Kmet, G. Dražić, U. Prah, G. Kapun, B. Malič and A. Benčan, "Micro-, nano- and atomic structure investigation of alkaline niobate based solid solutions", in *XVI. Conference of the European Ceramic Society, ECerS 2019*, Torino, Italy: Akadémiai Kiadó, 2019.

V. Buscaglia, G. Bottaro, G. Canu, M. T. Buscaglia, C. Costa, O. Condurache, L. Curecheriu, L. Mitoseriu and L. Armelao, "The influence of polar order on the

photoluminescence of Eu:$BaZr_xTi_{1-x}O_3$ ceramics", in *XVI. Conference of the European Ceramic Society, ECerS 2019*, Torino, Italy: Akadémiai Kiadó, 2019.

K. Radan, V. Vignaswaran, U. Prah, O. Condurache, M. Dragomir, T. Gindel, M. Deluca and B. Malič, "Structural phase transitions in multiple-element-modified lead-free piezoelectric ceramics", in *Slovenian Chemistry Days 2020, 26th Annual Meeting of the Slovenian Chemical*, Portorož, Slovenia: Slovenia: Slovenian Chemical Society, 2020.

O. Condurache, G. Dražić, T. Rojac, M. Makarovič, H. Uršič, B. Dkhil and A. Benčan, "Morphology and dynamics of ferroelectric domain walls in bismuth ferrite", in *Slovenian Chemistry Days 2020, 26th Annual Meeting of the Slovenian Chemical*, Portorož, Slovenija: Slovenia: Slovenian Chemical Society, 2020.

A. Mirjanić, U. Prah, M. Sadl, J. Walker, O. Condurache, A. Benčan, T. Rojac, M. Grigoras, H. Uršič, "Local piezoelectric and magnetic properties of $(Bi_{0.88}Gd_{0.12}FeO_3$ ceramics", in *12th Jožef Stefan International Postgraduate School Students' Conference and 14th Young Researchers' Day*, Ljubljana, Slovenia: Jožef Stefan International Postgraduate School, Jožef Stefan Institute, 2020.

K. Radan, V. Vignaswaran, U. Prah, O. Condurache, M. Dragomir, T. Gindel, M. Deluca and B. Malič, "Structure and temperature Induced phase transitions in lead-free Li- and Ta-modified alkaline niobate based piezoceramics probed by Raman spectroscopy", in: *IEEE IFCS 2020 ISAF 2020 Virtual Conference,* Keystone, Colorado, USA: joint Conference of IEEE International Symposium on Applications of Ferroelectrics, 2020.

K. Radan, V. Vignaswaran, U. Prah, O. Condurache, M. Dragomir, T. Gindel, M. Deluca and B. Malič, "Influence of MnO_2 addition on structural phase transitions and electrical properties of lead-free Li- and Ta-modified alkaline niobate based piezoceramics", in: *Electroceramics XVII, International Virtual Conference*, Darmstadt, Germany: Technical University of Darmstadt, 2020.

O. Condurache, K. Radan, U. Prah, M. Otoničar, B. Kmet, G. Dražić, B. Malič and A. Benčan, "Electron Microscopy study of lead-free piezoelectrics at different length scales", in: *Electroceramics XVII, International Virtual Conference*, Darmstadt, Germany: Technical University of Darmstadt, 2020.

O. Condurache, G. Dražić, N. Sakamoto, T. Rojac, B. Dkhil, A. Bradeško, H. Uršič and A. Benčan, "Static and dynamic study of domain walls in lead-free ferroelectrics", in: *Slovenian Chemistry Days 2021 , 27th Annual Meeting of the Slovenian Chemical Society*, Portorož, Slovenia: Slovenian Chemical Society, 2021.

K. Žiberna, S. W. Konsago, B. Malič, B. Kmet, O. Condurache and A. Benčan, "Electron microscopy study of $BaTiO_3$-based thin films prepared by chemical solution deposition", in: *Slovenian Chemistry Days 2021 , 27th Annual Meeting of the Slovenian Chemical Society*, Portorož, Slovenia: Slovenian Chemical Society, 2021.

M. Sadl, O. Condurache, A. Benčan, M. Dragomir, U. Prah, B. Malič and H. Uršič, "Relaxor-ferroelectric ceramic thick films integrated by aerosol deposition on metal and polymer substrates", in *13th Jožef Stefan International Postgraduate School Students' Conference and 15th Young Researchers' Day*, Ljubljana, Slovenia: Jožef Stefan International Postgraduate School, Jožef Stefan Institute, 2021

K. Žiberna, S. W. Konsago, O. Condurache, B. Kmet, B. Malič and A. Benčan, "Microstructural characterization of ferroelectric $BaTiO_3$-based thin films", in: *13th Jožef Stefan International Postgraduate School Students' Conference and 15th Young Researchers' Day*, Ljubljana, Slovenia: Jožef Stefan International Postgraduate School, Jožef Stefan Institute, 2021.

O. Condurache, G. Dražić, N. Sakamoto, T. Rojac, B. Dkhil, H. Uršič and A. Benčan, "Investigation of domain walls in ferroelectric bismuth ferrite at the atomic scale", in: *13th Jožef Stefan International Postgraduate School Students' Conference and 15th Young Researchers' Day*, Ljubljana, Slovenia: Jožef Stefan International Postgraduate School, Jožef Stefan Institute, 2021.

O. Condurache, G. Dražić, N. Sakamoto, T. Rojac, B. Dkhil, H. Uršič and A. Benčan, "Morphology, structure and dynamics of domain walls in $BiFeO_3$ bulk systems", in: *IEEE ISAF 2021 joint ISAF ISIF-PMF virtual Conference, IEEE International Symposium on Applications of Ferroelectric (ISAF), International Symposium on Integrated Functionalities (ISIF), Piezoresponse Force Microscopy Workshop (PFM)*, Sydney, Australia: Institute of Electrical and Electronics Engineers (IEEE), 2021.

M. Sadl, O. Condurache, A. Benčan, M. Dragomir, U. Prah, B. Malič, M. Deluca, et al., "Integration of aerosol deposited $0.9Pb(Mg_{1/3}Nb_{2/3})O_3{-}0.1PbTiO_3$ thick films on low-cost stainless steel and flexible polymer substrates", in: *IEEE ISAF 2021 joint ISAF ISIF-PMF virtual Conference, IEEE International Symposium on Applications of Ferroelectric (ISAF), International Symposium on Integrated Functionalities (ISIF), Piezoresponse Force Microscopy Workshop (PFM)*, Sydney, Australia: Institute of Electrical and Electronics Engineers (IEEE), 2021.

M. Sadl, O. Condurache, M. Dragomir, A. Benčan, U. Prah, B. Malič, H. Uršič, et al., "$0.9Pb(Mg_{1/3}Nb_{2/3})O_3{-}0.1PbTiO_3$ thick films integrated by aerosol deposition on metal and polymer substrates", in *Electronic materials and applications (EMA) 2021*, virtual only event: The American Ceramic Society, 2021.

H. Uršič, M. Sadl, O. Condurache, A. Benčan, M. Dragomir, B. Malič, "Relaxor-ferroelectric $0.9Pb(Mg_{1/3}Nb_{2/3})O_3{-}0.1PbTiO_3$ ceramic thick films integrated by aerosol deposition on stainless-steel and polymer substrates", in *8th International Workshop on piezoelectric MEMS: online/on-site hybrid meeting*, Nara, Japan: 2021.

M. Sadl, O. Condurache, A. Benčan, M. Dragomir, U. Prah, B. Malič and H. Uršič, "Energy storage and electrocaloric $(1{-}x)Pb(Mg_{1/3}Nb_{2/3})O_3{-}xPbTiO_3$ thick films realized by aerosol deposition method", in *56th International Conference on Microelectronics, Devices and Materials & the Workshop on Personal Sensor for Remote Health Care Monitoring*, Ljubljana, Slovenia: MIDEM - Society for Microelectronics, Electronic Components and Materials, 2021

O. Condurache, G. Dražić, N. Sakamoto, T. Rojac, B. Dkhil, H. Uršič and A. Benčan, "Atomically resolved properties of domain walls in ferroelectric $BiFeO_3$ bulk", in: *[1st] Crossnano Crossborder Workshop in Nanoscience and Nanotechnology*, Trieste, Italy: University of Trieste, 2021.

M. Sadl, O. Condurache, A. Benčan, M. Dragomir, U. Prah, B. Malič, H. Uršič, "Aerosol deposition as an enabling technology for flexible energy storage and electrocaloric devices", in: *[1st] Crossnano Crossborder Workshop in Nanoscience and Nanotechnology*, Trieste, Italy: University of Trieste, 2021.

O. Condurache, G. Dražić, T. Rojac, B. Dkhil, A. Bradeško, H. Uršič and A. Benčan, "Monitoring bismuth ferrite domain walls behavior under electric field with atomic resolution by in situ scanning transmission electron microscopy," in: *Microscopy and Microanalysis 2022,* Oregon, Portland: Microscopy Society of America, 2022.

M. Sadl, O. Condurache, A. Benčan, M. Dragomir, B. Malič, A. Lebar, J. Valentinčič, H. Uršič, et al., "Energy storage $Pb(Mg_{1/3}Nb_{2/3})O_3{-}PbTiO_3$ thick films integrated by aerosol deposition on metal and polymer substrates", in: *ISAF 2022: ISAF-PFM-*

ECAPD joint conference, Tours, France: Institute of Electrical and Electronics Engineers (IEEE), 2022.

O. Condurache, G. Dražić, T. Rojac, H. Uršič, B. Dkhil, A. Bradeško and A. Benčan, "Dynamics of ferroelectric domain walls in bismuth ferrite observed by in-situ voltage biasing transmission electron microscopy," in: *CIMTEC 2022,* Perugia, Italy: Center for Imaging Technology Commercialization, 2022.

O. Condurache, G. Dražić, T. Rojac, H. Uršič, B. Dkhil, A. Bradeško and A. Benčan, "In-situ scanning transmission electron microscopy study of ferroelectric domain walls," in: *Ceramics in Europe 2022*, Kraków, Poland*,* 2022]

R.-S. Stirbu, L. P. Curecheriu, L. Padurariu, V. A. Lukacs, G. Caruntu, M. T. Buscaglia, O. Condurache and L. Mitoseriu, "Comparative analysis of $BaTiO_3$ ceramics produced from cuboidal and spherical nanoparticles," in: *Ceramics in Europe 2022,* Kraków, Poland*,* 2022.

M. Koblar, O. Condurache, K. Žiberna, K. Pušnik Črešnar, L. Fras Zemljič, M. Kušter, A. Benčan, M. Otoničar, "Correct determination of chemical composition using Monte Carlo simulation and Energy Dispersive X-ray Spectroscopy (EDXS)," in: *4th Slovenian microscopists' conference,* Ankaran, Slovenia: Slovenian Society for Microscopy, 2022.

A. Benčan, O. Condurache, H. Uršič, T. Rojac, D. Damjanović and G. Dražić, "Lead-free ferroelectrics at atomic scale," in *4th Slovenian microscopists' Conference,* Ankaran, Slovenia: Slovenian Society for Microscopy, 2022.

Biography

The author of this thesis was born in Botoșani, Romania. She received her BSc degree in 2016 at the Faculty of Physics, A.I. Cuza University of Iași, Romania. In 2018, she completed an MSc in Physics for Advanced Technologies at the same university. During her undergraduate studies, she performed three Erasmus summer internships at the Institute of Condensed Matter and Technologies for Energy, Genova, Italy. During her master's degree, she interned at the Italian Institute of Technology, Smart Materials Department, Genova, Italy.

In 2018 she enrolled in the Sensor Technologies PhD program at Jožef Stefan International Postgraduate School, Ljubljana, Slovenia, under the supervision of Prof. Dr. Andreja Benčan Golob and Prof. Dr. Goran Dražić. Her research focused on the study of ferroelectric materials using transmission electron microscopy (TEM). During her PhD she was particularly interested in the investigation of ferroelectric domain walls at the atomic scale by atomic resolution TEM and in situ electric biasing TEM.